

**Thermosyphon-Cooled Axial Gap Electric Motors
for Ship Propulsion Applications**

by
Timothy John McCoy

Naval Engineer, S.M. Electrical Engineering and Computer Science,
Massachusetts Institute of Technology, (1993)

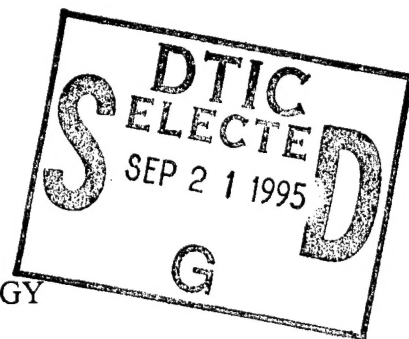
B.S. Mech. Eng., University of Illinois, (1983)

Submitted to the department of OCEAN ENGINEERING in partial fulfillment of the
requirements for the degree of

DOCTOR OF PHILOSOPHY
in the field of

NAVAL ENGINEERING

at the
MASSACHUSETTS INSTITUTE OF TECHNOLOGY
June 1995



© Timothy J. McCoy, all rights reserved.

The Author hereby grants to M.I.T. and the U.S. Government permission to reproduce and to distribute this document in whole or part.

Signature of Author: T. J. McCoy
Department of Ocean Engineering, May 1995

Certified by: James L. Kirtley, Jr.
James L. Kirtley, Jr.
Professor of Electrical Engineering
Thesis Supervisor

Certified by: Joseph L. Smith
Joseph L. Smith
Collins Professor of Engineering
Thesis Committee Member

Certified by: A. Douglas Carmichael
A. Douglas Carmichael
Professor of Power Engineering
Thesis Committee Member

Accepted by: A. Douglas Carmichael
A. Douglas Carmichael
Departmental Graduate Committee
Department of Ocean Engineering

DISTRIBUTION STATEMENT A
Approved for public release;
Distribution Unlimited

19950913 032

DTIC QUALITY INSPECTED 3

Thermosyphon-Cooled Axial Gap Electric Motors for Ship Propulsion Applications

by

Timothy John McCoy

Submitted to the Department of Ocean Engineering on May 2, 1995 in partial fulfillment of the requirements for the degree of Doctor of Philosophy in the field of Naval Engineering.

Abstract

There are many attributes of electric propulsion which make it a desirable technology for use in modern warship designs. However, current motor technology makes electric propulsion noncompetitive from a cost standpoint. The single largest impediment to making electric propulsion more affordable is the size of the propulsion motors. Two technologies aimed at reducing the size of ship propulsion motors are investigated, rotor cooling via radial rotating thermosyphons and the multi-disk axial gap geometry.

Size reductions in electric motors are ultimately limited by the ability to remove heat from the windings. Two-phase thermosyphons are considered for cooling the rotor windings of an axial gap motor because they can transfer large amounts of heat with a relatively small temperature difference. Predictions for the heat transfer coefficients of two-phase radially mounted thermosyphons are developed and experimentally evaluated.

The multi-disk axial gap geometry significantly reduces both the weight and volume of an electric propulsion motor over conventional radial gap designs. This is accomplished by consolidating several machines together on a single shaft that share a common magnetic circuit. This novel geometry also allows significant reduction in the motor's diameter, giving the ship designer more flexibility in locating the propulsion motors within the ship. A computerized propulsion motor design tool is developed for conducting preliminary design studies of this type of motor. This tool can be used in conjunction with a ship synthesis model to conduct feasibility level ship studies in order to evaluate the total ship impact of this innovative motor technology.

The two technologies described above have a synergistic effect when combined into a single design. A destroyer-sized motor of 35,000 HP @ 164 RPM exhibits a 15% weight reduction and more than a 30% volume reduction over the latest designs currently being developed by the U.S. Navy.

Thesis Supervisor: Dr. James L. Kirtley, Jr.

Title: Professor of Electrical Engineering

Acknowledgments

I would like to thank The United States Navy for providing me the opportunity to pursue my graduate studies and for funding my five years here at M.I.T. I would also like to thank the Office of Naval Research for their financial support of this research project. This thesis would not have been possible without their support.

I am very grateful to Professor Jim Kirtley, my advisor and Professors Doug Carmichael and Joe Smith, my thesis committee, for their support, challenges, suggestions and encouragement throughout the course of this work. Thank you all.

I would also like to thank the numerous people who made this work possible. It is unfortunate that only one person's name can go on the front of a thesis since any project such as this is very much a group effort. Thanks to all of my many friends and colleagues at the LEES lab for their camaraderie and intellectual stimulation. I owe the successful completion of experimental portion of this research to the technical expertise of Wayne Hagman and Professor Steve Leeb of LEES; and Mike Demaree and Bob Gertsen of the Cryogenics Lab, who always took time from their busy schedules to help me with my numerous experimental difficulties. The UROP students, Jason, Noel and Eileen who helped take data all did an outstanding job. Your efforts are much appreciated. Thanks also to Vivian Mizuno and Jennifer Laible for their outstanding administrative support of this work.

Finally, I would like to thank my family for being there when I needed them. To my wife Sandra, who has shown infinite love, patience and understanding over the past five years, I owe a debt which I will never be able to repay.

Accession For	
NTIS CRA&I	<input checked="" type="checkbox"/>
DTIC TAB	<input type="checkbox"/>
Unannounced	<input type="checkbox"/>
Justification <i>Per form 50</i>	
By _____	
Distribution /	
Availability Codes	
Dist	Avail and/or Special
<i>A-1</i>	

In memory of my mother:

Ida J. McCoy

1920 - 1990

Table of Contents

Abstract	2
Acknowledgments	3
Table of Contents	5
List of Symbols	7
Chapter 1: Introduction	13
1.1 Background and Motivation	13
1.1.1 Electric Drive Ships	13
1.1.2 Propulsion Motors	17
1.1.3 Thermosyphons and Heat Pipes	21
1.2 Previous Research	23
1.3 Aim of Present Research	26
Chapter 2: Axial Propulsion Motors	30
2.1 Voltage and Current	31
2.2 Reactance and Resistance	33
2.3 Structural Design	38
2.4 Weight and Volume	42
2.5 Losses and Efficiency	44
2.6 Heat Transfer	45
2.6.1 Air Gap Heat Transfer	46
2.6.2 Direct Water Cooling	48
2.6.3 Indirect Water Cooling	49
2.6.4 Hydrogen Cooling	49
2.6.5 Air Cooling	49
2.6.6 Two-Phase Cooling Methods	50
Chapter 3: Radial Rotating Thermosyphons	52
3.1 Film Condensation	52
3.2 Film Evaporation	60
3.3 Nusselt Analysis Restrictions	62
3.4 Pool Boiling	65
3.5 Coriolis Effects	67
3.6 Performance Limits	69

3.6.1 Viscous Limit	69
3.6.2 Sonic Limit	70
3.6.3 Entrainment Limit	70
3.6.4 Burnout Limit	71
3.6.5 Dry-Out Limit	73
3.6.6 Flooding Limit	74
3.7 External Heat Transfer	74
Chapter 4: Experimental Setup	83
4.1 Experiment Design	83
4.2 Measurements and Calculations	84
4.3 The Test Apparatus	87
4.4 Accuracy and Error Analysis	92
Chapter 5: Results and Conclusions	97
5.1 Experimental Results	97
5.2 Preliminary Design Tool	100
5.2.1 Design Example	104
5.3 Conclusions and Recommendations for Future Research	105
Appendix A: Thermosyphon Construction	118
Appendix B: Data Summary	124

List of Symbols

Symbol	Description	Units
A	Area	meters ²
α	Angle	radians
α_1	Thermal diffusivity	m ² /sec.
Ar	Archemedes number	
B	Air gap flux density	Tesla
β	Fin parameter	1 / m
C_p	Constant pressure specific heat	J/kg-°C
C_w	Flow Coefficient	
C_{nb}	Nucleate boiling coefficient	
D_h	Hydraulic diameter	meters
d	Diameter	meters
δ	Film thickness	meters
e_{af}	Voltage behind synchronous reactance	per unit
Ek	Ekman number	
Φ	Flux per pole	Webers
F	Magneto-motive force	
G	Gap ratio	
Γ	Mass flux	kg/m-sec.
g	Air gap length	meters
H	Magnetic Field	Amp-turns
η	Efficiency	
η_f	Fin Efficiency	

Symbol	Description	Units
h_{fg}	Heat of vaporation	J/kg
h	Enthalpy	J/kg
h	Heat transfer coefficient	W / m ² -°C
h	Slot height	meters
I	Current	Amps
I_p	Polar moment of inertia	meters ⁴
J	Current density	A/m ²
Ja	Jakob number	
K	Surface current density	A/m
k_b	Breadth factor	
k_p	Pitch factor	
k	Thermal conductivity	W / m -°C
L_t	Turn Length	meters
λ	Flux linkage	Weber-Turns
λ_r	Rotor space factor	
λ_s	Stator space factor	
μ	Fluid viscosity	kg / m-sec.
\dot{m}''	Condensation / evaporation rate	kg / m ² -sec.
\dot{m}	Mass flow rate	kg / sec.
m	Number of phases	
μ_0	Permittivity of free space	Henry / meter
N_f	Number of field winding turns	
N_s	Number of stator winding turns	
N_g	Number of air-gaps	

Symbol	Description	Units
N_r	Number of rotors	
N_s	Number of stators	
ν	Kinematic viscosity	$\text{m}^2/\text{sec.}$
Nu	Nusselt number	
P	Pitch	
P	Power	Watts
p	Number of pole pairs	
Pr	Prantl number	
Θ	Dimensionless temperature difference	
Q	Heat flow rate	Watts
\dot{Q}	Volume flow rate	$\text{m}^3/\text{sec.}$
θ	Angle	radians
R	Resistance	Ohms
ρ	Density	kg / m^3
r	Radius	meters
Re	Reynolds number	
RSF	Rotor slot factor	
S_r	Number of rotors	
S_s	Number of stators	
S	Tube spacing	meters
σ	Surface tension	N / m
SSF	Stator slot factor	
T	Temperature	deg. C
T	Torque	Newton-meters

Symbol	Description	Units
t_b	back iron thickness	meters
t_r	rotor disk thickness	meters
τ	Shear Stress	Pascals
t_s	stator disk thickness	meters
t	Time	seconds
τ_{\max}	Maximum allowable shear stress	Pa
u	X-direction velocity	m / sec.
V	Velocity	m / sec.
V	Voltage	volts
v	Volume	meters ³
v	Y-direction velocity	m / sec.
ω	Electrical frequency, speed of rotation	rad. / sec.
Ω	Speed of rotation	rad. / sec.
w	Slot width	meters
X	Offset distance from axis of rotation	meters
X_{al}	Leakage reactance	Ohms
X_{aa0}	Phase reactance	Ohms
X_d	Synchronous reactance	Ohms
x	Per unit reactance	per unit
ψ	Power factor angle	radians
Z	Impedance	Ohms

Subscripts

Subscript	Description
a	Armature
a	Axial
ag	Air-gap
b	Back iron
c	Condenser
cu	Copper
cw	Condenser wall
D	per disk
e	Evaporator
eff	Effective
ew	Evaporator wall
f	Field
fnl	Field no-load
g	Air-gap
i	Inner
in	Input
l	liquid
Lc	Condenser exit
Le	End of evaporator
max	Maximum
o	Outer

Subscript	Description
out	Outlet
p	Parallel
p	Pool
θ	θ -directed
r	radial
r	Rotor
rms	Root Mean Square
s	Series
s	Stator
sat	Saturation
scu	Stator copper
si	Stator iron
t	Tangential
v	vapor
w	Wall
w	Winding loss
z	Z-direction

Chapter 1: Introduction

1.1 Background and Motivation

Due to the current political and budgetary climate, the United States Navy is under great pressure to reduce both the acquisition and operational cost of its ships. One technology which shows great promise for reducing the size and manpower requirements of ships, and consequently their cost, is integrated electric propulsion. Some of the advantages of this type of propulsion system include increased arrangement flexibility, increased fuel efficiency, increased automation and reduced manning, all of which contribute to reducing the cost of a ship without sacrificing its mission capability.

The U.S. Navy has been conducting research in various technologies that will help make modern electric drive ships feasible in the near future. As part of that research, this thesis looks at novel cooling techniques as applied to axial gap motors that are very well suited to ship propulsion applications.

1.1.1 Electric Drive Ships

Electrically driven ships are not new. They have existed in one form or another for most of this century. However, since the 1940's electric drive has not been competitive with mechanical drive systems for warship applications. The variable speed requirement for ship propulsion systems has historically limited electric drive systems to the power levels achievable with brush-commutated direct current drive motors. Today this limit is only about 10,000 horsepower. A typical 8000 ton destroyer requires 30,000 - 40,000 horsepower per propeller shaft. Modern computerized control systems and high power

semiconductor switching devices have made variable speed electric drive systems possible using wound-field or permanent magnet synchronous motor technology.

The decision process of what goes where on a modern warship is largely a trade-off between many conflicting design requirements. Propulsion and electrical systems, while essential for every ship, are not part of the mission payload and thus their location within the ship should be subordinate to the placement of the payload items. In the case of a warship, those payload items are the combat systems.

Mechanical drive systems must maintain a stringent alignment between the propulsion prime movers and the ship's propellers. This constraint severely constricts ship arrangement options. Additionally, it makes construction more difficult and expensive due to the long propulsion shafts which must be aligned during construction.

Steam driven ships require boilers, condensers, steam turbines and other very large and heavy propulsion equipment. To ensure the stability of the ship, these heavy items are placed low in the ship's hull. This arrangement works well since this location is required anyway to maintain the mechanical drive system's alignment. In the past thirty years, the U.S. Navy and most other navies have switched to gas turbine mechanical drive on combatant ships. Gas turbine engines are very small and light when compared to a steam propulsion system of similar power rating, but they have other drawbacks. Gas turbines require large amounts of air, are non-reversible and suffer from poor fuel efficiency when operated at off-design conditions.

In modern mechanical drive ships, the gas turbines are located low in the hull to maintain alignment with the propeller shafts (see Figure 1-1a). This arrangement results in

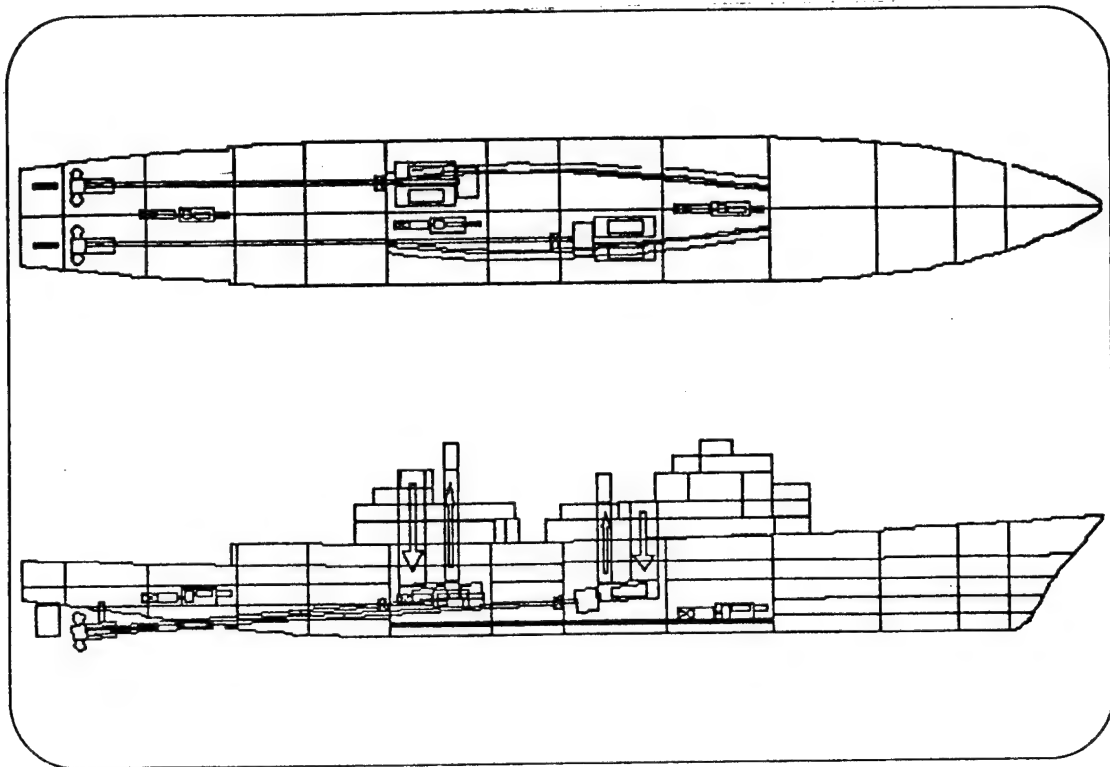


Figure 1-1a: Conventional ship arrangement.

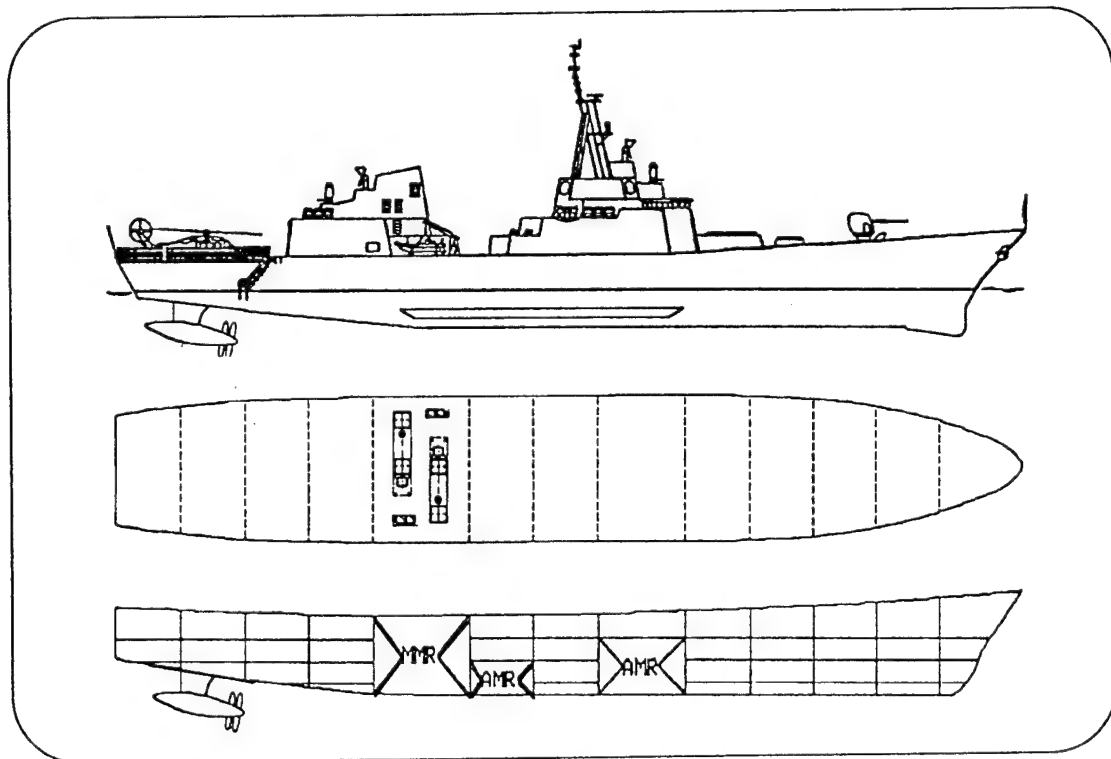


Figure 1-1b: Podded-Propulsor ship arrangement.

long intake and exhaust ducts which take up much valuable space aboard the ship. The non-reversibility of the engines is usually compensated for via reversible pitch propellers. While reversible pitch propellers have worked very well in the fleet, they are costly and are inherently less efficient than a properly designed fixed-pitch propeller.

All of these drawbacks could be eliminated with an electric drive system. By eliminating the mechanical connection between the gas turbines and the propellers, the engines could be placed higher in the ship where they would require less volume for intake and exhaust ducting. This results in a smaller ship design. The variable speed and reversing requirement can be handled via the control of the semiconductor switching devices which feed power to the propulsion motors. This eliminates the need for reversible pitch propellers. Combining the propulsion and ship's service electric power loads on a common prime mover reduces the total number of installed gas turbines on the ship. If they are sized properly for the ship's operating profile a significant fuel savings can be expected. Electric drive also provides the ability to "cross-connect" the propulsion motors; that is, to split the output from one operating gas turbine generator between both propulsion motors in a twin screw ship. This flexibility existed with steam propulsion and was lost upon switching to mechanical gas turbine drive.

With present day technology, electric propulsion is still not cost competitive with modern mechanical drive systems. This is primarily due to the large size and weight of a direct-drive electric motor. In order to achieve all of the benefits cited above, the propulsion motors would also have to be moved outside the ship's hull as depicted in figure 1-1b. This concept is known as "podded-propulsors" and further restricts the size

of the propulsion motor beyond that required for an "inside-the-hull" electric drive arrangement.

1.1.2 Propulsion Motors

Electric motors for ship propulsion are subject to a rather unusual set of constraints. They can be best characterized as low-speed high-torque machines. Recall that power (P) and torque (T) are related by:

$$P = T \cdot \Omega \quad (1.1)$$

where Ω is the rotational speed in radians / second. A typical propulsion motor for an 8000 ton destroyer might be rated at 30 MW @ 164 rpm, a torque of 1.75×10^6 N-m.

Torque in a conventional radial gap electric machine is given by:

$$T = 2\pi R^2 L \cdot \tau \quad (1.2)$$

where τ is the electromagnetic shear stress, R and L are the rotor radius and length, respectively. In an axial gap machine, the torque is given by:

$$T = \frac{2}{3}\pi(R_o^3 - R_i^3) \cdot \tau \quad (1.3)$$

where R_o and R_i are the outer and inner radii of the rotor. Equations (1.2) and (1.3) assume one air-gap in the motor. In either geometry, the radius should be as large as possible to maximize the generated torque. Normally, the limit to the radius is determined from structural considerations. However, the ship's geometry constrains the radius to less than structural limits would normally allow. For inside-the-hull use, the outer radius of the motor would be limited to about 2 meters. For a podded-propulsor ship, the outer radius

could be no more than 1 meter with a length limit of about 2.0 meters. Current motor technology can meet the in-hull limit; however, the size and weight make the system noncompetitive with a mechanical drive system from a cost standpoint. The size limitations of the podded-propulsor configurations are beyond current motor technology.

There has been a great deal of effort aimed at reducing the size of propulsion motors. Numerous technologies have been suggested for use including superconducting homopolar DC and water-cooled permanent magnet AC machines [1-1],[1-2]and [1-3]. Common to all of the proposed technologies is the need to use sophisticated cooling techniques.

As can be seen from (1.2) and (1.3), to reduce the size of any electric machine without reducing the torque output, the electromagnetic shear stress must be increased. The electromagnetic shear stress (τ) is given by:

$$\tau = B_g \cdot K_s \quad (1.4)$$

where B_g is the air-gap magnetic flux density, and K_s is the stator surface current density. The magnetic flux density is limited by saturation effects in the iron of the machine, so the only way to further increase the electromagnetic shear stress is to increase the current density. Increasing the current density also increases the resistive heating losses in the windings. Therefore, the current density is limited by the ability to remove the generated heat from the windings. For a ship propulsion motor to be successful, it must have high current densities and consequently requires some sort of advanced cooling methods.

The cooling methods which are typically used in large machines are not suitable for shipboard use. The most common methods used today in large turbine generators are

hydrogen cooling and direct water cooling. Due to the explosive nature of hydrogen gas, it is unacceptable for shipboard use. Helium could be considered as a substitute; however, its density/specific heat product is only 2/3 that of hydrogen gas. This means 50% more volumetric flow rate is required to remove the same amount of heat with the same temperature difference.

Water cooling could be used and has been considered in previous propulsion motor designs. In direct water cooling the conductors of the winding are hollow and cooling water passes through these hollow conductors in direct contact with the copper conductors. The same cooling water must also come into contact with pumps and heat exchangers which are at ground potential. The main drawback to direct water cooling is the high water purity requirements which must be maintained for the water to span the required voltage potential without shorting out the windings. While technically feasible, direct water cooling poses the potential to become a major maintenance problem at a time when the Navy is looking to significantly reduce its maintenance expenses.

Another cooling method exists which has become the central focus of this research. Two-phase rotating thermosyphons are able to move heat away from the rotor winding to the central part of the rotor nearly isothermally. Heat fluxes on the order of 10^6 Watts/meter² are possible with these devices. The heat generated in the windings may then be removed from the motor by passing cooling air or water through the center of the motor. Two-phase capillary heat pipes could be used in a similar fashion to remove heat from the stator windings to the periphery of the machine. Although this complicates the design and construction of the motor, the thermosyphons and heat pipes are virtually

maintenance free once installed. As a result, this type of motor would be much simpler to operate and maintain than one which requires direct water cooling.

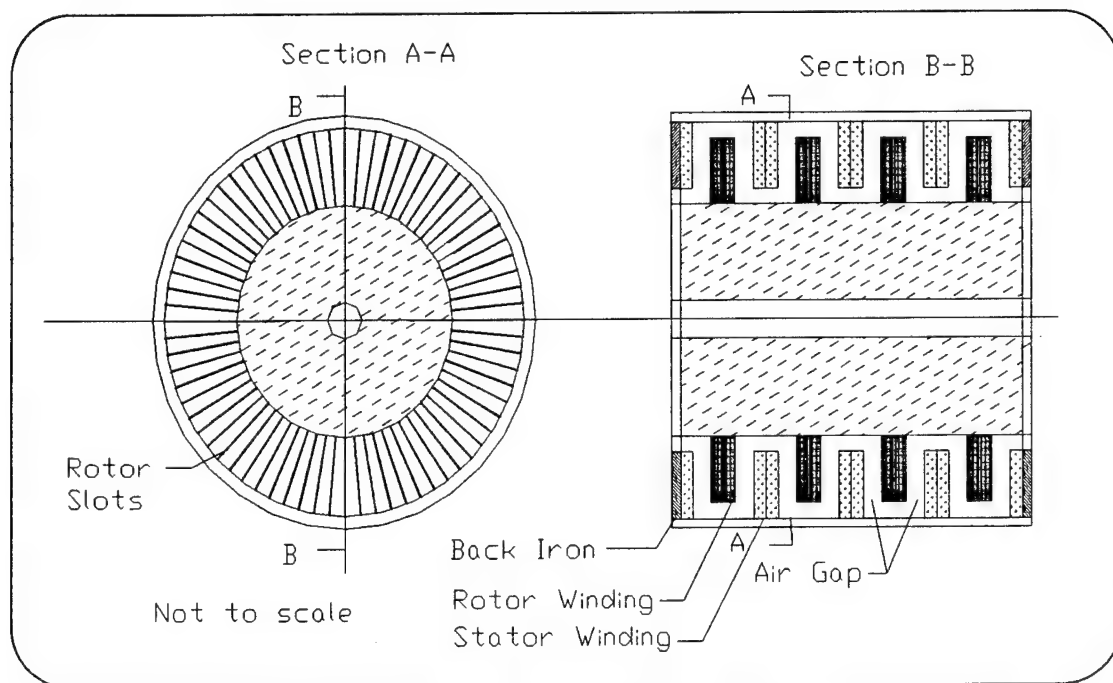


Figure 1-2: Multi-disk axial motor geometry.

Another technology which shows promise for ship propulsion applications is the multi-disk axial gap motor. Figure 1-2 shows a schematic representation of this geometry. With the radius constrained the only way to increase the size of a conventional machine is to lengthen it. With the outer radius similarly constrained, the size of an axial machine may be increased by reducing the inner radius or by combining multiple machines on the same shaft. It turns out that the optimum ratio of r_i / r_o for maximum torque generation is in the range of 0.5-0.6 depending upon the number of pole pairs [1-4]. The multi-disk geometry is simply the consolidation of several axial gap machines together on the same shaft that share a common magnetic circuit. Although this does increase the length of the

machine, this increased length is much less than that required for a conventional radial gap machine to achieve a similar power rating.

The combination of the multi-disk axial gap geometry with the highly efficient cooling capability of radial rotating thermosyphons and heat pipes will allow significant size reductions in the ship propulsion motor. These size reductions are necessary to make electric drive cost competitive with mechanical systems.

1.1.3 Thermosyphons and Heat Pipes

Thermosyphons and heat pipes have been in existence for many years. Both are highly efficient heat transfer devices which operate by recirculating a fluid within a closed hollow tube. Figure 1-3 shows a schematic representation of the thermosyphon. Heat is transferred via latent heat during the evaporation and condensation of the working fluid. While a thermosyphon relies on gravity to return the liquid portion of the working fluid to the evaporator, a heat pipe contains a wick structure that uses capillary action to return the fluid to the evaporator. This allows a heat pipe to work in zero gravity or inverted (with the condenser section below the evaporator section). Both thermosyphons and heat pipes can achieve an effective thermal conductivity which is several hundred times greater than that of copper [1-5].

For analysis purposes, the thermosyphon can be separated into its constituent components: condenser, evaporator and adiabatic sections. Vapor enters the condenser section where it is condensed on the walls via the film condensation process. The liquid film flows through the adiabatic section into the evaporator on the walls of the heat pipe.

When the liquid reaches the evaporator section, the wall temperature rises above the saturation temperature and the film begins to evaporate. At some point in the evaporator, the film will reach the pool of liquid in the bottom of the evaporator, replenishing it. The liquid pool undergoes a pool boiling process, creating vapor to repeat the cycle. Although treated as separate phenomena in most heat transfer texts, in the thermosyphon each process is related to the others through the conservation laws.

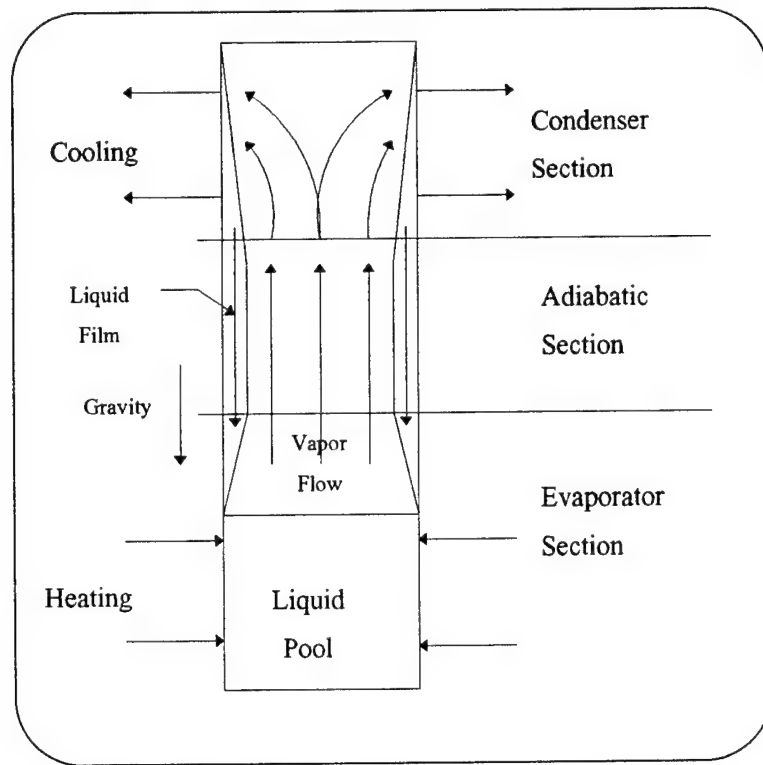


Figure 1-3: Typical thermosyphon.

The radial rotating thermosyphon (RRT) is related to the "rotating heat pipe" which was first introduced by Gray [1-6] in 1969. Both devices rely on the centrifugal force of rotation to return the condensate to the evaporator. In the rotating heat pipe the axis of rotation is parallel to or coincident with the pipe axis. In the radial rotating

thermosyphon the axis of rotation is perpendicular to the axis of the pipe. This simple geometry change significantly alters the analysis of fluid flow and heat transfer in the device.

Capillary and rotating heat pipes have been developed for many applications and their heat transfer characteristics are fairly well understood [1-5]. Radial rotating thermosyphons have been largely ignored to date. One of the contributions of this thesis is to provide some insight into the heat transfer characteristics of these devices.

1.2 Previous Research

There are several fields of research which apply to the present study. These include ship propulsion, axial gap motors, cooling of electric motors, heat pipes & thermosyphons, two-phase flow, heat transfer and gas turbine technology just to name a few. The following section summarizes some of the more important and interesting works in the various fields of applicability to this thesis.

There have been numerous papers published concerning the design of axial gap motors. The vast majority of these deal with small permanent-magnet A.C. and D.C. machines. Takeda [1-7] discusses a variable-reluctance machine and Varga [1-8] has published several nearly identical papers about induction machines. All reviewed publications on axial gap machines concentrate on the basic electromagnetic circuit and design performance of the motors. Little attention is paid to the structural or thermal design of the motors in these papers. None of the papers concerned with axial gap motors consider anything other than air-gap cooling. Di-Napoli [1-4] develops relationships for torque, iron & copper weight, iron & copper losses, power and efficiency vs. radius ratio.

Chan [1-9] and Desequilles [1-10] both discuss the possibility of using a multi-disk geometry with permanent magnet machines. Chan also calculates the optimum radius ratio for maximum power and minimum rotor inertia. Several of these authors hint at or state that axial gap machines are more power dense than conventional machines, but none prove this assertion. The paper by Leung & Chan [1-11] is the only paper reviewed that considers space harmonics of the magnetic field in the air-gap. This paper discusses pole shaping on salient pole synchronous axial machines.

There have been numerous publications concerning thermal modeling of conventional radial gap motors: [1-12], [1-13] and [1-14] for example. However, there seem to be no published studies of the thermal behavior of axial gap motors. The underlying principles are the same, but the geometry is significantly different which makes any models developed for radial gap machines invalid.

A rotating disk that is convectively cooled on its sides is the basic geometry to be considered for modeling the air-gap heat transfer in the axial gap machine. There has been an abundance of experimental and theoretical work done on this problem, both with and without a nearby stator. Most of the research was concerned with the cooling of gas turbine rotors. The authority on this particular heat transfer problem appears to be J.M. Owen who has published several papers on the subject. The most useful of his works is [1-15] which provides a complete set of design formulae for determining heat transfer coefficients for both the stator and rotor as a function of rotational speed, air-gap length and air mass flow rate.

There have been a few papers published regarding electric machines with heat-pipe or thermosyphon cooling: [1-16], [1-17], [1-18], [1-19], and [1-20]. All of these are exclusively concerned with radial gap machines. Consequently the heat pipes considered are axially oriented on the rotor of the machine and are only of limited use in the present study.

The field of literature which has been useful in the present study of radially oriented thermosyphons is gas turbine blade cooling. In the late 1940's and 1950's there was quite a bit of research done on liquid and two-phase cooling of gas turbine blades. Developments in this area apparently died out as high temperature alloys were developed for turbine blades. There was a resurgence of interest in this area in the late 1970's largely due to the energy crisis. Of the early work, the most interesting paper is by Cohen & Bayley [1-21] that considers using radially mounted two-phase thermosyphons to cool gas turbine blades. They built a rotating test rig to show that they could transfer heat from the tip to the center of the rotor, but all of their quantitative experiments were carried out on a fixed gravitational thermosyphon. The later work was concentrated on the more fundamental problems of flow and heat transfer in rotating fluid films. Of particular interest here are the theses by Mudawar [1-22] and El-Masri [1-23]. Both of these works look at heat transfer from thin rotating films.

There is an extensive body of literature on thermosyphons and heat pipes. Although there are numerous references in this area, most of the pertinent research can be summarized with just a few papers. The paper by Al-Farah [1-24] is the most complicated numerical analysis of a tilted thermosyphon. It models the thermosyphon using a

three-dimensional finite difference solution. Harley [1-25] provides a fairly useful transient two-dimensional numerical model for thermosyphons. Reed & Tien [1-26] develop a very useful one-dimensional analytical model for the thermosyphon which includes a prediction of the flooding failure mode. Shiraishi [1-27] does one of the better experimental analyses and develops empirical equations for the heat transfer coefficients based upon Nusselt theory. The paper by Nguyen-Chi [1-28] contains a good description of the various operating limits for thermosyphons. This paper also develops the flooding limit theoretically and corroborates it experimentally.

Most of the other papers are quite repetitive, with a modified Nusselt analysis compared to their experimental results. All of the previously published work in the thermosyphon field has been done in a gravitational system. Apparently, there has been no published research concerning thermosyphons in a centrifugal gravity field.

Another related field which has seen much press is that of the "rotating heat pipe" which is actually an axially mounted rotating thermosyphon. P.J. Marto has published numerous papers on this subject, [1-29] provides a very good overview of the research through 1984. Because of the geometry difference between the axial and radial rotating thermosyphons, the research in the rotating heat pipe field cannot be applied to the radial rotating thermosyphon.

1.3 Aim of Present Research

The research underlying this thesis hopes to accomplish three main objectives. The first objective of this thesis is to develop a computerized design tool for conducting a preliminary design of multi-disk axial gap motors. This design tool will include

electromagnetic, thermal and structural aspects of the motor design. In order to properly develop the thermal design of the motor, it is necessary to consider both the air-gap cooling and cooling of the windings via advanced cooling methods such as thermosyphons and heat pipes. Herein lie the other two objectives of this research.

An overall thermal model of the axial gap motor based on classical heat transfer models will be developed for use in the computerized design tool. Such a model currently does not exist for axial gap motors. Development of such a model is one contribution of this research. Part of the overall thermal model will be the thermal modeling of the radial rotating thermosyphon for rotor cooling. Since there has been no prior research into the thermal behavior of the radial rotating thermosyphon, the thermal model which is developed will be evaluated experimentally. This development of the theory for radial rotating thermosyphons will be another contribution of this research.

- 1-1 Dade, T.B., "Advanced Electric Propulsion, Power Generation, and Power Distribution," *Naval Engineers Journal*, Vol. 106, No. 2, pp. 83-92, March 1994.
- 1-2 Dutton, J.L., "Contrarotating Electric Drive for Attack Submarines," *Naval Engineers Journal*, Vol. 106, No. 2, pp. 45-50, March 1994.
- 1-3 Smith, R.C. & Zavertrnik, T.O., "Overview of U.S. Navy Electric Propulsion Technology," *ICEM '94*, Paris, 1994.
- 1-4 Di Napoli, A., et al., "Design Criteria of a Low-speed Axial-flux PM Synchronous Machine," *International Conference on the Evolution & Modern Aspects of Synchronous Machines, (SM'100)*.
- 1-5 Dunn, P.D., & Reay, D.A., *Heat Pipes*, 4th edition, Pergamon Press, New York, NY, 1994.
- 1-6 Gray, V.H., *The Rotating Heat Pipe*, ASME paper No. 69-HT-19, 1969.
- 1-7 Takeda, Y. et al., "High Torque Variable Reluctance Motor with Axial Construction for Direct Drives," *ICEM '88*, pp. 521-524, 1988.
- 1-8 Varga, J.S., "Magnetic and Dimensional Properties of Axial Induction Motors," *IEEE Transactions*, Vol. EC-1, No. 2, pp. 137-144, June 1986.
- 1-9 Chan, C.C., "Axial-field Electrical Machines - Design and Applications," *IEEE Transactions*, Vol. EC-2, No. 2, pp. 294-300, June 1987.
- 1-10 Desequilles, P.F. et al., "Theoretical and Experimental Results upon Multi-Air-Gap Axial Synchronous Machines with Permanent Magnets," *ICEM '90*, pp. 1066-1070, 1990.
- 1-11 Leung, W.S. & Chan, J.C.C., "A New Design Approach for Axial-Field Electrical Machines," *IEEE Transactions*, Vol. PAS-99, No. 4, pp. 1679-1685, July/Aug. 1980.
- 1-12 Bousbaine, A., "Thermal Modelling of Induction Motors Based on Accurate Loss Density Measurements," *ICEM 1992*.
- 1-13 Elin, D.G., "Calculation of Temperature Distribution in the Windings of Induction Motors," *Electrotehnika*, Vol. 60, No. 3, pp. 12-14, 1989.
- 1-14 Zhu, D.S., et al., "Thermal Model Parameter Identification of an Induction Machine by a Weighted-Least-Square Method," *ICEM 1990*.
- 1-15 Owen, J.M. & Haynes, C.M., "Design Formulae for the Heat Loss and Frictional Resistance of Air-cooled Rotating Discs," *Improvements in Fluid Machines and Systems for Energy Conversion*, Ulrico Hoepli, 1976.

- 1-16 Bradford, M., "The Application of Heat Pipes to Cooling Rotating Electrical Machines,"
- 1-17 Brost, O. et al., "Heat Pipes for Electric Motors," *Fifth International Heat Pipe Conference*, 1984.
- 1-18 Guobiao, Gu, "Research Precess and Prespect of Evaporative Cooling Applied to Hydro-generator," Source of paper unknown. Provided by Prof. Kirtley.
- 1-19 Oslejsek, O., & Polasek, F., "Cooling of Electrical Machines by Heat Pipes," *Second International Heat Pipe Conference*, 1976.
- 1-20 Thoren, F., "Hean Pipe Cooled Induction Motors," *Fifth International Heat Pipe Conference*, 1984.
- 1-21 Cohen, M.A. & Bayley, F.J., "Heat-transfer Problems of Liquid-cooled Gas-turbine Blades," *Proceedings, Institution of Mechanical Engineers*, Vol. 169, pp. 1063-1074, 1956.
- 1-22 Mudawwar, I.A., *Boiling Heat Transfer in Rotating Channels with Reference to Gas Turbine Blade Cooling*, Ph.D. Thesis, M.I.T., 1984.
- 1-23 El-Masri, M.A., *Fluid Mechanics and Heat Transfer in the Blade Channels of a Water-Cooled Gas Turbine*, Ph.D. Thesis, M.I.T., 1979.
- 1-24 Al-Farah, M. et al., "Analysis of Film Condensation in Tilted Thermosyphons," *ASME Paper No. 91-HT-21*, 1991.
- 1-25 Harley, C. & Faghri, A., "Transient Two-Dimensional Analysis of Thermosyphons Including the Falling Condensate Film, *ASME Paper No. 93-WA/HT-17*, 1993.
- 1-26 Reed, J.G. & Tien, C.L., "Modeling of the Two-Phase Closed Thermosyphon," *Transactions of the ASME*, Vol. 109, pp. 722-730, August 1987.
- 1-27 Shiraishi, M. et al., "Investigation of Heat Transfer Characteristics of a Two-phase Closed Thermosyphon," *Advances in Heat Pipe Technology, Proceedings of the 4th International Heat Pipe Conference*, Pergamon, 1982.
- 1-28 Nguyen-Chi, H. & Groll, M., "Entrainment or Flooding Limit in a Closed Two-Phase Thermosyphon," *Advances in Heat Pipe Technology, Proceedings of the 4th International Heat Pipe Conference*, Pergamon, 1982.
- 1-29 Marto, P.J., "Rotating Heat Pipes," *Heat and Mass Transfer in Rotating Machinery*, D.E. Metzger & N.H. Afgan, Eds., Hemisphere, Washington, D.C., 1984.

Chapter 2: Axial Propulsion Motors

Axial gap motors represent a significant departure from conventional radial gap electric motors. Figure 2-1 shows a comparison of the geometry. The primary advantage of this geometry in ship propulsion applications is the ability to increase the active volume of the machine by adding disks which is much more volume efficient than adding length to a conventional radial gap machine. This chapter develops a model of the multi-disk axial gap machine for preliminary design purposes.

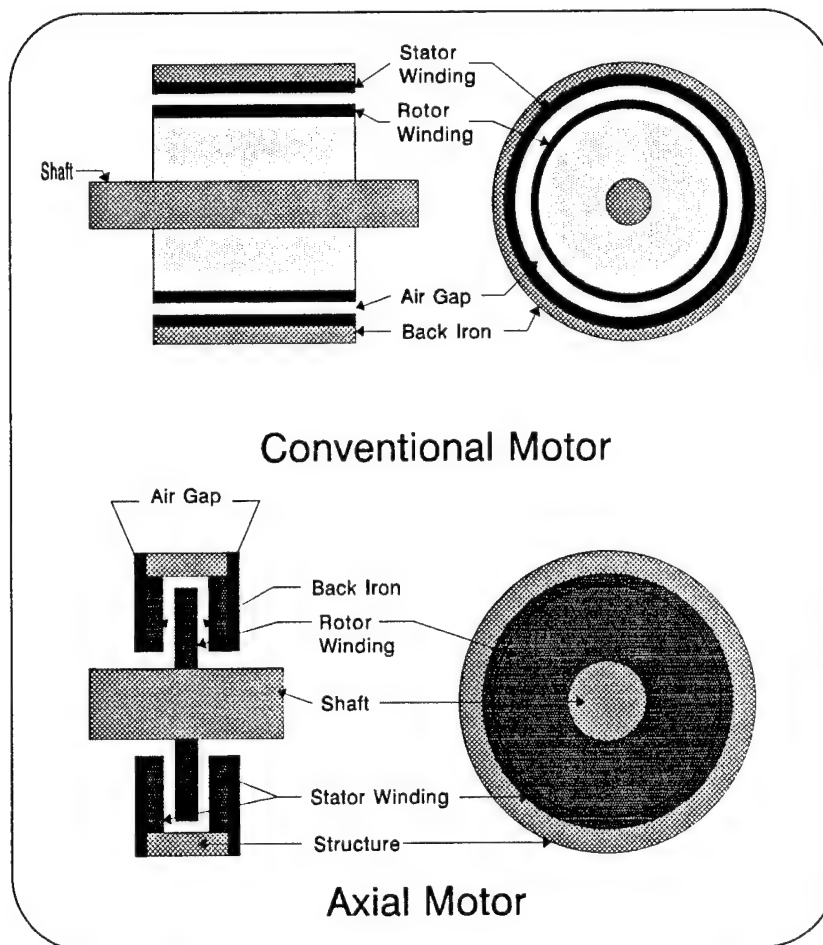


Figure 2-1: Radial Vs Axial Motor Geometry

2.1 Voltage and Current

For the preliminary design analysis of the axial gap machine, only the space fundamental component of the air gap magnetic flux will be considered. The air gap is assumed to be small such that the air gap flux exists in the axial direction only. Under these assumptions, the air gap magnetic flux is given by:

$$B(\alpha) = B_{\max} \sin p(\alpha - \omega t) \quad (2.1)$$

The flux per pole is obtained by integrating equation (2.1) over the active area of the machine:

$$\Phi = \int_0^{\pi/p} \int_{r_i}^{r_o} B(\alpha) r \cdot dr \cdot d\alpha \quad (2.2)$$

the result is:

$$\Phi = (r_o^2 - r_i^2) B_{\max} \cos(p\omega t) \quad (2.3)$$

The terminal voltage can be obtained by recalling that:

$$v = \frac{d\lambda}{dt}, \text{ where } \lambda = \Phi \cdot N_s \cdot S_s, \text{ or in the steady state: } V_{\text{rms}} = \frac{\omega N_s S_s \Phi}{\sqrt{2} p}$$

where N_s is the number of series turns per stator phase and S_s is the number of stators connected in series. The terminal voltage is then:

$$V_{\text{rms}} = \frac{\omega N_s S_s k_b k_p (r_o^2 - r_i^2) B_{\max}}{\sqrt{2} p} \quad (2.4)$$

where the breadth and pitch factors, k_b and k_p , have been introduced to account for distribution and chording of the windings. The breadth and pitch factors are calculated in the same manner as for a conventional radial gap machine. See Fitzgerald, et. al [2-1] for breadth and pitch factor calculation methods.

The phase current is obtained next in terms of the stator current density. From geometric considerations, the current is given by:

$$I_a = \frac{N_{\text{slots}} \cdot A_{\text{slot}}}{6 \cdot N_s} \cdot J_a \cdot S_p \quad (2.5)$$

where S_p is the number of stators connected in parallel. The stator space factor (λ_s) is now defined as the fraction of the stator circumference which contains conductor slots:

$$\lambda_s \equiv \frac{N_{\text{slots}} \cdot w_s}{2\pi r_i} \quad (2.6)$$

where w_s is the width of a stator slot. Note that this parameter has been defined in terms of the inner radius. This avoids the problem of having the teeth go to a zero or negative thickness which could occur if λ_s is defined at the mean or outer radius. The area of one slot is given by:

$$A_{\text{slot}} = h_s \cdot w_s \quad (2.7)$$

Equations (2.6) and (2.7) are then substituted into equation (2.5) to obtain the phase current:

$$I_a = \frac{2\pi r_i \lambda_s}{6N_s} h_s \cdot J_a \cdot S_p \quad (2.8)$$

where the product ($h_s J_a$) is simply the electric loading, K_a . The terminal variables of the machine are now defined by equations (2.4) and (2.8) in terms of the electric loading, magnetic loading and geometric parameters. The power rating of a three-phase machine is then:

$$P = 3 V_a \cdot I_a \cdot \cos(\psi) \quad (2.9)$$

where ψ is the power factor angle.

2.2 Reactance and Resistance

Next, the reactance and resistance values for the windings must be determined.

Only two reactances are considered for preliminary motor design, the synchronous reactance and the leakage reactance due to slot leakage. End-turn leakage, zig-zag leakage and differential leakage reactances are left to a more detailed design analysis. The slot leakage reactance can be calculated by integrating Ampere's Law around the contour shown in Figure 2-2:

$$\oint_c \vec{H} \cdot d\vec{l} = \int_s \vec{J} \cdot \hat{n} dA \quad (2.10)$$

which becomes:

$$H \cdot w_s = J_a \cdot w_s h_s \quad (2.11)$$

The total flux crossing the slot is simply the product of the flux density and the area:

$$\Phi_l = \mu_0 H \cdot h_s (r_o - r_i) \quad (2.12)$$

The leakage reactance is defined by:

$$X_{al} \equiv \frac{\omega N_s \Phi_l}{I_a} \quad (2.13)$$

Equations (2.8), (2.11) and (2.12) are substituted into equation (2.13) to obtain the required expression for the leakage reactance:

$$X_{al} = \frac{6N_s^2 k_b^2 k_p^2 \mu_0 h_s (r_o - r_i)}{2\pi r_i \lambda_s S_p} \quad (2.14)$$

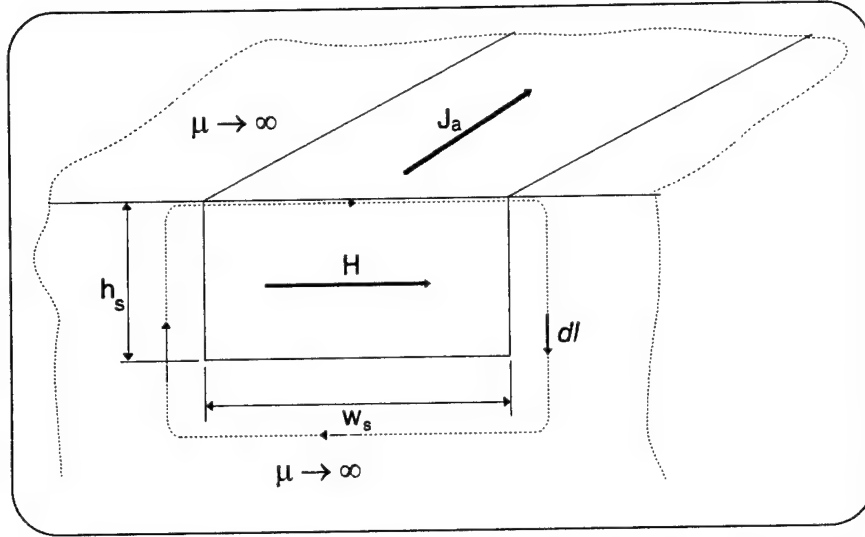


Figure 2-2: Ampere's Law Contour for Slot Leakage Calculation

The synchronous reactance can be obtained by considering the flux linked by the stator winding due to its own excitation. The MMF produced by exciting a single stator phase is:

$$F_{a1} = \frac{4 N_s I_a}{\pi 2p} \sin(p\theta) \quad (2.15)$$

The corresponding flux density in the air gap is:

$$B_z = \frac{2\mu_0 N_s I_a}{\pi g p} \sin(p\theta) \quad (2.16)$$

The flux per pole is found by integrating from the inner radius to the outer radius and over the angle of one pole pitch:

$$\Phi = \int_0^{\pi/p} \int_{r_i}^{r_o} B_z \cdot r \, dr \, d\theta \quad (2.17)$$

Carrying out the integration yields:

$$\Phi = \frac{2\mu_0 N_s I_a (r_o^2 - r_i^2)}{\pi g p^2} \quad (2.18)$$

which gives the phase reactance as:

$$X_{aa0} = \frac{2\mu_0 \omega N_s^2 k_b^2 k_p^2 (r_o^2 - r_i^2)}{\pi g p^2} \quad (2.19)$$

The synchronous reactance for a three-phase machine is determined by:

$$X_d = \frac{3}{2} X_{aa0} + X_{al} \quad (2.20)$$

where X_{aa0} and X_{al} are given by equations (2.14) and (2.19). The synchronous reactance is per-unitized by dividing equation (2.20) by the base impedance:

$$Z_b = \frac{V_b}{I_b} \quad (2.21)$$

where V_b and I_b are the base voltage and current, respectively.

The required field excitation for the motor is determined from the phasor diagram at rated conditions, see Figure 2-3. Assuming the base voltage and current are the rated values, the per unit field excitation is:

$$e_{af} = \sqrt{1 + x_d^2 + 2x_d \sin(\psi)} \quad (2.22)$$

The field current required to develop rated voltage at no load is:

$$I_{f1} = \frac{\pi B_{max} p g}{2\mu_0 k_f N_f} \quad (2.23)$$

where k_f is the field winding factor and N_f is the number of series turns in the field winding referred to the stator. The rated field current is then:

$$I_f = I_{f1} \cdot e_{af} \quad (2.24)$$

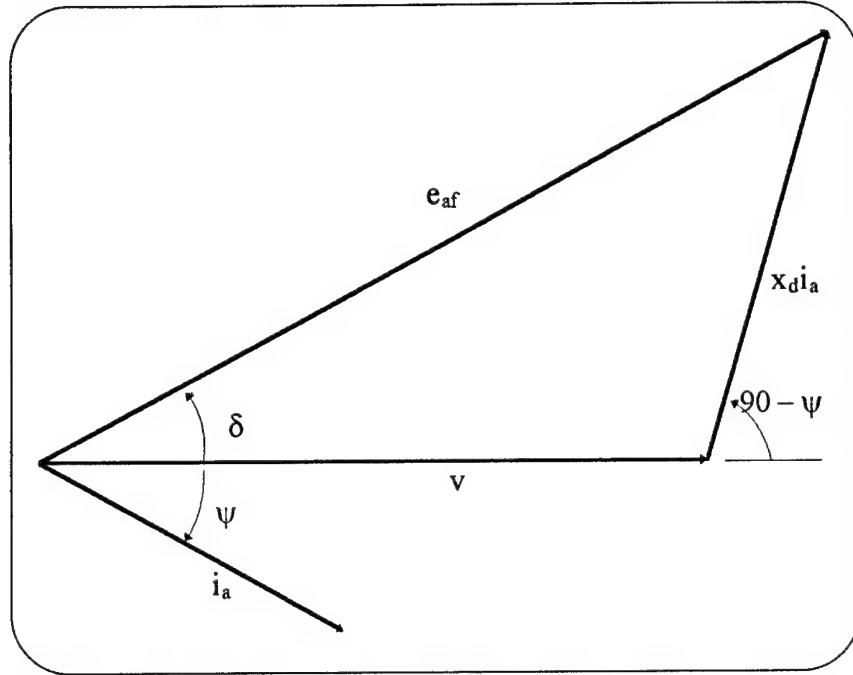


Figure 2-3: Phasor Diagram at Rated Conditions

Finally, the field current density is given by:

$$J_f = \frac{N_f I_f}{\pi r_i \lambda_r h_r} \quad (2.25)$$

where λ_r is the rotor space factor corresponding to λ_s on the stator and h_r is the rotor slot height.

The turn length must be determined in order to calculate the winding resistances. Figure 2-4 shows the typical winding geometry for an axial gap machine. As a starting point, the end turns are assumed to be triangular with approximately 45 degree bend angles. Although this is not exact, it is a good approximation for a motor with a large number of poles as are being considered. This gives the turn length as:

$$L_t = 2(r_o - r_i) + \sqrt{2} (r_o + r_i) \alpha \quad (2.26)$$

where α is the angle between corresponding sides of a coil and is given by: $\alpha = \frac{\pi}{p} \cdot \text{pitch}$.

Equation (2.26) holds for both the stator and rotor windings where "pitch" is the

fractional pitch (i.e.. 5/6 pitch) which is unity for the field winding. The resistance for one turn of a coil is:

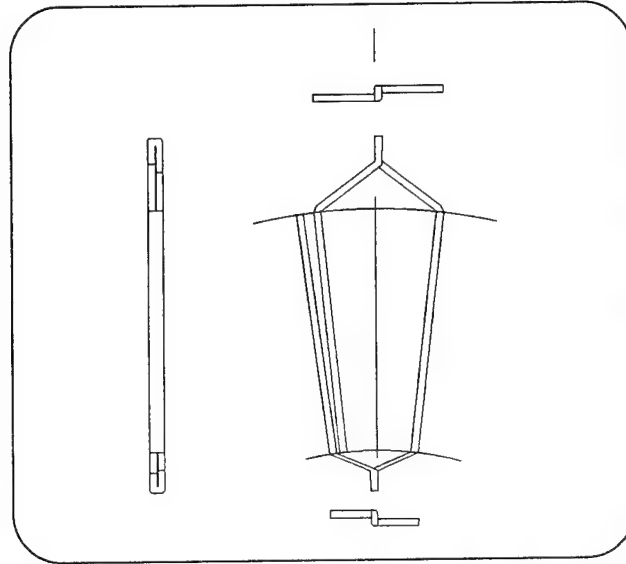


Figure 2-4: End Turn Geometry (Armature Winding Shown)

$$R_t = \frac{L_t}{\sigma_{cu} A_{wire}} \quad (2.27)$$

where σ_{cu} is the conductivity of copper [mho/m]. A_{wire} is the cross-sectional area of one turn of the winding and is given by:

$$A_{wire} = \frac{2\pi r_i h_s \lambda_s SSF}{2N_s \cdot m} \quad (2.28)$$

where m is the number of phases and SSF is the fraction of the slot cross-section which contains conductors. The stator space factor (SSF) and slot height are replaced with their respective rotor values for the field winding. The winding resistance is then found from:

$$R = R_t N_s S_s \quad (2.29)$$

Combining equations (2.27) - (2.29) yields:

$$R = \frac{m L_t \cdot N_s^2 \cdot S_s}{\sigma_{cu} \pi r_i \lambda_s h_s \cdot SSF} \quad (2.30)$$

Equation (2.30) is valid for either stator or rotor windings when the appropriate values are used.

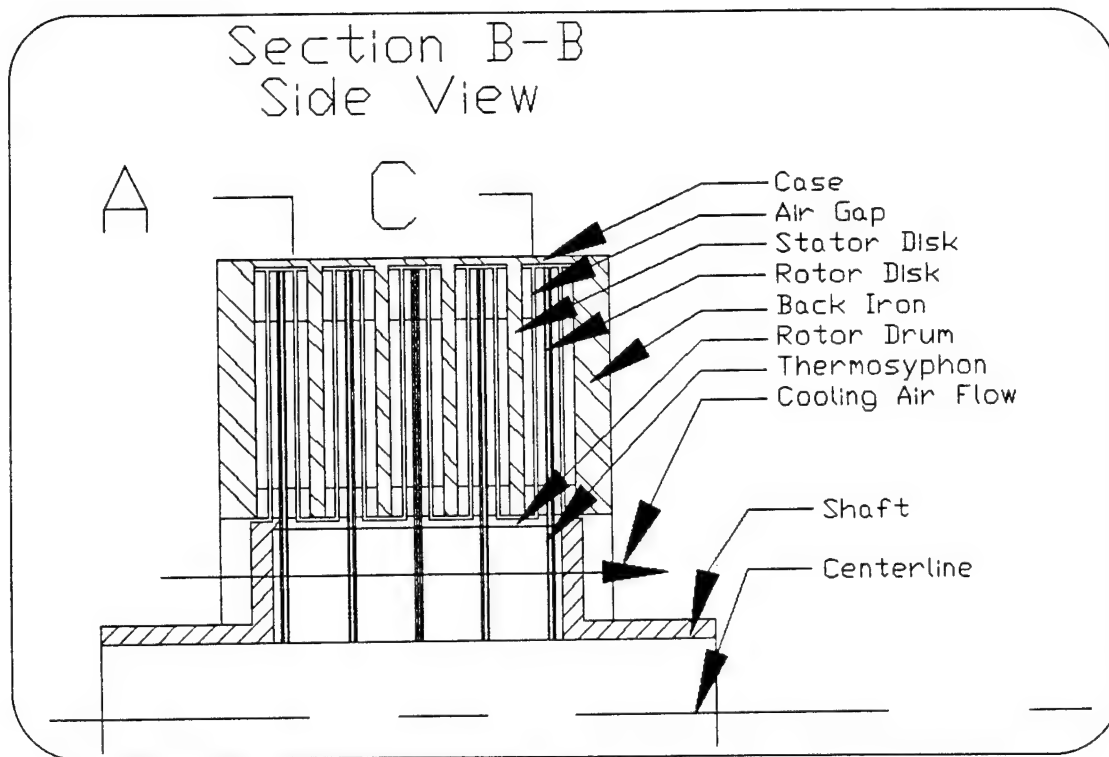


Figure 2-5: Section View of Motor

2.3 Structural Design

For preliminary design purposes, the structural design of the motor will consider only the major components of the machine. Specifically, the shaft, rotor disks, stator disks and case are sized based upon classical engineering mechanics. While an analytical analysis such as this is rather simplistic in nature, it serves the purpose of generating reasonable dimensions for comparison purposes in the preliminary design stage. Figures 2-5 and 2-6 depict the geometry under consideration.

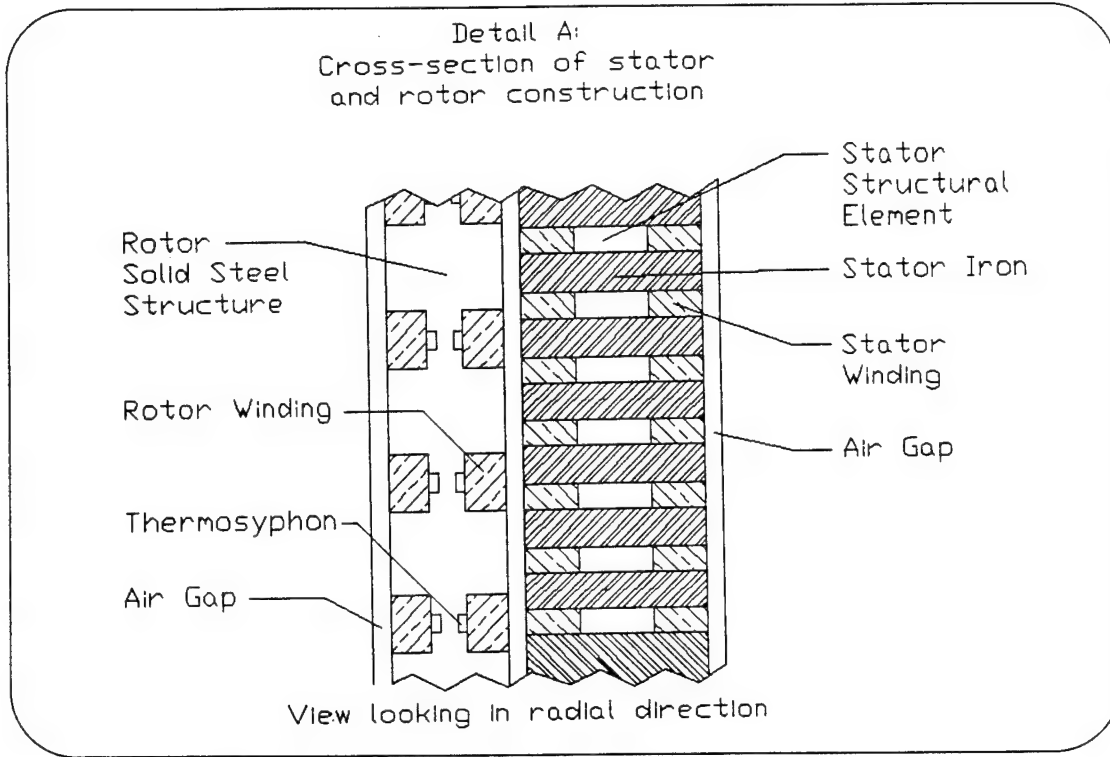


Figure 2-6: Detail of Stator and Rotor Construction

The shaft is modeled as a hollow steel tube subjected to torsional loading. Popov [2-2] provides a simple design formula based upon purely elastic behavior:

$$\frac{2 \cdot I_p}{d_o} = \frac{T}{\tau_{\max}} \quad (2.31)$$

where d_o is the outer diameter of the shaft, T is the load torque, τ_{\max} is the maximum allowable shear stress of the material and I_p is the polar moment of inertia which is given by:

$$I_p = \frac{\pi}{32} (d_o^4 - d_i^4) \quad (2.32)$$

for a hollow cylinder. Torque is equal to P/Ω , so if we assume that $d_i = 0.8d_o$ then the equations (2.31) and (2.32) can be combined and solved for d_o as:

$$d_o = 2.05 \left(\frac{P}{\Omega \tau_{\max}} \right)^{1/3} \quad (2.33).$$

For design purposes, τ_{\max} for steel is assumed to be 100 MPa.

The stator and rotor disks must be strong enough to transmit the electromagnetic torque to the motor case and shaft, respectively. The required area for transmitting the torque from the disk to the drum or case is found from:

$$A_D = \frac{T_D}{r \cdot \tau_{\max}} \quad (2.34)$$

where r is the inner radius for rotor disks and the outer radius for stator disks and T_D is the torque per disk. The rotor is constructed from solid steel, so τ_{\max} for the rotor will be that of steel. The structural portion of the stator disk is constructed from a composite material whose maximum shear stress is about 14 MPa. T_D is determined from the rated power, speed and number of disks as:

$$T_D = \frac{2 \cdot P}{\Omega \cdot N_g} \quad (2.35).$$

The required disk thickness is then determined from:

$$t_D = \frac{A_D}{2\pi r} \quad (2.36)$$

For the stator, r will be:

$$r_{oo} = r_o + \frac{\text{stator pitch}}{2} \quad (2.37)$$

to account for the end turns. Similarly, for the rotor r is given by:

$$r_{ii} = r_i - \frac{\text{rotor pitch}}{2} \quad (2.38)$$

In the region of the rotor disks, the shaft outer diameter is increased to that of the inner diameter of the rotor disks, creating effectively a "drum" region to support the rotor disks. This is done both to reduce rotor weight and to allow more space for cooling devices in the inner region of the machine. Equations (2.31) and (2.32) can be solved for the drum inner diameter in terms of the known outer diameter. The result is:

$$d_{ir} = \left[d_{or}^4 - \frac{16d_{or}}{\pi} \frac{T}{\tau_{max}} \right]^{1/4} \quad (2.39)$$

where τ_{max} is the maximum shear stress for steel and equation (2.38) determines the radius corresponding to d_{or} .

The case that supports the stator disks is sized in a similar manner and is also constructed of steel. Unfortunately, d_i is now known and d_o is the unknown in equations (2.31) and (2.32). The inner diameter is twice the radius given in equation (2.37). The result is an implicit equation in terms of the outer diameter:

$$d_{os}^4 - \frac{T}{\tau_{max}} \frac{16}{\pi} d_{os} = d_{is}^4 \quad (2.40)$$

An implicit equation is not the preferred result, but it is easily handled in the design spreadsheet. This is discussed further in Section 5.1.

This simple structural analysis doesn't begin to address all the concerns of designing a motor, but it does allow rationally based sizing of the major structural components of the motor. Obviously, a more complete structural analysis which considers deflection of the various components, stress concentration due to geometry changes and a

dynamic analysis to determine shaft critical speeds should be performed before proceeding further with any motor design.

2.4 Weight and Volume

An estimate of the weight and volume of a particular design must be obtained in order to make comparisons of various machine designs. For preliminary design purposes, only the electromagnetic and structural components of the motor are considered in these estimates.

The stator winding volume is calculated from:

$$V_{scu} = L_t h_s \pi r_i \lambda_s N_s \quad (2.41)$$

and the rotor winding volume is similar with the appropriate rotor values substituted for the stator parameters. The windings are imbedded into slots in magnetic iron on both the rotor and stator disks. The volume of the stator magnetic material can be approximated by:

$$V_{si} = \pi (r_o^2 - r_i^2) (1 - \lambda_s) N_s \cdot (2h_s + t_s) \quad (2.42)$$

where λ_s is the stator space factor defined by equation (2.6), h_s is the stator slot height and t_s is the disk structural thickness determined from equation (2.36). Since the density of the structural composite portion of the stator is small, its volume is not calculated explicitly. The stator case volume is given by:

$$V_{case} = \frac{\pi}{4} (d_{os}^2 - d_{is}^2) \cdot L \quad (2.43)$$

where d_{os} is the case outer diameter calculated in equation (2.40), d_{is} is twice r_{oo} from equation (2.37) and L is the stack length of equation (2.49).

The rotor volume is calculated as the sum of the disks and the drum. This volume is:

$$v_{ri} = \pi \left[(r_{oo}^2 - r_{ii}^2) \cdot t_r + (r_o^2 - r_i^2) \cdot 2h_r \right] \cdot N_r - v_{rcu} + \frac{\pi}{4} (d_{or}^2 - d_{ir}^2) \cdot L \quad (2.44)$$

where r_{oo} and r_{ii} are the structural radii determined from equations (2.37) and (2.38), respectively. d_{or} is simply twice r_{ii} and equation (2.39) determines d_{ir} .

There must be back iron at both ends of the machine to provide a return path for the magnetic flux. The thickness of the back iron is determined from saturation limits in the iron and the desired flux density in the air gap. In the air gap, the flux per pole is:

$$\Phi = \frac{(r_o^2 - r_i^2) B_{ag}}{p} \quad (2.45)$$

where B_{ag} is the flux density in the air gap. In the back iron, the flux per pole is:

$$\Phi = (r_o - r_i) B_{sat} t \quad (2.46)$$

which must be the same flux as that given in equation (2.45). Equating these fluxes and solving for the back iron thickness results in:

$$t_b = \frac{B_{ag}}{B_{sat}} \cdot \left(\frac{r_o + r_i}{p} \right) \quad (2.47).$$

The back-iron thickness is inversely proportional to the number of pole pairs. The back-iron volume is then:

$$v_{bi} = 2\pi (r_o^2 - r_i^2) \cdot t_b \quad (2.48).$$

Another important parameter is the stack length of the axial machine. The stack length (L) is:

$$L = N_r(t_r + 2h_r) + N_s(t_s + 2h_s) + 2t_b + N_g g \quad (2.49)$$

In all designs currently being considered, N_r , N_s and N_g will be equal.

The weight of the machine is simply the summation of the various volumes multiplied by the appropriate density of the component materials.

2.5 Losses and Efficiency

There are several loss mechanisms in electric motors. The primary ones are the winding loss, core loss, windage and friction loss. These three mechanisms are considered in this analysis. Winding loss is simply the I^2R loss associated with the current passing through the armature and field windings. This is calculated as:

$$P_w = 3I_a^2 R_a + I_f^2 R_f \quad (2.50)$$

for a three-phase machine. Winding loss is the single largest loss component. This is fortunate as this is the only loss mechanism which can be calculated in a straightforward manner.

Core loss arises from eddy currents induced in the magnetic materials of the machine by the magnetic fields created in the windings. The specific core loss is a function of flux density in the core, electrical frequency, lamination thickness and resistivity of the core material. Walker [2-3] provides empirical graphical relationships for core loss as a function of lamination thickness, electrical frequency, steel grade and flux density in the core. For the typical values of 1.3 T flux density at 60 Hz in 0.5 mm laminations of grade 170 steel, the specific core loss is approximately 33 KW/m³ from his graphs. The total

core loss for a particular machine is the product of this specific core loss and the volume of the core material. To account for hysteresis effects, the total core loss is multiplied by an empirical factor of 1.55.

Windage and friction losses arise from the motion of the rotor. Air in the air gap and the bearings which support the rotor both cause a drag on the rotor as it rotates. However, due to the very slow speed of the propulsion motors being considered, this loss is very small in comparison to the other loss mechanisms described above and can be ignored.

The efficiency (η) of the machine is then given as the ratio of the power output to the power input. This can be written as:

$$\eta = 1 - \frac{\sum P_{\text{losses}}}{P_{\text{in}}} \quad (2.51)$$

where $\sum P_{\text{losses}}$ is the summation of the winding and core losses. P_{in} is the power input to the motor terminals.

2.6 Heat Transfer

Heat transfer to the surroundings is the method by which all losses are ultimately dissipated. There are several paths through which heat may be transferred out of the machine, all of which act in parallel. Some of these paths occur naturally such as conduction out of the shaft or natural convection off the outer casing. The most important paths are the ones designed into the machine specifically for the purpose of cooling the heat generating parts. This cooling is provided via the air gap and any liquid or gas cooling passages designed into the machine to cool the windings.

2.6.1 Air Gap Heat Transfer

Virtually all electric machines push air (or some fluid) through the air gap to provide cooling to the machine. In this respect, the axial motor is no different. However, the geometry of the air gap is significantly different from a conventional radial gap machine. This section examines heat transfer in the axial geometry air gap.

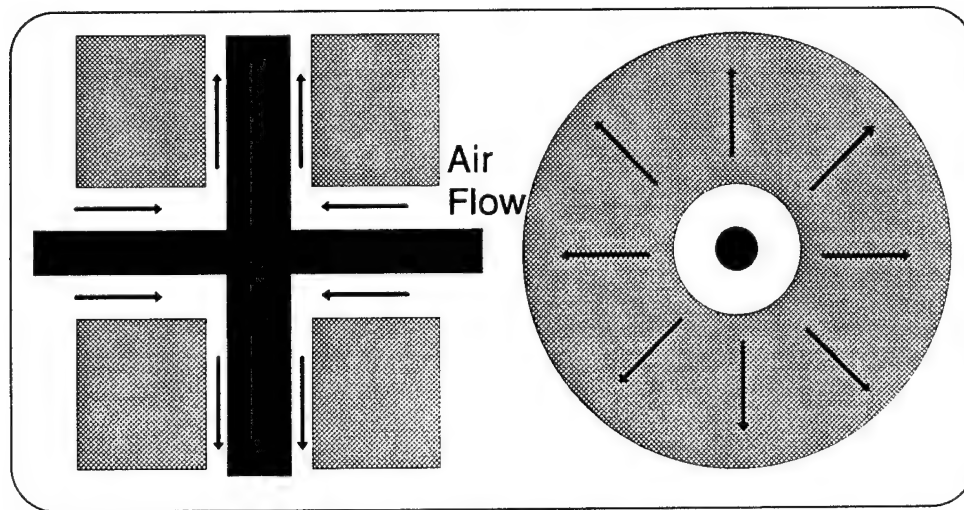


Figure 2-7: Axial Gap geometry

The geometry of the axial gap motor is depicted in Figure 2-7. This heat transfer problem has been studied in gas turbine rotor cooling applications. Owen [2-4] provides a review of the theoretical and experimental work done in this area. The heat transfer in the rotor-stator system depends primarily on the rotation rate, gap ratio and the amount of throughflow. The rotation rate is measured via the Rotational Reynolds Number:

$$Re_{\theta} = \frac{\omega r_o^2}{\nu}$$

where ω is the rotational speed, r_o is the outer disk radius and ν is the kinematic viscosity.

The gap ratio (G) is defined as the ratio of the axial spacing between the rotor and stator and the outer radius of the rotor:

$$G = \frac{g}{r_o}$$

where g is the gap length. The amount of throughflow, \dot{Q} is given by:

$$\dot{Q} = 2\pi r_i g V_s$$

and is typically non-dimensionalized as the flow coefficient, C_w :

$$C_w = \frac{\dot{Q}}{r_o V}$$

The throughflow can also be non-dimensionalized as the radial Reynolds number, Re_r :

$$Re_r = \frac{\dot{Q}}{\nu D_h}$$

for comparison with the rotational flow. D_h is the hydraulic diameter which is defined as four times the cross-sectional flow area divided by the wetted perimeter:

$$D_h = \frac{4A_c}{P} = \frac{4 \cdot 2\pi r g}{4\pi r} = 2g$$

and is twice the gap length for the geometry under consideration.

For heat transfer between the rotor and the air, the heat transfer coefficient is defined non-dimensionally by the Nusselt number:

$$Nu_r = \frac{h_r r_o}{k} = 0.145 \left(\frac{C_w}{G} \right)^{0.8} \quad (2.52)$$

where h_r is the dimensional heat transfer coefficient for the rotor with SI units of [Watts/(meter²-°C)] and k is the thermal conductivity of the fluid in the air gap. The total heat transfer from the rotor is:

$$Q = h_r \cdot A \cdot (T_r - T_{in}) \quad (2.53)$$

where A is the surface area of the rotor, T_r is the rotor temperature and T_{in} is the inlet air temperature. Similarly, the heat transfer coefficient for the stator is defined by:

$$Nu_s = \frac{h_s r_o}{k} = 0.76 \cdot C_w^{0.57} \cdot G^{-0.32} \quad (2.54).$$

The total heat transfer between the stator and air gap is calculated using (2.53) when the appropriate stator values are used. Equations (2.52) and (2.54) were developed by Owen [2-4].

2.6.2 Direct Water Cooling

Direct water cooling is one of the most effective winding cooling methods used today. As the name implies, the cooling water comes into direct contact with the windings of the machine. This is accomplished by using hollow conductors and pumping the cooling water through them. Because the heat generated in the windings does not have to be conducted through electrical insulation before reaching the cooling water, this method is very attractive for high voltage machines which have thick winding insulation. The drawback to this method is that the cooling water must span the potential difference between ground and the winding voltage. This requires very high purity water, which from a shipboard maintenance standpoint is a serious deficiency.

2.6.3 Indirect Water Cooling

Indirect water cooling is similar to direct water cooling except the cooling water stays outside the electrical insulation. The advantage of this method is that the high purity water requirements of direct water cooling are no longer required. The disadvantage is that heat must be transferred through the electrical insulation before reaching the cooling water. For a given maximum winding temperature, this reduces the allowable temperature rise of the cooling water. The motor must be designed with larger cooling passages and lower current densities which increases the machine size.

2.6.4 Hydrogen Cooling

While water cooling is very effective for stator cooling, the hydrostatic pressure caused by the centrifugal force of rotation makes it impractical for rotor cooling in most applications. Hydrogen, due to its low density and very high specific heat, is very well suited to rotor cooling. Hydrogen is passed through hollow conductors in a direct cooling mode or it can be used in lieu of air in the air gap and indirect cooling passages built into the machine. This cooling method is common in large turbine generators. The drawback of this method is the flammability and explosive nature of hydrogen gas. This potential safety hazard makes hydrogen cooling unacceptable for shipboard use.

2.6.5 Air Cooling

The advantage of air cooling is that it is simple and reliable. Lower heat transfer coefficients are obtained than with other methods. Current densities are necessarily

limited to much lower values, resulting in a much larger and heavier machine. Air-cooled motors do not provide the high power densities needed in ship propulsion applications.

2.6.6 Two-Phase Cooling Methods

All of the winding cooling schemes previously described have relied upon transferring heat from the windings to a cooling medium via sensible heat, or increasing the temperature of the coolant. Two-phase cooling relies on the heat of vaporization of the coolant to remove heat from the windings. There are two advantages of this cooling method. First, the large heat transfer coefficients obtained via boiling of the coolant allow higher heat fluxes into the coolant. Second, the need for a temperature difference in the coolant is virtually eliminated, allowing the designer to use more of the total allowable temperature difference for conduction through the electrical insulation to the coolant.

While two-phase cooling has been previously used to cool conventional machines, it has yet to be considered for cooling axial gap machines. The designs developed for this thesis use two-phase rotating thermosyphons to cool the rotor windings. Development of the necessary design equations is deferred to Chapter 3.

- 2-1 Fitzgerald, A.E., Kingsley, C., Umans, S.D., *Electric Machinery, 5th ed.*, McGraw-Hill, 1990.
- 2-2 Popov, E.P., *Mechanics of Materials*, Prentice-Hall, 1978.
- 2-3 Walker, J.H., *Large A.C. Machines, Design, Manufacture and Operation*, BHEL, New Delhi, India, 1979.
- 2-4 Owen, J.M. & Haynes, C.M., "Design Formulae for the Heat Loss and Frictional Resistance of Air-cooled Rotating Discs," *Improvements in Fluid Machines and Systems for Energy Conversion*, Ulrico Hoepli, 1976.

Chapter 3: Radial Rotating Thermosyphons

There are essentially three heat transfer processes which occur within the radial rotating thermosyphon (RRT). These are film condensation, film evaporation and pool boiling. This chapter develops a description for these processes which is applicable to the RRT and also investigates the limits to thermosyphon performance as applied to the RRT.

3.1 Film Condensation

The classical heat transfer problem of film condensation of a vapor on a vertical wall is known as a Nusselt analysis and is treated in any introductory heat transfer text such as Mills [3.1]. The primary assumptions built into the Nusselt analysis are that the inertia of the film is neglected and the temperature profile is linear. The effects of vapor superheat, liquid subcooling and vapor velocity are also neglected. While seemingly quite restrictive, the standard Nusselt type analysis gives good results in many applications. In the RRT, gravitational force is replaced by the centrifugal force of rotation which may be one or two orders of magnitude larger and varies with radius. If the cross-sectional area is very small, the vapor velocity may become significant at higher heat transfer rates. With these differences in mind, this section develops a Nusselt type analysis that is valid for the variable centrifugal force found in the RRT. The momentum and energy equations are then evaluated to determine the range of validity of this solution.

Analysis of film condensation begins by looking at an elemental volume of fluid within the film (see Figure 3-1). A force balance per unit width on this element in the radial or x-direction yields:

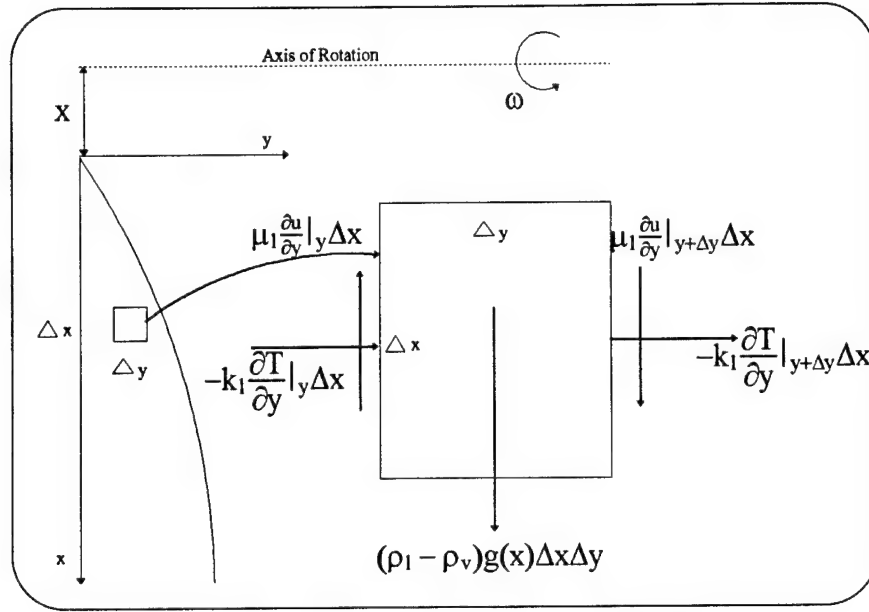


Figure 3-1: Elemental Film Volume

$$\sum F_x = 0 = \mu_1 \frac{\partial u}{\partial y} \Big|_y \Delta x - \mu_1 \frac{\partial u}{\partial y} \Big|_{y+\Delta y} \Delta x - (\rho_l - \rho_v)g(x)\Delta x \Delta y.$$

After rearranging and taking limits, this becomes:

$$\mu_1 \frac{\partial^2 u}{\partial y^2} + (\rho_l - \rho_v)g(x) = 0 \quad (3.1)$$

This differential equation for the velocity profile is subject to the boundary conditions:

$$u(y = 0) = 0 \text{ (no slip at wall)}$$

$$\text{and } \frac{\partial u}{\partial y} = 0 \text{ @ } y = \delta \text{ (neglect interfacial shear stress).}$$

Equation (3.1) can be directly integrated to yield the film velocity profile:

$$u(x, y) = \frac{(\rho_l - \rho_v)g(x)}{2\mu_1} (2\delta y - y^2) \quad (3.2)$$

The mass flow rate of the film per unit width (Γ) is obtained by integrating equation (3.2) across the film thickness:

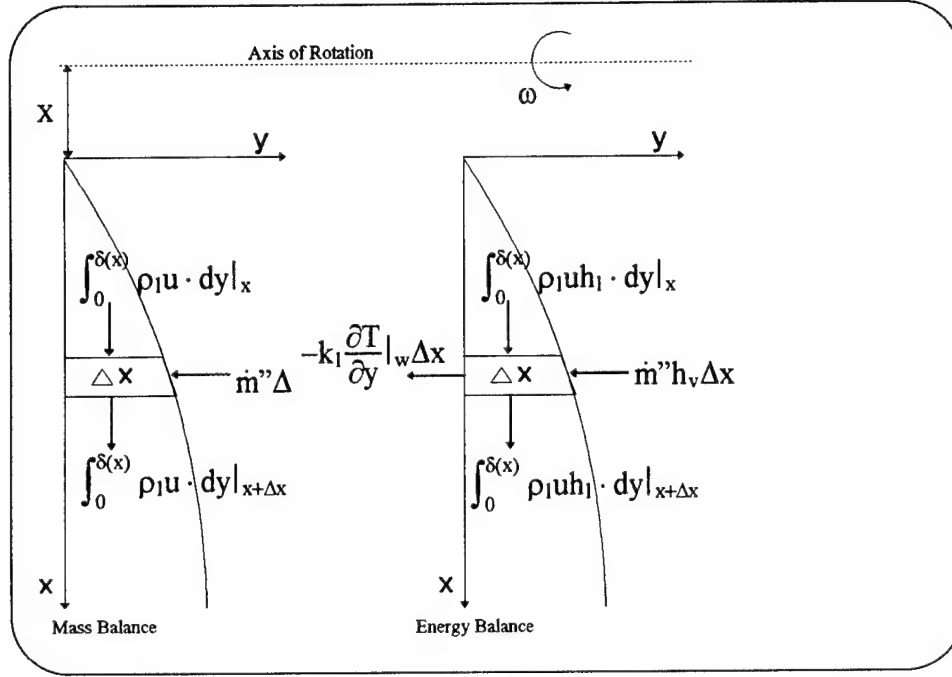


Figure 3-2: Energy & Mass Balance on Film Strip

$$\Gamma = \int_0^{\delta} \rho_1 u(x, y) \cdot dy = \frac{g(x)(\rho_l - \rho_v)\delta^3}{3\nu_l} \quad [\text{kg/m-s}] \quad (3.3)$$

The film Reynolds number (Re) is defined as:

$$\text{Re} = \frac{4\Gamma}{\mu_l} \quad (3.4)$$

Equations (3.3) and (3.4) can be re-arranged to give the film thickness (δ) in terms of the film Reynolds number:

$$\delta = \left[\frac{3\mu_l \nu_l \text{Re}}{4(\rho_l - \rho_v)g(x)} \right]^{1/3} \quad (3.5).$$

An energy balance on the film element of Figure 3-1 results in the differential equation:

$$\frac{\partial^2 T}{\partial y^2} = 0 \quad (3.6)$$

which is subject to the boundary conditions:

$$\begin{aligned} T(y = \delta) &= T_{\text{sat}} \\ T(y = 0) &= T_w. \end{aligned}$$

Integrating equation (3.6) results in the linear temperature profile:

$$T - T_w = \frac{y}{\delta}(T_{\text{sat}} - T_w)$$

which indicates that heat is simply conducted through the liquid film. The heat flow through the film is given by:

$$q = k_l \frac{\partial T}{\partial y} \Big|_{y=0} \equiv h(T_{\text{sat}} - T_w) \quad (3.7)$$

where the local condensation heat transfer coefficient has been defined in terms of the heat flux and the temperature difference across the film. A mass balance on a thin strip of the liquid film as depicted in Figure 3-2 shows:

$$\int_0^\delta \rho_l u(x, y) \cdot dy \Big|_x + \dot{m}'' \cdot \Delta x - \int_0^\delta \rho_l u(x, y) \cdot dy \Big|_{x+\Delta x} = 0$$

this can be solved for the condensation rate:

$$\dot{m}'' = \frac{d}{dx} \int_0^\delta \rho_l u(x, y) \cdot dy = \frac{d\Gamma}{dx} \quad (3.8).$$

An energy balance on the same element of Figure 3-2 shows:

$$\int_0^\delta \rho_l u(x, y) h_l \cdot dy \Big|_x + \dot{m}'' h_v \cdot \Delta x - \int_0^\delta \rho_l u(x, y) h_l \cdot dy \Big|_{x+\Delta x} - k_l \frac{\partial T}{\partial y} \Big|_{y=0} = 0.$$

If subcooling of the liquid film is neglected and a constant specific heat is assumed, then:

$$k_l \frac{\partial T}{\partial y} \Big|_{y=0} = \frac{d\Gamma}{dx} \cdot h_{fg} \quad (3.9).$$

Now, equations (3.4), (3.7) and (3.9) can be combined:

$$h(T_{\text{sat}} - T_w) = h_{fg} \frac{\mu_l}{4} \cdot \frac{d\text{Re}}{dx} \quad (3.10).$$

For the radial rotating thermosyphon, the Nusselt number is defined by:

$$\text{Nu} \equiv \frac{h\sqrt{v/\omega}}{k_l} \quad (3.11)$$

where $\sqrt{v/\omega}$ is taken as the characteristic length scale. Equation (3.10) can now be written as:

$$\frac{dx}{\sqrt{v_l/\omega}} = \frac{\text{Pr}}{4\text{Ja}} \cdot \frac{d\text{Re}}{\text{Nu}} \quad (3.12)$$

where the Prandtl number and Jakob number have been defined as: $\text{Pr} = \frac{C_p \mu_l}{k_l}$ and $\text{Ja} = \frac{C_p(T_{\text{sat}} - T_w)}{h_{fg}}$, respectively. An energy balance on the entire film from $x = 0$ to $x = L_c$ shows:

$$\bar{h}L_c(T_{\text{sat}} - T_w) = \Gamma_L \cdot h_{fg} = \frac{\mu_l h_{fg}}{4} \text{Re}_{L_c}$$

and the average Nusselt number is defined as: $\bar{\text{Nu}} \equiv \frac{\bar{h}\sqrt{v_l/\omega}}{k_l}$ which can now be written

in terms of the exit Reynolds number:

$$\bar{\text{Nu}} = \frac{\sqrt{v_l/\omega}}{L_c} \left(\frac{\text{Pr}}{4\text{Ja}} \right) \text{Re}_{L_c} \quad (3.13).$$

The difference between the gravitational and centrifugal forces can be accounted for using the method presented by Dhir & Lienhard [3.2] which uses an effective gravity. Using their method, the film thickness is given by:

$$\delta = \left[\frac{4\mu_l k_l (T_{\text{sat}} - T_w) x}{(\rho_l - \rho_v) \rho_l h_{fg} g_{\text{eff}}} \right]^{1/4} \quad (3.14)$$

$$\text{where: } g_{\text{eff}} \equiv \frac{x(gR)^{4/3}}{\int_0^x g^{1/3} R^{4/3} dx} \quad (3.15)$$

The local Nusselt number is given by:

$$\text{Nu} = \frac{h \sqrt{v_l/\omega}}{k} = \left[\frac{(\rho_l - \rho_v) h'_{fg} x^3}{g_{\text{eff}} 4v_l k_l (T_{\text{sat}} - T_w)} \right]^{1/4} \quad (3.16)$$

For the case of the RRT, $g(x) = r\omega^2 = X_c\omega^2 + x\omega^2$ where X_c is the distance from the axis of rotation to the top of the condenser and x is the distance down from the top of the condenser. The radius of curvature ($R(x)$) is infinite for a flat surface. The resulting effective gravity is:

$$g_{\text{eff}} = \frac{4x\omega^2/3}{1 - [X_c/(X_c + x)]^{4/3}} \quad (3.17)$$

and for $\rho_l \gg \rho_v$, the local Nusselt number becomes:

$$\text{Nu} = \left(\frac{X_c + x}{\sqrt{v_l/\omega}} \right)^{1/3} \cdot \left(\frac{3}{4} \text{Re} \right)^{-1/3} \quad (3.18)$$

The average Nusselt number is obtained from equation (3.13). First, the exit Reynolds number must be found by substituting equation (3.18) into (3.12) and integrating along the length of the condenser.

$$\int_0^{L_c} (X_c + x)^{1/3} \cdot dx = \frac{\text{Pr}}{4\text{Ja}} \cdot \left(\sqrt{v_l/\omega} \right)^{4/3} \cdot \int_0^{\text{Re}_{Lc}} \left(\frac{3}{4} \text{Re} \right)^{1/3} \cdot d\text{Re}$$

which integrates out to:

$$\text{Re}_{L_c} = \frac{4}{3} \left[\frac{(X_c + L_c)^{4/3} - X_c^{4/3}}{(\sqrt{v_l/\omega})} \cdot \frac{3\text{Ja}}{\text{Pr}} \right]^{3/4} \quad (3.19)$$

Equation (3.19) is substituted into equation (3.13) to obtain the average Nusselt number:

$$\overline{\text{Nu}} = \left(\frac{\text{Pr}}{3\text{Ja}} \right)^{1/4} \cdot \frac{[(X_c + L_c)^{4/3} - X_c^{4/3}]^{3/4}}{L_c} = \frac{\bar{h}\sqrt{v_l/\omega}}{k_l} \quad (3.20).$$

Equation (3.20) can be used to estimate the heat transfer coefficient in the condenser of the radial rotating thermosyphon. A Nusselt number based on condenser length can also be defined as:

$$\overline{\text{Nu}}_{L_c} = \frac{\bar{h}L_c}{k_l} = \left(\frac{\text{Pr}}{3\text{Ja}} \right)^{1/4} \left[\frac{(X_c + L_c)^{4/3} - X_c^{4/3}}{(\sqrt{v_l/\omega})^{4/3}} \right]^{3/4} \quad (3.21).$$

An important effect that has not been included in this result is the Coriolis force.

This is treated later. Subcooling, which has also been neglected can be accounted for by replacing the latent heat with a corrected latent heat given by:

$$h'_{fg} = h_{fg} + 0.68C_p(T_{\text{sat}} - T_w).$$

The above analysis is limited to laminar flow which occurs when the film Reynolds number is less than 30.

For the wavy laminar regime in gravitational systems, the empirical relationship of Chun & Seban [3.3] is commonly used to predict the heat transfer coefficient. Their relationship is given by:

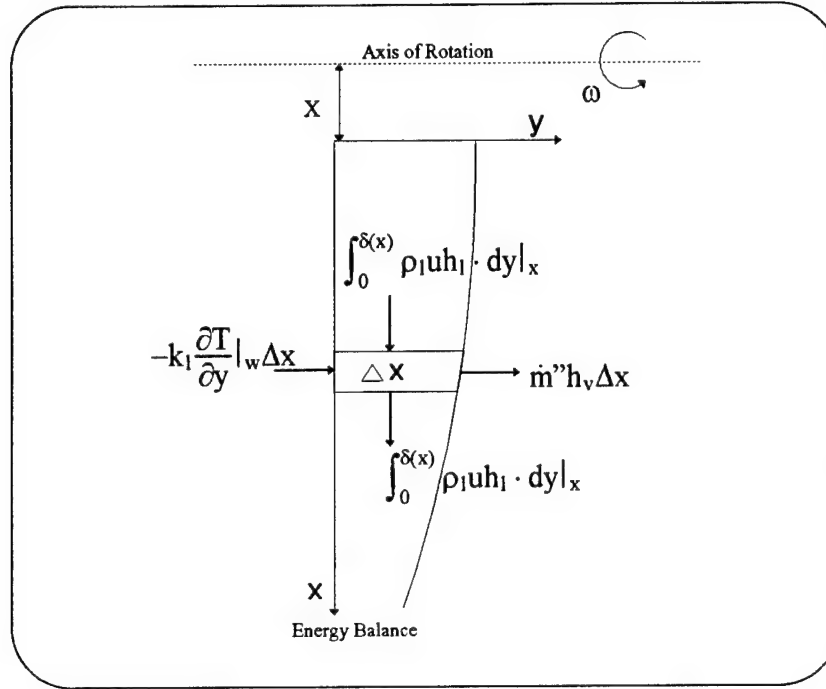


Figure 3-3: Evaporating film

$$Nu' = \frac{h \sqrt[3]{g/v_l^2}}{k_l} = 0.822 Re^{-0.22} \quad (3.22).$$

For use in rotational systems, the length scale is changed to $\sqrt{v_l/\omega}$. The resulting local Nusselt number is:

$$Nu = 0.822 Re^{-0.22} \left(\frac{X_c + x}{\sqrt{v_l/\omega}} \right)^{1/3} \quad (3.23)$$

Equation (3.23) is then substituted into equation (3.12) and integrated over the length of the condenser to obtain the condenser exit Reynolds number:

$$Re_{Lc} = \left(\frac{3Ja}{Pr} \cdot \frac{[(X_c + L_c)^{4/3} - X_c^{4/3}]}{(\sqrt{v_l/\omega})^{4/3}} \right)^{0.82} \quad (3.24).$$

The average Nusselt number is then found from equation (3.13) to be:

$$\overline{Nu} = \frac{3}{4} \left(\frac{Pr}{4Ja} \right)^{0.18} \frac{\sqrt{v_1/\omega}}{L_c} \left[\frac{(X_c + L_c)^{4/3} - X_c^{4/3}}{(\sqrt{v_1/\omega})^{4/3}} \right]^{0.82} \quad (3.25).$$

Similarly, a Nusselt number based upon the condenser length is defined as:

$$\overline{Nu}_L = \frac{\bar{h}L_c}{k_1} = \frac{3}{4} \left(\frac{Pr}{4Ja} \right)^{0.18} \left[\frac{(X_c + L_c)^{4/3} - X_c^{4/3}}{(\sqrt{v_1/\omega})^{4/3}} \right]^{0.82} \quad (3.26).$$

This result is valid over the wavy laminar regime of $30 < Re < 1000-1800$. The radial rotating thermosyphon is not expected to operate with a turbulent film so that regime will not be considered here. For turbulent films, the reader is referred to the works of El-Masri [3.4], Mudawar [3.5], Dakin [3.6] and [3.7].

3.2 Film Evaporation

Film evaporation is treated in a manner similar to film condensation. However, the film thickness is not zero at $x = 0$. If the adiabatic section is assumed to have no heat or mass transfer, then the condenser exit film Reynolds number will equal the evaporator entrance Reynolds number. Because the liquid film is evaporating, the energy balance on the film element shown in Figure 3-3 results in an equation similar to equation (3.12):

$$\frac{dx}{\sqrt{v_1/\omega}} = -\frac{Pr}{4Ja} \frac{dRe}{Nu} \quad (3.27).$$

Equation (3.18) is still valid here. It is substituted into (3.27) and integrated from $x = 0$ to $x = L_e$ and $Re = Re_{Le}$ to $Re = Re_{Le}$ yielding:

$$\text{Re}_{Le} = \frac{4}{3} \cdot \left[\left(\frac{3}{4} \text{Re}_{Lc} \right)^{4/3} - \frac{3\text{Ja}}{\text{Pr}} \cdot \frac{(\text{X}_e + \text{L}_e)^{4/3} - \text{X}_e^{4/3}}{\left(\sqrt{\text{v}_l/\omega} \right)^{4/3}} \right]^{3/4} \quad (3.28)$$

The average Nusselt number is then found from equation (3.13):

$$\overline{\text{Nu}} = \frac{\sqrt{\text{v}_l/\omega}}{\text{L}_e} \left(\frac{\text{Pr}}{3\text{Ja}} \right) \left[\left(\frac{3}{4} \text{Re}_{Lc} \right)^{4/3} - \frac{3\text{Ja}}{\text{Pr}} \cdot \frac{(\text{X}_e + \text{L}_e)^{4/3} - \text{X}_e^{4/3}}{\left(\sqrt{\text{v}_l/\omega} \right)^{4/3}} \right]^{3/4} \quad (3.29).$$

Just as in the condenser, another Nusselt number based on the evaporator length is defined as:

$$\overline{\text{Nu}}_{Le} = \frac{\bar{h}\text{L}_e}{k_l} = \left(\frac{\text{Pr}}{3\text{Ja}} \right) \left[\left(\frac{3}{4} \text{Re}_{Lc} \right)^{4/3} - \frac{3\text{Ja}}{\text{Pr}} \cdot \frac{(\text{X}_e + \text{L}_e)^{4/3} - \text{X}_e^{4/3}}{\left(\sqrt{\text{v}_l/\omega} \right)^{4/3}} \right]^{3/4} \quad (3.30)$$

Equation (3.30) is used to predict the heat transfer from the film above the liquid pool in the laminar regime. For the wavy laminar regime, equation (3.23) represents the local Nusselt number vice equation (3.18). When this is integrated along the evaporator length the exit Reynolds number becomes:

$$\text{Re}_{Le} = \left[\text{Re}_{Lc}^{1.22} - \frac{3\text{Ja}}{\text{Pr}} \cdot \frac{(\text{X}_e + \text{L}_e)^{4/3} - \text{X}_e^{4/3}}{\left(\sqrt{\text{v}_l/\omega} \right)^{4/3}} \right]^{0.82} \quad (3.31).$$

Similarly, the average Nusselt number is:

$$\overline{\text{Nu}} = \frac{\sqrt{\text{v}_l/\omega}}{\text{L}_e} \frac{\text{Pr}}{4\text{Ja}} \left[\text{Re}_{Lc}^{1.22} - \frac{3\text{Ja}}{\text{Pr}} \cdot \frac{(\text{X}_e + \text{L}_e)^{4/3} - \text{X}_e^{4/3}}{\left(\sqrt{\text{v}_l/\omega} \right)^{4/3}} \right]^{0.82} \quad (3.32)$$

for the wavy laminar regime. The Nusselt number based on the evaporator length is:

$$\overline{\text{Nu}}_{L_e} = \frac{\bar{h}L_e}{k_1} = \frac{\text{Pr}}{4\text{Ja}} \left[\text{Re}_{L_e}^{1.22} - \frac{3\text{Ja}}{\text{Pr}} \cdot \frac{(X_e + L_e)^{4/3} - X_e^{4/3}}{(\sqrt{v_1/\omega})^{4/3}} \right]^{0.82} \quad (3.33).$$

3.3 Nusselt Analysis Restrictions

As stated at the beginning of this chapter, there are many assumptions built into the Nusselt analysis of Section 3.2. The conservation equations for a falling film in a rotational gravity field are now examined more closely. This is to determine when the analysis of Section 3.2 may be expected to accurately predict the heat transfer capability of the radial rotating thermosyphon.

Figure 3-4 shows a thin film in a rotational gravitational field. A mass balance on the element in that figure gives the following continuity equation:

$$\frac{\partial u}{\partial x} + \frac{\partial v}{\partial y} = 0 \quad (3.34).$$

A momentum balance on the same film element taking into account both the $\omega^2 r$ and the Coriolis-hydrostatic forces yields the following momentum equation:

$$u \frac{\partial u}{\partial x} + v \frac{\partial u}{\partial y} = \nu_1 \frac{\partial^2 u}{\partial y^2} + \frac{(\rho_l - \rho_v)}{\rho_l} \cdot r\omega^2 - 2\omega y \frac{\partial u}{\partial x} \quad (3.35).$$

An energy balance on the same element gives the energy equation as:

$$u \frac{\partial T}{\partial x} + v \frac{\partial T}{\partial y} = \alpha_1 \frac{\partial^2 T}{\partial y^2} \quad (3.36).$$

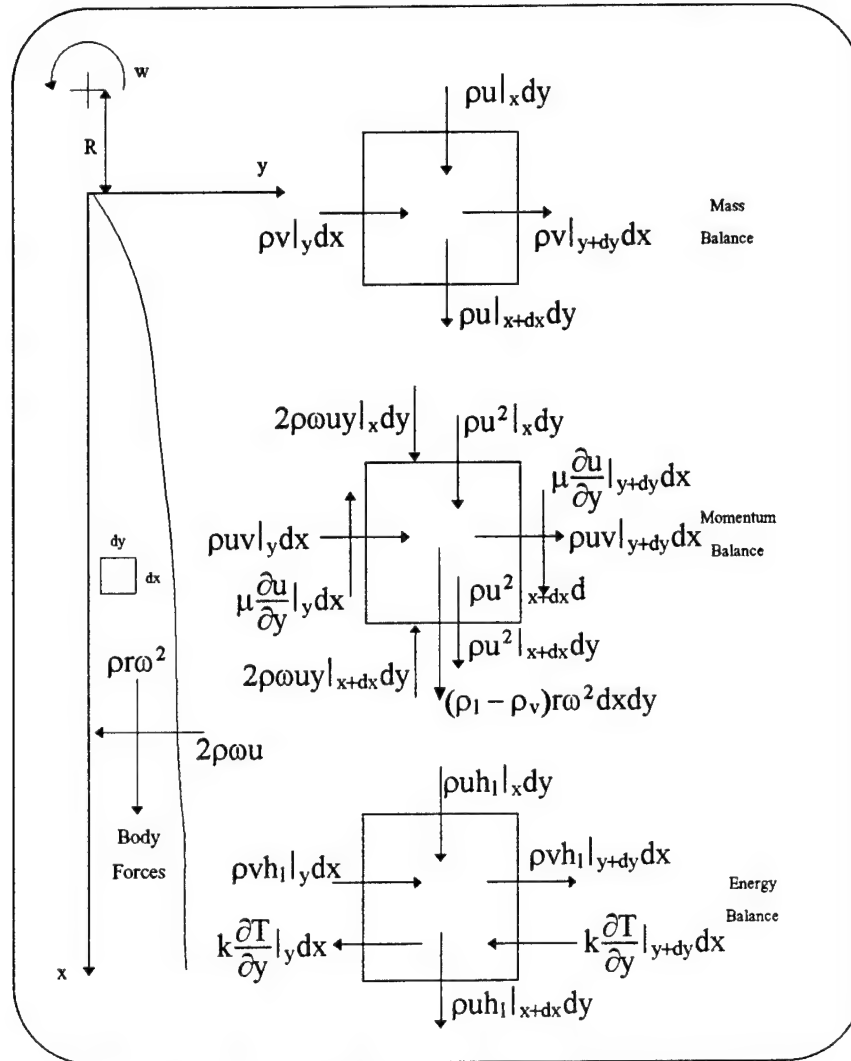


Figure 3-4: Film in Rotating Gravity Field

These equations are nondimensionalized by defining the following nondimensional variables:

$$u^* = \frac{u}{u_c}; \quad v^* = \frac{v}{v_c}; \quad x^* = \frac{x}{L_c}; \quad y^* = \frac{y}{\sqrt{v_l/\omega}}; \quad \Theta = \frac{T - T_w}{T_{sat} - T_w}; \quad \omega^* = \frac{\omega}{\Omega_{max}}; \quad r^* = \frac{r}{R_o};$$

where the x-direction characteristic velocity is chosen to be the average film velocity:

$$u_c \equiv \bar{u} = \frac{\Gamma}{\rho_l \delta}.$$

The y-direction characteristic velocity (v_c) is the one unknown left to be determined. The continuity equation (3.34) is used to define v_c :

$$\frac{u_c}{L_c} \frac{\partial u^*}{\partial x^*} + \frac{v_c}{\sqrt{v_1/\omega}} \frac{\partial v^*}{\partial y^*} = 0 \Rightarrow v_c \equiv u_c \frac{\sqrt{v_1/\omega}}{L_c} \quad (3.37).$$

The momentum and energy equations can now be nondimensionalized as:

$$\frac{Re}{4} Ek_L^{1/2} \left(u^* \frac{\partial u^*}{\partial x^*} + v^* \frac{\partial u^*}{\partial y^*} \right) = \frac{\partial^2 u^*}{\partial y^{*2}} + \frac{4 Ar_L Ek_L^{3/2}}{Re} r^* \omega^{*2} - 2 \cdot Ek_L^{1/2} \omega^* y^* \frac{\partial u^*}{\partial x^*} \quad (3.38)$$

$$\frac{Re}{4} Ek_L^{1/2} \left(u^* \frac{\partial \Theta}{\partial x^*} + v^* \frac{\partial \Theta}{\partial y^*} \right) = \frac{1}{Pr_1} \frac{\partial^2 \Theta}{\partial y^{*2}} \quad (3.39)$$

where the following non-dimensional groups have been defined:

$$\text{Film Reynolds No.} = Re \equiv \frac{4\Gamma}{\mu_1} = \frac{\text{Inertia Force}}{\text{Viscous Force}}$$

$$\text{Archimedes No.} = Ar_L \equiv \frac{R_o \Omega^2 L^3 (\rho_l - \rho_v)}{v_1^2 \rho_l} = \frac{\text{Buoyant Force}}{\text{Viscous Force}}$$

$$\text{Ekman No.} = Ek_L \equiv \frac{v_1}{\Omega L^2} = \frac{\text{Viscous Force}}{\text{Coriolis Force}}$$

$$\text{Prandtl No.} = Pr \equiv \frac{C_p \mu_1}{k_1} = \frac{v_1}{\alpha_1} = \frac{\text{Momentum diffusivity}}{\text{Thermal diffusivity}}.$$

The order of magnitude for the above parameters is:

$$10^1 < Re < 10^2$$

$$10^{11} < Ar_L < 10^{13}$$

$$10^0 < Pr_1 < 10^1$$

$$10^{-7} < Ek_L < 10^{-8}.$$

Within this range of parameters, the viscous term and the gravity term in equation (3.38) have an order of magnitude of about one. The convective terms have an order of magnitude of 10^{-2} or less and can be neglected without significant error. The Coriolis term in equation (3.38) can also be neglected as it has an order of magnitude of $10^{-4} - 10^{-3}$.

In the energy equation (3.39), the Reynolds-Prantl number product must be small compared to 10^4 for the Nusselt assumptions to be valid. This condition is met for the fluids and operating conditions under consideration. Recall that the operating conditions which generate higher Prantl numbers are at low heat fluxes where the Reynolds number is at the smaller end of its range.

At higher Reynolds numbers the Nusselt assumptions are no longer valid and the previous analysis can not be used. However, the gravitational term becomes smaller with respect to the other terms as the Reynolds number is increased. If this term can be neglected from the momentum equation then equations (3.38) and (3.39) resemble the flat plate boundary layer problem which is treated in many introductory heat transfer texts. Previous researchers [3.8] have applied the integral method for solving the classical boundary layer problem to gravitational thermosyphons.

3.4 Pool Boiling

Any portion of the liquid charge which is not in vapor form or forming part of the liquid film remains at the bottom of the evaporator forming the liquid pool. Heat transfer from the walls surrounding the pool is by natural convection at low heat fluxes and by pool boiling at high heat fluxes. Classical pool boiling can be described by the relation of Rohsenow [3.9]:

$$Nu' = \frac{hL_c}{k_l} = \frac{Ja^2}{C_{nb}^3 Pr^m}; \quad (3.40)$$

where $L_c = \left[\frac{\sigma}{(\rho_l - \rho_v)g} \right]^{1/2}$, C_{nb} and m are empirical constants that are a function of the liquid and surface characteristics. The relationship in Equation (3.40) cannot be used directly because the characteristic length is a function of gravity which varies with radius. Equation (3.36) can be modified by introducing a new characteristic length which is the same as that used in the condensation and evaporation Nusselt numbers above. The modified Nusselt number is:

$$Nu = \frac{\sqrt{v_l/\omega}}{L_c} \cdot Nu' = \frac{\sqrt{v_l/\omega} Ja^2}{C_{nb}^3 Pr^m} \left(\frac{(\rho_l - \rho_v)g(x)}{\sigma} \right)^{1/2} \quad (3.41)$$

which is now a function of pool depth. The average Nusselt number is found from:

$$\overline{Nu} = \frac{\sqrt{v_l/\omega} Ja^2}{C_{nb}^3 Pr^m} \left(\frac{\rho_l - \rho_v}{\sigma} \right)^{1/2} \cdot \frac{\omega}{L_p} \int_0^{L_p} (X_p + x)^{1/2} \cdot dx \quad (3.42)$$

which is:

$$\overline{Nu} = \frac{2}{3} \frac{\sqrt{v_l/\omega} Ja^2}{C_{nb}^3 Pr^m} \left(\frac{\rho_l - \rho_v}{\sigma} \right)^{1/2} \cdot \omega \cdot \left[\frac{(X_p + L_p)^{3/2} - X_p^{3/2}}{L_p} \right] \quad (3.43).$$

Equation (3.39) accounts for the effect of the variable gravity field in the liquid pool. A

Nusselt number based on the evaporator length can be defined as:

$$\boxed{\overline{Nu}_{Le} = \frac{2}{3} \frac{L_e Ja^2}{C_{nb}^3 Pr^m} \left(\frac{\rho_l - \rho_v}{\sigma} \right)^{1/2} \cdot \omega \cdot \left[\frac{(X_p + L_p)^{3/2} - X_p^{3/2}}{L_p} \right]} \quad (3.44).$$

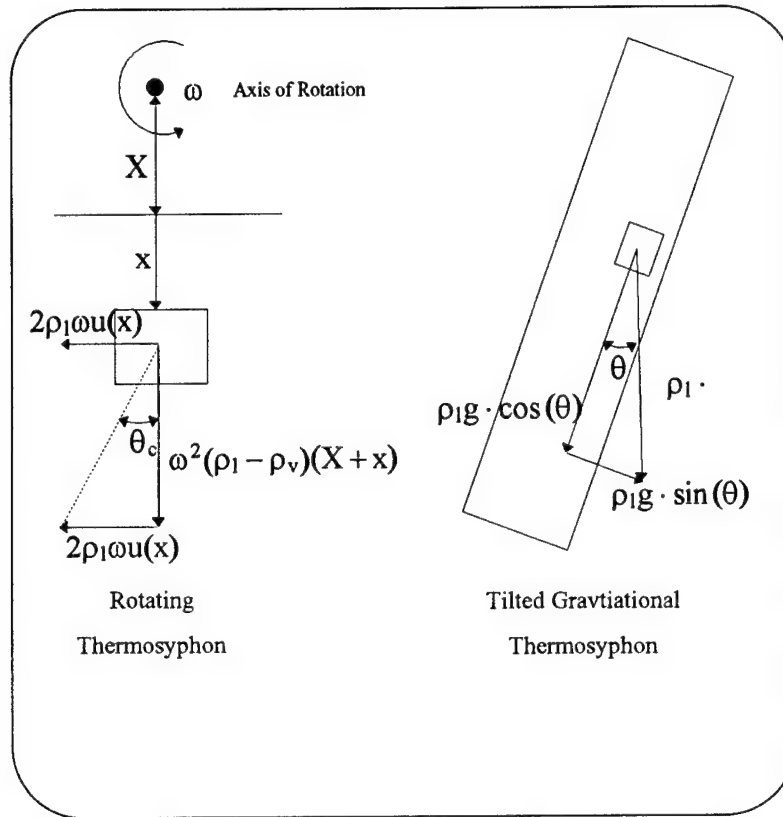


Figure 3-5: Body Force Components in Thermosyphons

3.5 Coriolis Effects

The Coriolis force occurs in any rotating system when the mass under consideration moves in the radial direction. A complete treatment of Coriolis acceleration can be found in [3.10]. In the case of the RRT the working fluid flows radially as the pipe is spun around, resulting in a Coriolis force as shown in Figure 3-5. The body forces of a tilted gravitational thermosyphon are also depicted in Figure 3-5. Lock [3.11], suggests a comparison of these forces as a method for accounting for the Coriolis force in the RRT.

In the tilted gravitational thermosyphon the gravity force components on the liquid film are given by:

$$g_a = \rho_l \cdot g \cdot \cos(\theta) \text{ - gravity component parallel to thermosyphon axis}$$

$$g_t = \rho_l \cdot g \cdot \sin(\theta) \text{ - gravity component perpendicular to thermosyphon axis.}$$

where θ is the angle between the thermosyphon axis and vertical. In the radial rotating thermosyphon the body force components are:

$$\begin{aligned} g_a(x) &= (\rho_l - \rho_g)\omega^2(X+x) - \text{centrifugal force} \\ g_t(x) &= 2 \cdot \rho_l \cdot \omega \cdot u(x) - \text{Coriolis force.} \end{aligned}$$

An effective tilt angle for the rotating thermosyphon can be defined as:

$$\tan(\theta_c) = \frac{2\rho_l\omega u(x)}{(\rho_l - \rho_g)\omega^2(X+x)} \quad (3.45).$$

where $u(x)$ is the fluid velocity in the radial direction. Lock determines characteristic velocity scales from the equation of motion neglecting the convective terms. The resulting Coriolis tilt angle from his analysis is:

$$\theta_c = (2\pi)^{1/3} \left(\frac{D}{r(x)} \frac{Ja}{Pr} \frac{\rho_l}{(\rho_l - \rho_v)} \right)^{1/3} \quad (3.46)$$

where small angles have been assumed.

Lock further postulates that the Coriolis effects can be treated by looking at tilted gravitational thermosyphons. There have been several investigations of tilted gravitational thermosyphons [3.8], [3.12], [3.4] and [3.13], all of which show an increase in heat transfer ability with tilt angle up to a maximum that occurs in the range of 40-60 degrees from vertical. This increase is due to the thinning of the film layer by the gravity component normal to the thermosyphon axis. The film is thickened at the "bottom" of the circumference, but studies have shown this area to be very small in comparison to the thinned area; hence the resultant increase in overall heat transfer coefficient. For the conditions encountered in the RRT for axial motors, the Coriolis tilt will only be on the

order of one or two degrees using this method. This is consistent with the small size of the Coriolis term in equation (3.38). Such a small tilt angle will not have a significant impact on the heat transfer capability of the RRT. The asymmetry which it causes may help promote dryout failure on the leading edge of the evaporator.

3.6 Performance Limits

Dunn & Reay [3.14] provide a fairly complete accounting of performance limits for heat pipes. The performance limits of the radial rotating thermosyphon are similar to those of the heat pipe when the geometry differences and effects of rotation are accounted for. This section describes each type of limit and suggests a possible method of determining the limits for radial rotating thermosyphons.

3.6.1 Viscous Limit

The viscous limit of a thermosyphon occurs at low temperatures when the viscous drag dominates the vapor flow in the thermosyphon. This limit is directly proportional to the vapor pressure and density in the evaporator. A two-dimensional analysis of the vapor flow in the pipe yields the following result:

$$q = \frac{r_v^2 h_{fg} \rho_v p_v}{16 \mu_v L_{eff}} \quad (3.47)$$

which agrees well with published data for heat pipes [3.11]. This limit is normally only encountered under conditions of very low vapor pressure and is not reached under the operating conditions being considered.

3.6.2 Sonic Limit

The vapor flow in a heat pipe or thermosyphon behaves much like the flow through a converging-diverging nozzle. The difference being that in the nozzle the mass flow is constant while the cross-sectional area varies; in the thermosyphon the area is constant while the mass flow rate varies. The evaporator exit is the point where the greatest vapor mass flow exists. This location corresponds to the throat of a nozzle. The sonic limit occurs when the vapor velocity at the exit of the evaporator reaches the speed of sound at that point. This choking limitation can be predicted by:

$$q = 0.474 h_{fg} \sqrt{\rho_v p_v} \quad (3.48)$$

which is cited in [3.11].

3.6.3 Entrainment Limit

Entrainment is caused by the interfacial shear stress between the liquid film on the walls and the vapor core. The entrainment limit is often the limiting factor in low temperature thermosyphons such as are the subject of this research. Unfortunately, there seems to be no concise method for calculating this limit. Dunn & Reay [3.11] present the following correlation for thermosyphons:

$$q = h_{fg} f_1 f_2 f_3 \sqrt{\rho_v} [g(\rho_l - \rho_v) \sigma_l]^{0.25} \quad (3.49)$$

where $f_1 - f_3$ are empirical constants which are functions of Bond Number, pressure coefficient and inclination angle, respectively. This relationship is used to predict entrainment failure in rotating thermosyphons.

3.6.4 Burnout Limit

The burnout limit is encountered at high radial heat fluxes. Although this limit could be encountered in thermosyphons, it is primarily a problem in heat pipes when boiling within the wick structure upsets the capillary pumping action. In the RRT, this limit manifests itself in two distinct ways. One is the boiling crisis situation (or transition to film boiling) in the liquid pool at the end of the evaporator. The other is the critical heat flux limit in the liquid film above the pool.

The geometry of the pool within the RRT is markedly different from that of classic pool boiling. Previous researchers [3.15] and [3.16] have shown that the shape of the pool boiling curve is preserved, but the critical heat flux is altered. Work with axial rotating heat pipes [3.17] has also shown that the centrifugal force can affect the critical heat flux. The critical heat flux can be calculated using the method of Lienhard and Dhir [3.5] for finite bodies. For the geometry of the RRT the critical heat flux is given by:

$$q_{\max} = 0.90 \cdot q_{\max f} = 0.90 \cdot \frac{\pi}{24} \rho_v^{1/2} h_{fg} [\sigma g(x)(\rho_l - \rho_v)]^{1/4} \quad (3.50)$$

where $q_{\max f}$ is the flat plate pool boiling limit. By substituting in the centrifugal acceleration ($g(x) = r\omega^2$) for the gravitational acceleration (g), q_{\max} has become a function of pool depth.

Recalling that $r = X_p + x$ in the liquid pool, equation (3.50) can be integrated to obtain an average evaporator critical heat flux. The result is:

$$q_{\max} = 0.90 \cdot \frac{\pi}{24} \frac{4}{5} \rho_v^{1/2} h_{fg} [\sigma \omega^2 (\rho_l - \rho_v)]^{1/4} \left[(X_p + L_p)^{5/4} - X_p^{5/4} \right] \quad (3.51)$$

which accounts for the differences in both geometry and body force. Unlike most other limits on the RRT, the critical boiling heat flux is a radial flux value which acts over the

entire heated surface area of the liquid pool rather than the cross-sectional area. As a result, other performance limits will be encountered well prior to the burnout limit of equation (3.51).

The second type of burnout limitation takes place in the liquid film above the pool. Mudawar [3.5] studied evaporation and boiling of rotating liquid films in the field of gas turbine cooling. The critical heat flux in the liquid film occurs when the film boils away and can no longer re-wet the surface creating a dry wall condition. Based upon an analysis which balances vapor drag and body forces, Mudawar determined the critical heat flux in the liquid film to be:

$$q = 0.69 \cdot \rho_v h_{fg} \left[\frac{(\rho_l - \rho_v) \sigma \omega \sqrt[3]{v_l a}}{\rho_v^2} \right]^{1/4} \quad (3.52)$$

which he confirmed experimentally.

Another related phenomenon which is important to the radial rotating thermosyphon is the incipient boiling limit in the liquid film. This is the level of heat flux at which the liquid film begins to boil. This heat flux can be determined as:

$$q_i = \frac{h_{fg} k_l}{8 \sigma T_{sat} v_{fg}} (T_w - T_{sat})^2 \quad (3.53)$$

where v_{fg} is the difference in liquid and vapor specific volumes. Rohsenow [3.18] bases this result on the premise that when the wall temperature exceeds a certain value, wall-bound bubbles will begin to grow. Since most commercially prepared surfaces have a wide range of cavity sizes, the incipient boiling condition should be independent of surface condition.

Mudawar [3.15], presents equation (3.53) in a slightly different form:

$$q_i = \frac{8\sigma T_{\text{sat}} V_{\text{fg}} h^2}{h_{\text{fg}} k_l} \quad (3.54)$$

where the heat transfer coefficient, h is calculated from:

$$h = 0.042 \cdot \lambda \cdot \text{Re}^{0.17} \cdot \text{Pr}^{0.35} \quad (3.55)$$

$$\text{and } \lambda = \text{Pr}^{-0.48} \text{Re}^{[0.18(\text{Pr}-0.3)^{0.18}-0.17]} \quad (3.56)$$

The heat transfer coefficient in equation (3.55) is his theoretical result for turbulent films which is valid for $5 \times 10^3 < \text{Re} < 80 \times 10^3$. For the conditions to be encountered in the present research, equation (3.54) can be used in conjunction with equations (3.29) and (3.32) to predict the incipient boiling condition.

3.6.5 Dry-Out Limit

A limit peculiar to thermosyphons is the dry-out limit. Dry-out occurs when the liquid film evaporates entirely prior to reaching the liquid pool at the bottom of the evaporator. It is caused by small fill ratios and long evaporator sections where the total heat transfer ability of the evaporator exceeds that of the condenser section. Dry-out can be predicted by comparing the instantaneous mass flow rates of the condenser and evaporator sections. When the mass flow rate of the evaporator exceeds that of the condenser, dry-out is imminent.

3.6.6 Flooding Limit

Flooding or hold up is specific to thermosyphons. It is another result of the shear stress at the liquid/vapor interface. Flooding occurs when the vapor velocity increases to a point where the vapor drag on the liquid film overcomes the gravitational force, halting the downward flow of the film. Flooding differs from entrainment in that the film is not carried off in the vapor stream but is simply held stationary on the tube wall. This phenomenon is also common in two-phase vertical flow. Wallis [3.19] suggests the following relationship for predicting the heat flow at which hold-up will occur:

$$Q_{\max} = C_w^2 \frac{\pi D_i^{2.5}}{4} \cdot \frac{h_{fg} \sqrt{g \rho_v (\rho_l - \rho_v)}}{\left[1 + (\rho_v / \rho_l)^{1/4} \right]^2} \quad (3.57).$$

When SI units are used, the empirical constant, $C_w = 1.105$. Nguyen-Chi and Groll [3.20] achieved good results with this correlation on their tilted gravitational thermosyphons. Equation (3.57) is used to predict flooding failure in rotating thermosyphons with g replaced by the effective gravity due to the centrifugal force.

3.7 External Heat Transfer

Thus far, this chapter has dealt with the heat transfer processes within the thermosyphon. The thermosyphon must form part of a total cooling system to be of any practical use. This section examines how heat is transferred into the evaporator and out of the condenser of the thermosyphon.

Heat is generated in the rotor both within the windings and in the magnetic iron. A two-dimensional finite element model of the rotor slot region was developed to determine the temperature distribution in the region of the rotor windings and thermosyphon

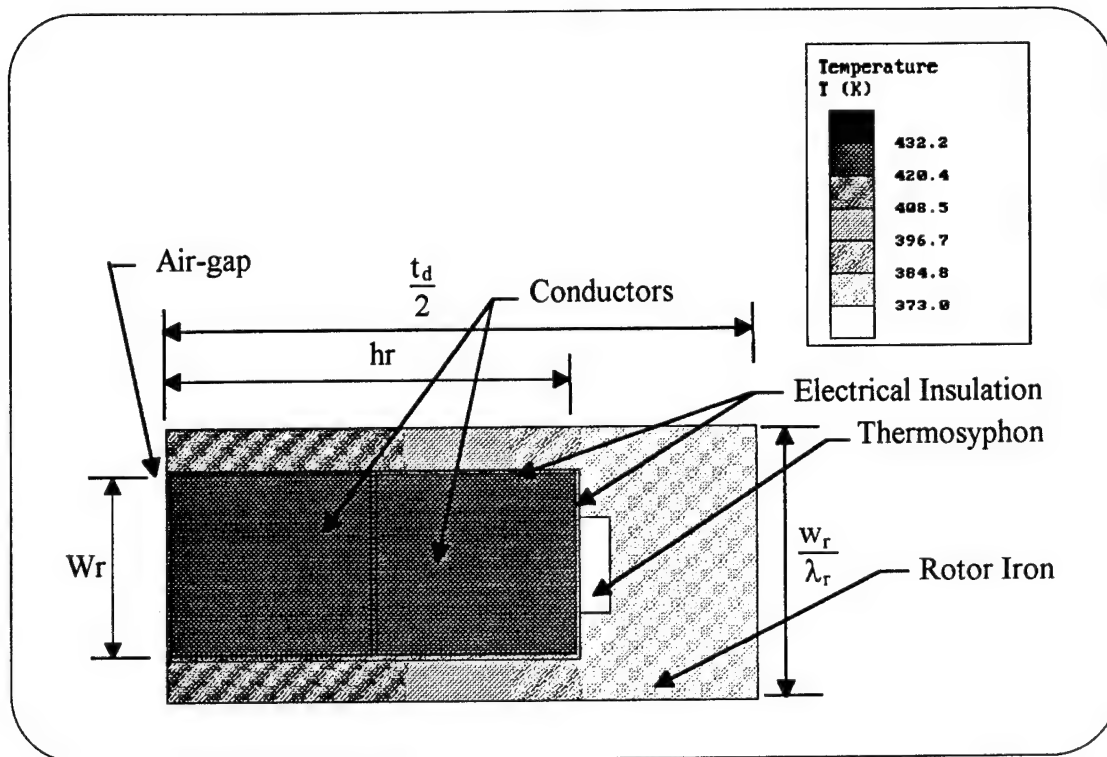


Figure 3-6: Rotor Slot Detail for Finite Element Solution

evaporators. The geometry under consideration is depicted in Figure 3-6. This geometry simulates the rotor slot and surrounding iron at the inner radius of the rotor. The specific dimensions chosen are from the sample motor depicted in Figures 5-1 and 5-2.

The temperature profile of Figure 3-6 indicates that the largest temperature drop occurs across the electrical insulation, all other temperature drops are small by comparison. This specific geometry results in a maximum winding temperature of 159° C when the wall temperature of the thermosyphon is assumed to be 100° C.

At the opposite (condenser) end of the thermosyphon the heat is dissipated to a secondary cooling fluid. This secondary coolant may be air or water. Air provides for a simpler design, but more heat can be extracted with water than air. To determine if air can

be used to cool the thermosyphons the external heat transfer coefficient is calculated based on the classical flow through a tube bundle problem.

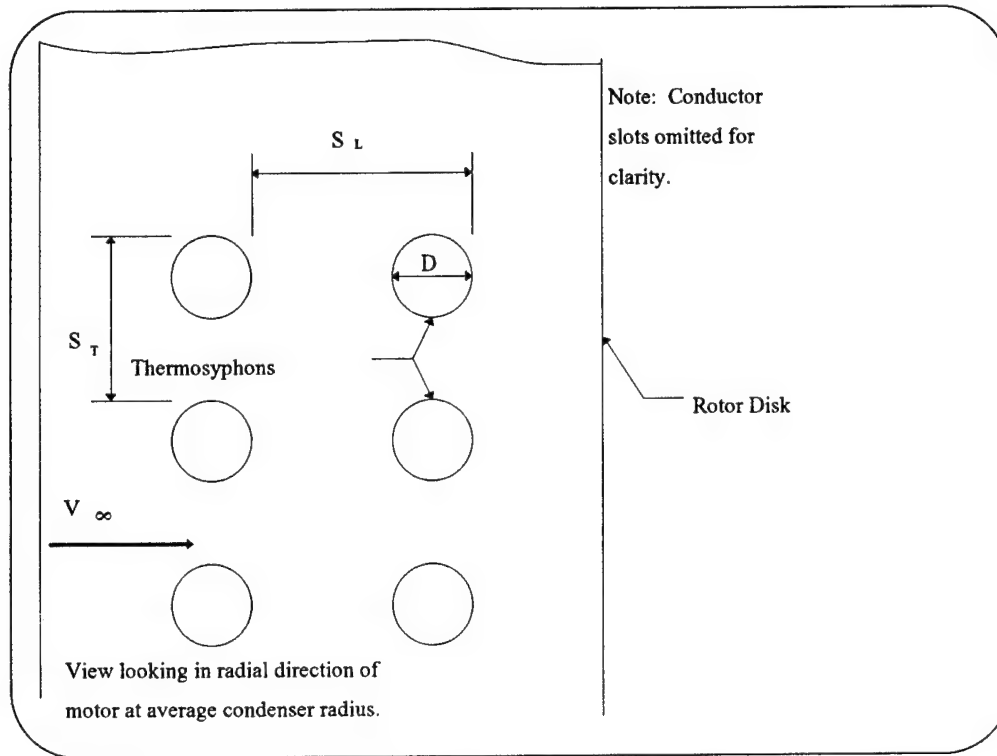


Figure 3-7: Condenser Section External Arrangement

Figure 3-7 shows the geometry under consideration. The RRT's are assumed to have round cross-sections. The transverse spacing is taken as the average over the length of the condenser since it varies over the condenser length. The transverse and longitudinal pitch are calculated as:

$$P_T = \frac{S_T}{D}; \quad P_L = \frac{S_L}{D} \quad (3.58)$$

The Nusselt number for the array of tubes is simply:

$$\overline{Nu}_D = \frac{1 + (N-1)\Phi}{N} \overline{Nu}_D^1 \quad (3.59)$$

where N is the number of tubes (thermosyphons) \overline{Nu}_D^1 is the Nusselt number for a single tube and Φ is:

$$\Phi_{aligned} = 1 + \frac{0.7}{\Psi^{1.5}} \frac{S_L/S_T - 0.3}{(S_L/S_T + 0.7)^2} \quad (3.60)$$

where:

$$\Psi = 1 - \frac{\pi}{4P_T}; P_L > 1 \text{ and } \Psi = 1 - \frac{\pi}{4P_T P_L}; P_L < 1.$$

The single tube Nusselt number is given by:

$$\overline{Nu}_D^1 = 0.3 + \frac{0.62 \cdot Re_D^{1/2} Pr^{1/3}}{\left[1 + (0.4/Pr)^{2/3}\right]^{1/4}}; Re_D < 10^4$$

$$\overline{Nu}_D^1 = 0.3 + \frac{0.62 \cdot Re_D^{1/2} Pr^{1/3}}{\left[1 + (0.4/Pr)^{2/3}\right]^{1/4}} \left[1 + \left(\frac{Re_D}{282,000}\right)^{1/2}\right]; 2 \times 10^4 < Re_D < 4 \times 10^5$$

$$\overline{Nu}_D^1 = 0.3 + \frac{0.62 \cdot Re_D^{1/2} Pr^{1/3}}{\left[1 + (0.4/Pr)^{2/3}\right]^{1/4}} \left[1 + \left(\frac{Re_D}{282,000}\right)^{5/8}\right]^{4/5}; 4 \times 10^5 < Re_D < 5 \times 10^6.$$

The Reynolds number is based on the tube diameter:

$$Re_D = \frac{\overline{V}D}{\nu}$$

where the velocity is the maximum between the tubes:

$$\overline{V} = \overline{V}_\infty \frac{S_T}{S_T - \frac{\pi D}{4}}.$$

The above set of equations is used to calculate the maximum heat which can be transferred from the condenser to the air flowing through the motor without cooling fins.

In most cases this heat transfer will be insufficient to completely cool the condenser. There are two possible solutions to this problem: 1) switch to water cooling of the condensers, and 2) add fins to the exterior of the condensers. If solution 1 is chosen, then the above analysis still holds with water properties substituted for air in the equations. If solution 2 is chosen, then the problem is solved in a different manner.

Figure 3-8 depicts the geometry of the condensers with cooling fins attached.

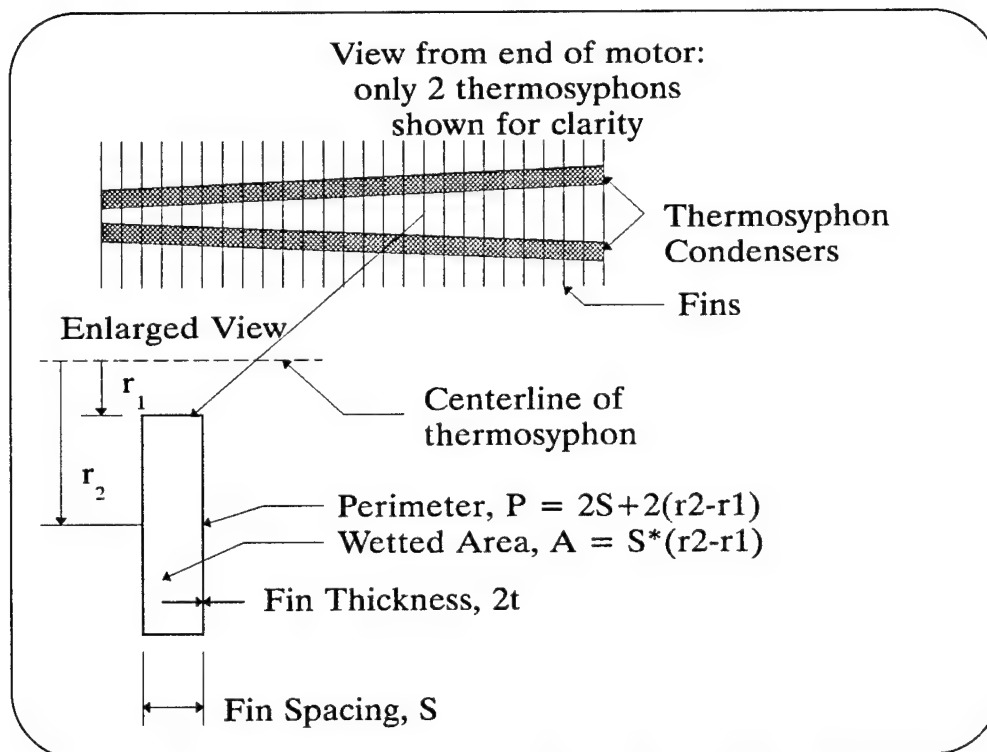


Figure 3-8: Finned Condenser Arrangement

Heat transfer from the finned surface is determined from the fin efficiency. For design purposes, the fins are assumed to be circular with an outer radius equal to half the distance between condenser tubes. The fin efficiency for such an arrangement is:

$$\eta_f = \frac{2r_1/\beta}{(r_2^2 - r_1^2)} \left[\frac{K_1(\beta \cdot r_1) \cdot I_1(\beta \cdot r_2) - I_1(\beta \cdot r_1) \cdot K_1(\beta \cdot r_2)}{K_0(\beta \cdot r_1) \cdot I_1(\beta \cdot r_2) + I_0(\beta \cdot r_1) \cdot K_1(\beta \cdot r_2)} \right] \quad (3.61)$$

where I and K are Bessel functions, r_1 and r_2 are the inner and outer radii of the fin and β is given by:

$$\beta = \sqrt{\frac{h_c}{k \cdot t}}$$

k is the thermal conductivity of the fin material and t is the half-thickness of the fin. The heat transfer coefficient from the fins is determined from:

$$Nu_{Dh} = \frac{h_c D_h}{k} = \frac{(f/8)(Re_{Dh} - 1000)Pr}{1 + 12.7(f/8)^{1/2}(Pr^{2/3} - 1)} \quad (3.62)$$

where f is determined by:

$$f = (0.79 \ln(Re_{Dh}) - 1.64)^{-2}$$

and the Reynolds number is:

$$Re_{Dh} = \frac{VD_h}{\nu}$$

where the hydraulic diameter (D_h) is found from:

$$D_h = \frac{4 \cdot A}{P}$$

A is the flow area and P is the wetted perimeter as shown in Figure 3-8. The total heat transfer from the finned surface is:

$$Q = h_c A_f (T_b - T_\infty) \cdot \eta_f \quad (3.63)$$

where A_f is the surface area of the finned surface. This result is compared to the required heat flow per thermosyphon to determine if the finned condenser can be air-cooled. This completes the heat transfer circuit from the windings to the secondary coolant. For design purposes, the secondary coolant is assumed to have an entry temperature of 30 °C. The maximum allowable winding temperature is 150 °C.

- 3.1 Mills, A.F., *Heat Transfer*, Irwin, Homewood, IL, 1992.
- 3.2 Dhir, V. & Lienhard, J., "Laminar Film Condensation on Plane and Axisymmetric Bodies in Nonuniform Gravity," *Journal of Heat Transfer*, Vol. 93, pp. 97-100, Feb. 1971.
- 3.3 Chun, K.R. & Seban, R.A., "Heat Transfer to Evaporating Liquid Films," *Journal of Heat Transfer*, Vol. 93, pp. 391-396, 1971.
- 3.4 El-Masri, M.A., *Fluid Mechanics and Heat Transfer in the Blade Channels of a Water-Cooled Gas Turbine*, Ph.D. Thesis, M.I.T., 1979.
- 3.5 Mudawwar, I.A., *Boiling Heat Transfer in Rotating Channels with Reference to Gas Turbine Blade Cooling*, Ph.D. Thesis, M.I.T., 1984.
- 3.6 Dakin, J.T. & So, R.M.C., "The Dynamics of Thin Liquid Films in Rotating Tubes: Approximate Analysis," *Journal of Fluids Engineering*, Vol. 100, pp. 187-193, June 1978.
- 3.7 Dakin, J.T. et al., "Heat Transfer in the Rotating Blades of a Water-cooled Gas Turbine," *Gas Turbine Heat Transfer 1978*, pp. 39-47, ASME, New York, NY, 1978.
- 3.8 Al-Farah M. et al., "Analysis of Film Condensation in Tilted Thermosyphons," *ASME Paper No. 91-HT-21*, 1991.
- 3.9 Rohsenow, W.M., "A method of Correlating Heat Transfer Data for Surface Boiling of Liquids," *Trans. ASME*, Vol. 74, pp. 969-976, 1952.
- 3.10 Halliday, D. & Resnick, R., *Physics*, John Wiley & Sons, 1978.
- 3.11 Lock, G.S.H., *The Tubular Thermosyphon*, Oxford University Press, New York, NY, 1992.
- 3.12 Hahne, E. & Gross, U., "The Influence of Tilt Angle on a Closed Two-Phase Thermosyphon," *4th International Heat Pipe Conference*, pp. 125-136, 1981.
- 3.13 Negishi, K. & Sawada, T., "Heat Transfer Performance of an Inclined Two-Phase Thermosyphon," *International Journal of Heat and Mass Transfer*, Vol. 26(2), pp. 1207-1213, 1983.
- 3.14 Dunn, P.D. & Reay, D.A., *Heat Pipes*, 4th ed, Pergamon Press, Tarrytown, NY, 1994.
- 3.15 Cohen, H. & Bayley, F., "Heat-transfer Problems of Liquid-cooled Gas-turbine Blades," *Proceedings, Institution of Mechanical Engineers*, Vol. 169, pp. 1063-1074, 1956.

- 3.16 Lienhard, J.H. & Dhir, V.K., "Hydrodynamic Prediction of Peak Pool-boiling Heat Fluxes from Finite Bodies," *Journal of Heat Transfer*, Vol. 95, pp. 152-158, May 1973.
- 3.17 Marto, P.J., "Rotating Heat Pipes," *Heat & Mass Transfer in Rotating Machinery*, Edited by: D.E. Metzger & N.H. Afgan, Hemisphere, Washington, DC, 1984.
- 3.18 Rohsenow, W.M., *Handbook of Heat Transfer Fundamentals*, Chapter 12: Boiling, McGraw-Hill, 1985.
- 3.19 Wallis, G.B., *One-dimensional Two-phase Flow*, McGraw-Hill, New York, NY, 1969.
- 3.20 Nguyen-Chi, H. & Groll, M., "Entrainment or Flooding Limit in a Closed Two-Phase Thermosyphon," *Advances in Heat Pipe Technology, Proceedings of the 4th International Heat Pipe Conference*, Pergamon, 1982.

Chapter 4: Experimental Setup

4.1 Experiment Design

The purpose of the experimental portion of this thesis is to determine if the theoretical results developed in Chapter 3 are accurate enough to be used for design purposes. With this objective in mind, the operating conditions and parameters are developed to specifically simulate the operating conditions that are expected to be encountered in ship propulsion motors.

Due to size limitations of the laboratory facilities, a full scale experimental setup is impractical. Therefore, the experimental setup of a single RRT is designed to be a one-half scale model of the actual motor size. Similarity between the experiment and the actual motor is achieved by making the important non-dimensional parameters the same order of magnitude. Table 4-1 compares the important dimensions and non-dimensional parameters of the experimental setup and a typical destroyer size propulsion motor. Throughout this research the fill ratio is defined as the liquid fill volume divided by the evaporator volume. The length-to-diameter ratio is defined as the total thermosyphon length divided by the internal hydraulic diameter.

All testing is completed by maintaining a constant rotational speed and increasing the power input to a predetermined value. The tests are run until a failure occurs or until a predetermined internal pressure of 50 psig is reached. Once failure occurs, the thermosyphon is cooled completely prior to re-starting it at a different speed setting.

Parameter	Experiment	35,000 HP Motor
Outer Radius (m)	0.5	1
Inner Radius (m)	0.1	0.2
Condenser Length (m)	0.1	0.3
Evaporator Length (m)	0.13	0.4
Rotational Speed (rad/sec)	0 - 50	0 - 20
Film Reynolds No. = Re	$10^1 - 10^2$	$10^1 - 10^2$
Archimedes No. = Ar_L	$10^{11} - 10^{13}$	$10^{11} - 10^{13}$
Ekman No. = Ek_L	$10^{-8} - 10^{-7}$	$10^{-8} - 10^{-7}$
Prandtl No. = Pr	$10^0 - 10^1$	$10^0 - 10^1$
$\frac{\sqrt{\nu_l/\omega}}{L_c}$	10^{-4}	10^{-4}
$\frac{L}{D}$	30 - 62	50 - 70

Table 4-1: Experiment vs. Motor Parameters

4.2 Measurements and Calculations

In order to determine the heat transfer characteristics of the thermosyphon, the

following quantities are measured:

- Cooling water inlet and outlet temperatures, T_{in} & T_{out} [deg. C]
- Cooling water volume flow rate, Q_{H_2O} [$m^3/sec.$]
- Speed of rotation, Ω [rad./sec.]
- Thermosyphon vapor temperature, T_{sat} [deg. C]
- Thermosyphon condenser wall temperature, T_{cw} [deg. C]
- Thermosyphon evaporator wall temperature, T_{ew} [deg. C].

Additional measurements taken are:

- Heater input voltage, V [Volts]

- Heater input current, I [Amps]
- Thermosyphon pressure, P_{sat} [kPa].

From these measurements the condenser and evaporator heat transfer coefficients and overall heat transferred by the thermosyphon are determined. The overall heat transfer rate comes from an enthalpy balance of the cooling water:

$$Q = \dot{m} \cdot C_p \cdot (T_{out} - T_{in}) \quad [\text{Watts}] \quad (4.1)$$

where C_p is the specific heat of the cooling water. \dot{m} is the mass flow rate of the cooling water which is:

$$\dot{m} = \rho_{H_2O} \cdot \dot{Q}_{H_2O} \quad [\text{kg. / sec.}] \quad (4.2).$$

The cooling water volume flow rate is measured with a rotameter type flow meter.

Density is determined from the saturated liquid thermodynamic Table at the average cooling water temperature.

The heat transfer coefficients are calculated from the definition of a convective heat transfer coefficient:

$$Q \equiv \bar{h} \cdot A \cdot (\Delta T) \quad [\text{Watts}] \quad (4.3)$$

where Q is determined from equation (4.1) above, A is the measured heat transfer area and ΔT is the difference between the thermosyphon wall and the saturation temperatures.

This temperature difference is defined as:

$$\begin{aligned} \Delta T &= (T_{sat} - T_{cw}) \text{ in the condenser} \\ \Delta T &= (T_{ew} - T_{sat}) \text{ in the evaporator.} \end{aligned}$$

Each of the above temperatures is measured in more than one way to obtain the final value. T_{sat} is measured by two thermocouple probes. One probe is inserted into each

end of the test thermosyphon. These two measurements are averaged to obtain T_{sat} . The pressure transducer output is used to compute T_{sat} independently and this value is compared to that obtained from the thermocouples as a sanity check.

T_{cw} and T_{ew} are each computed from the average of five wall temperature measurements. See Figure 4-1 for actual thermocouple locations on the test thermosyphons. All of the wall temperature thermocouples are located on the trailing edge of the thermosyphon for all tests. This location results in temperature measurements taken at the location of the greatest film thickness. Appendix A contains more detailed information on construction of the test thermosyphons.

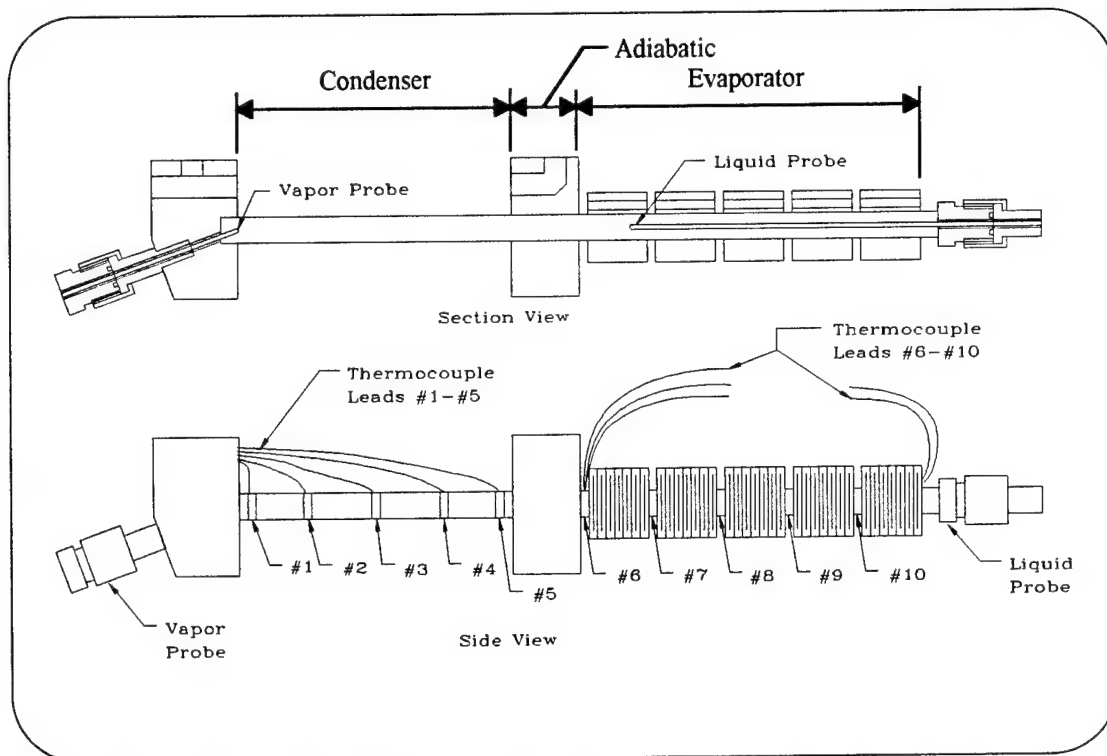


Figure 4-1: Test Thermosyphon

T_{out} and T_{in} are measured both in the fixed reference frame and on the rotor. Only the rotor measurements are used to calculate the heat transfer rate as they are more accurate than the stationary measurements. This is because the stationary measurement points are further from the test thermosyphon cooling jacket. The stationary measurements are used to set the cooling water flow rate since they are not subject to slip ring noise and can be read in real time. The flow rate is adjusted to maintain a cooling water temperature difference of approximately 10° C.

4.3 The Test Apparatus

A test stand was constructed to test thermosyphons in a rotating reference frame. The test stand is depicted in Figures 4-2 & 4-3. The main components of the test stand are the foundation, rotor, drive system, safety shield, cooling water system, heater and instrumentation. The important aspects of each will be described below.

The foundation supports the rotor and drive system. It is designed to allow a rotor radius of 0.5 meter in keeping with the scale of the experiment.

The rotor features rotating couplings on each end for the cooling water. There are also slip rings for power transfer to the heater and for connecting the rotating electronics assembly with the stationary one. A static balance of the rotor is sufficient as the rotational speed was limited to 500 rpm.

The drive system consists of a DC motor which drives the rotor assembly through a V-belt with a 2.4:1 speed reduction. A variable transformer feeding through a bridge rectifier is used to vary the terminal voltage to the motor, achieving a continuously variable rotor speed.

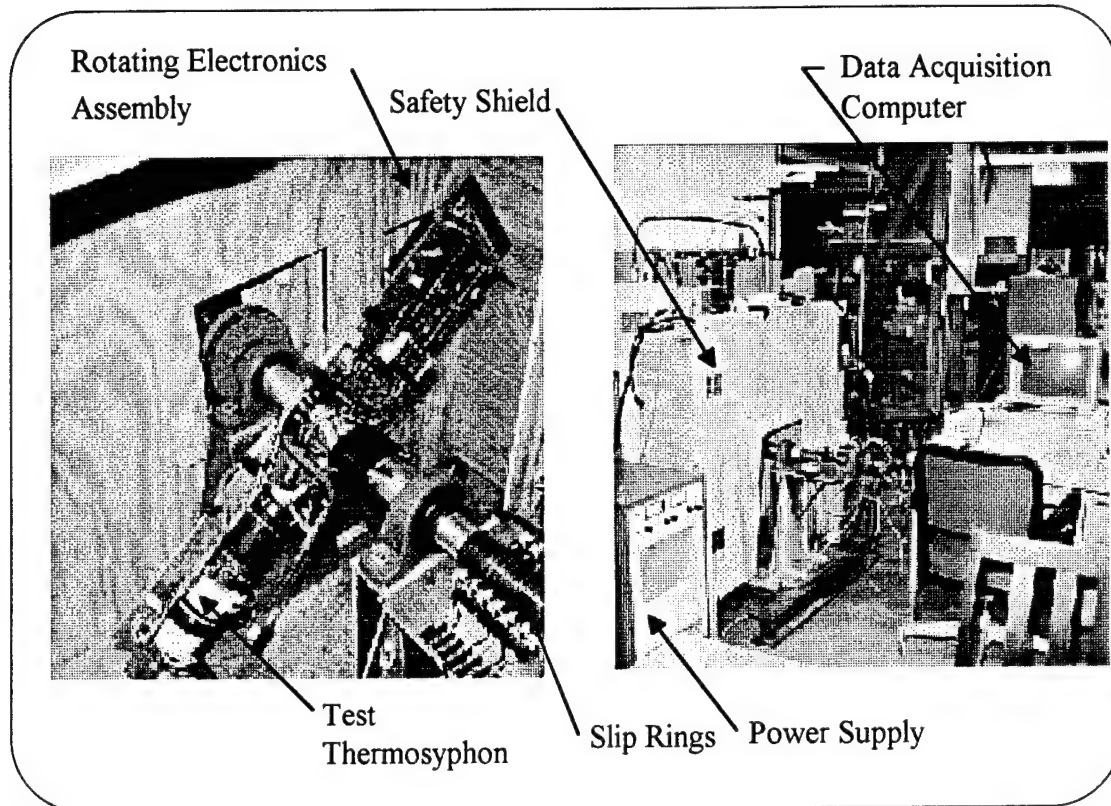


Figure 4-2: Thermosyphon Test Stand

The safety shield is shown in Figure 4-2. It is constructed of 1-1/2 inches of plywood with a 2"x4" frame surrounding the shield. The safety shield is sized to allow a rotor radius of 0.5 meter. Its strength is determined by assuming a 1.0 kg mass (weight of largest single rotating component) traveling at 50 m/s (maximum tip velocity) strikes the shield at mid-span between supports. Using the method described in [4.1] or [4.2] to calculate the depth of penetration provides a factor of safety of three or greater under these conservative assumptions.

A schematic of the cooling water system is shown in Figure 4-4. Tap water is filtered and passed through a pressure regulator to reduce the pressure. A pre-heater is installed to allow positive control of the cooling water inlet temperature. A rotating

coupling passes the cooling water onto the rotor. Once there, it passes through a cooling jacket absorbing heat from the condenser section of the test thermosyphon. Another rotating coupling takes the water off the rotor where it passes through a second filter just prior to the flow meter. Upon exiting the flow meter, the cooling water is discarded into the city sewer drain.

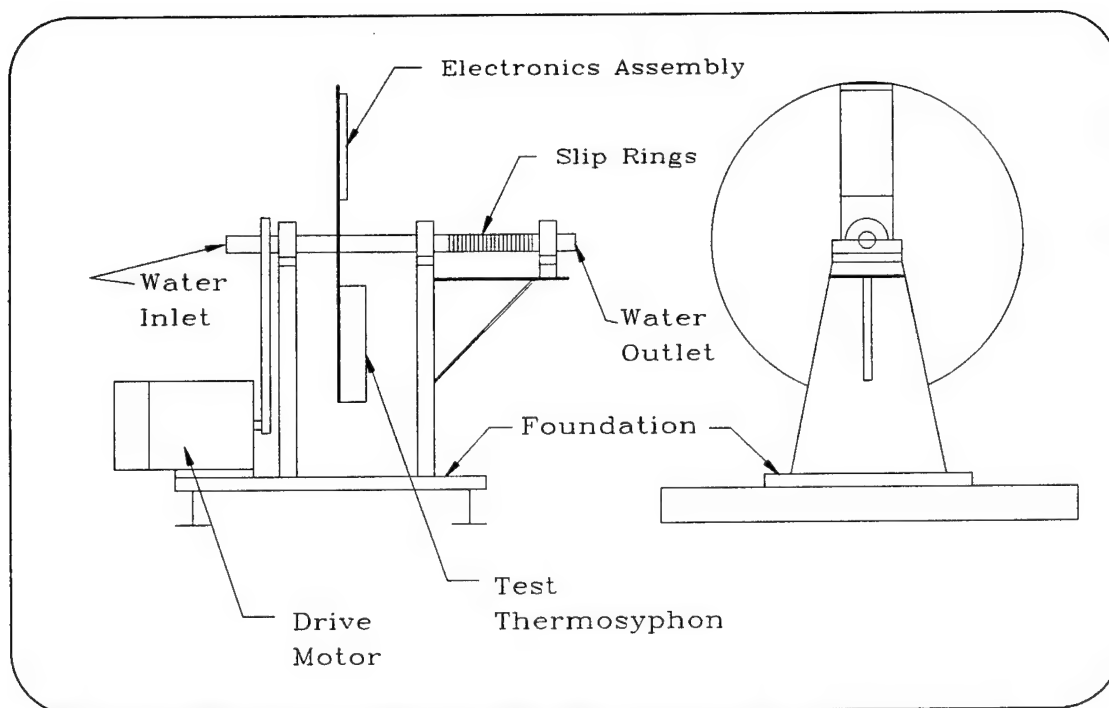


Figure 4-3: Thermosyphon Test Stand

The heater system consists of a regulated D.C. power supply connected to a resistance heater via carbon brushes and copper slip rings. Electric fans supply cooling air to the brushes and slip rings. The heater itself is a hollow cylinder of brass around which Nickel-Chromium resistance wire was wound. The resistance wire is potted inside two layers of thermally conductive ceramic. The heater is sized to produce 2.0 kW of power

at the maximum voltage rating of the power supply. It attaches to the outside of the test thermosyphon evaporator section via machine threads coated with heat-sink compound. The outside diameter of the heater is insulated to minimize heat loss to the surroundings.

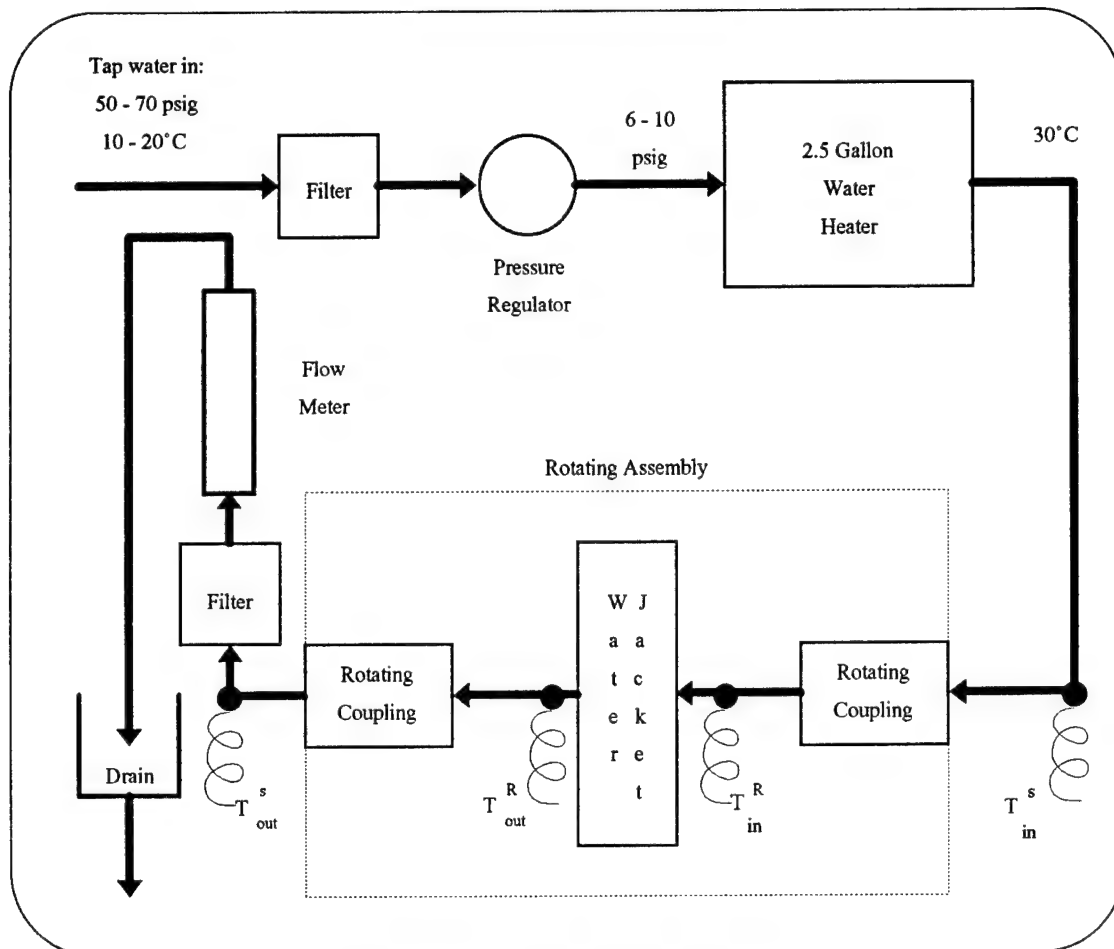


Figure 4-4: Cooling Water System

The instrumentation installed on the test stand consists of a flow meter (rotameter type), pressure transducer, optical speed sensor circuit, a pc-based 8-channel data acquisition system and a 16-channel thermocouple multiplexer/amplifier board. Figure 4-5 shows a schematic of the instrumentation system. The multiplexer board is mounted on the rotor and is connected to the data acquisition system via copper slip rings and carbon

brushes. This arrangement sends three high-level (0-10 volt) analog signals across the slip rings: the multiplexed thermocouple signal, the pressure transducer signal and the cold junction compensation signal. The slip ring noise is canceled out by recording the voltage of a shorted input and subtracting this from the recorded input voltages.

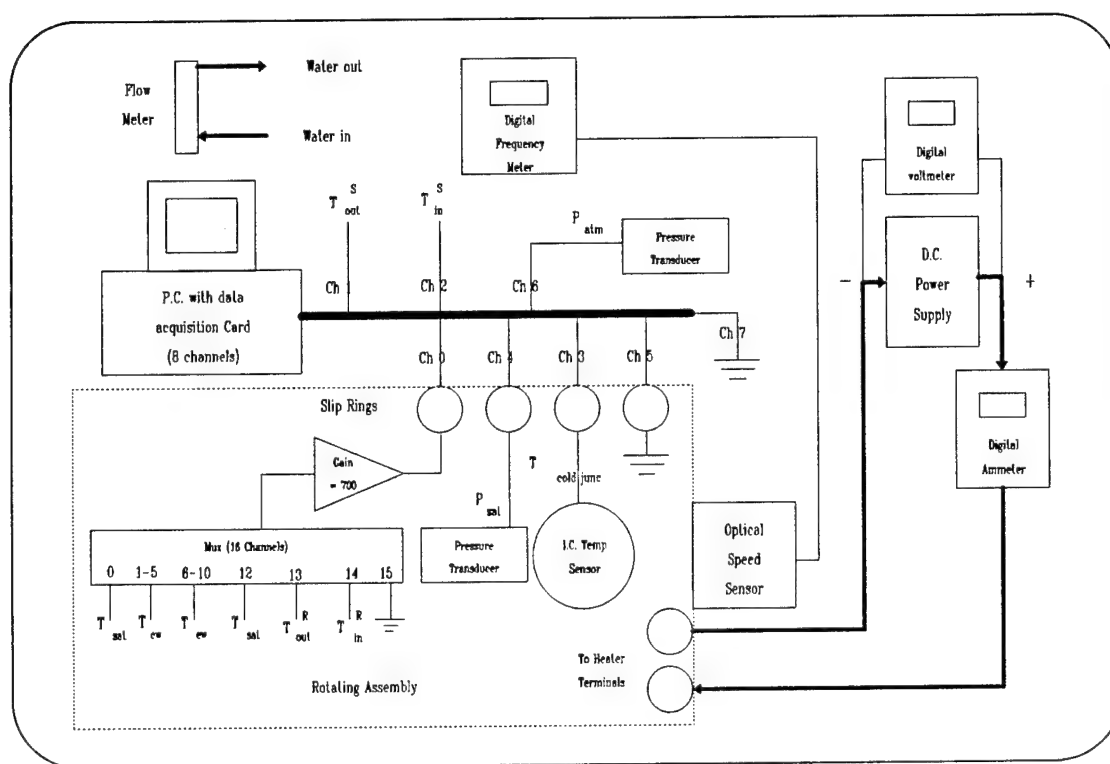


Figure 4-5: Instrumentation Block Diagram

Hand-held meters are used to read the input current and voltage as well as the shaft speed. These three measurements and the flow meter must be read manually, all temperature and pressure data are automatically recorded via the PC data acquisition system.

4.4 Accuracy and Error Analysis

All measurements are imperfect attempts to determine an unknown quantity. Consequently, every measurement contains errors. These errors fall into two categories, systematic and random. Random errors are easily reduced by taking repeated readings. Systematic errors can only be eliminated by taking independent measurements using different techniques [4.3].

The systematic errors in the temperature measurements were reduced by calibrating the data acquisition system so that its output matched the reading of a calibrated glass bulb thermometer over the expected temperature range of 30-100° C. The flow meter was calibrated by measuring the volume of water passing through the meter in a fixed amount of time.

The random errors were reduced by taking repeated readings and averaging. Data was collected over a 10 minute period for each data point. The manual readings were taken at one-minute intervals whereas the data acquisition system recorded all measurements at one-second intervals.

Confidence limits on the temperature measurements are determined via standard statistical methods. Hogg & Ledolter [4.4] shows that confidence limits are calculated from:

$$P\left[\bar{X} - z\left(\frac{\alpha}{2}\right)\frac{\sigma}{\sqrt{N}} \leq \mu \leq \bar{X} + z\left(\frac{\alpha}{2}\right)\frac{\sigma}{\sqrt{N}}\right] = 1 - \alpha \quad (4.4)$$

which says the probability that the true mean (μ) lies within $z(\alpha/2)\frac{\sigma}{\sqrt{N}}$ of the sample mean (\bar{X}) is $1 - \alpha$, where $z(\alpha/2)$ is the area under the standard normal distribution curve from minus infinity to $\alpha/2$ and N is the number of samples taken. Equation (4.4) assumes that

the underlying distribution is normal with mean μ and variance σ^2 . For 95% confidence intervals $\alpha = 0.05$ which makes $z(\alpha/2) = 1.96$ [4.4].

A numerical example shows how this is applied to the measurements taken in the experiment. The selected temperature measurement is the worst-case encountered in the data. The measured inputs are the raw voltage, shorted voltage, cold junction voltage and slip ring voltage. For our example, these inputs are:

$$\begin{aligned}\bar{V}_{\text{raw}} &= 5.40126 \text{ mV}; s = 0.3826 \text{ mV} \\ \bar{V}_{\text{shorted}} &= 1.60133 \text{ mV}; s = 0.44998 \text{ mV} \\ \bar{V}_{\text{cjc}} &= 1.76722 \text{ V}; s = 0.36407 \text{ V} \\ \bar{V}_{\text{slipring}} &= 1.16734 \text{ V}; s = 0.34671 \text{ V}\end{aligned}$$

where $N = 516$ samples have been taken for each. Since N is large (greater than 30) the sample standard deviation (s) is assumed to be equal to the population standard deviation (σ). Using equation (4.4) the 95% confidence intervals on these inputs are:

$$\begin{aligned}\bar{V}_{\text{raw}} &= [5.368, 5.434] \\ \bar{V}_{\text{shorted}} &= [1.563, 1.640] \\ \bar{V}_{\text{cjc}} &= [1.736, 1.799] \\ \bar{V}_{\text{slipring}} &= [1.137, 1.197].\end{aligned}$$

The temperature of the cold junction is calculated from:

$$T_{\text{cjc}} = 40.0 \cdot (\bar{V}_{\text{cjc}} - \bar{V}_{\text{slipring}}) \text{ [deg. C]} \quad (4.5).$$

In our example this is:

$$T_{\text{cjc}} = [21.6, 26.5] \text{ deg. C.}$$

This temperature is entered into the National Bureau of Standards (NBS) thermocouple Tables to determine the cold junction voltage ($\bar{V}_{\text{coldjunct}}$). The temperature at the thermocouple is calculated from:

$$\bar{V}_{\text{corr}} = \bar{V}_{\text{raw}} - \bar{V}_{\text{shorted}} + \bar{V}_{\text{coldjunct}} \quad [\text{mV}] \quad (4.6)$$

This corrected voltage is entered into the NBS thermocouple equation to determine the measured temperature [4.5]:

$$T_{\text{corr}} = [80.5, 87.1] \text{ deg. C.}$$

It is emphasized that this $\pm 3.3^\circ\text{C}$ is a worst-case example. The vast majority of the data is within $\pm 2.5^\circ\text{C}$ or less. It is also worth noting that the majority of the uncertainty in the temperature measurement comes from the cold junction temperature. Since the heat transfer coefficients are calculated from temperature differences, rather than absolute temperatures, the uncertainty in the cold junction temperature has no effect on those calculations.

A similar analysis carried out on the flow meter reading shows that the largest standard deviation ($s=0.483$) of the raw reading results in 95% confidence limits on the heat flow of ± 0.18 Watts/ $^\circ\text{C}$ of cooling water temperature difference. For a typical temperature difference of 10°C this gives confidence limits on the heat flow less than two watts.

The above uncertainty can be carried through the calculation of the heat transfer coefficient or Nusselt number in non-dimensional form. The measured Nusselt number is:

$$\overline{\text{Nu}} = \frac{QL}{kA\Delta T} \quad (4.7)$$

where k is the thermal conductivity, L and A are the characteristic length scale and heat transfer area, respectively. For the numerical example cited above, equation (4.7) evaluates to:

$$\overline{Nu} = 5737 \pm 1620$$

which is a 95% confidence level of $\pm 28\%$ using the $\pm 3.3^\circ\text{C}$ temperature confidence limits. Again, this is the extreme case, the typical uncertainty is around $\pm 20\%$.

- 4.1 U.S. Navy, *Explosives Effects & Properties*, (Confidential) NOLTR 65-218, Section used herein is Unclassified.
- 4.2 Wierzbicki, T. & Hoo Fatt, M., "Deformation and Perforation of a Circular Membrane due to Rigid Projectile Impact," *Dynamic Response of Structures to High-Energy Excitations*, ASME, 1991.
- 4.3 Baker, H.D., Ryder, E.A. & Baker, N.H., *Temperature Measurement in Engineering*, Omega Engineering, Inc., Stamford, CT, 1975.
- 4.4 Hogg, R.V. & Ledolter, J., *Engineering Statistics*, Macmillan, New York, NY, 1987.
- 4.5 "Practical Temperature Measurements," *The Temperature Handbook*, Omega Engineering, Inc., Stamford, CT, 1992.

Chapter 5: Results and Conclusions

5.1 Experimental Results

Figures 5-1 through 5-15 at the end of this chapter summarize the experimental results. Figures 5-1 to 5-3 show in dimensional form, the effects of effective gravity, working fluid and length to diameter ratio in the condenser. The overall trend in these graphs shows that heat flux is proportional to temperature difference.

Recall that the definition of a convective heat transfer coefficient is:

$$h \equiv \frac{q}{\Delta T} \quad (5.1).$$

Figure 5-1 shows that the heat transfer coefficient increases with effective gravity as was predicted in Chapter 3. This is observed by noticing that for any given temperature difference, the measured heat flux increases with relative gravity.

The effect of working fluid is depicted in Figure 5-2. For a given temperature difference, the heat flux is higher with methanol than with ethanol. This is a consequence of the higher heat of vaporization of methanol. This is also predicted from the results of Chapter 3.

Figure 5-3 shows the effect of the L/D ratio on the condenser. The only discernible difference between the three L/D's tested is that the smaller one ($L/D = 30$) exhibits a large amount of scatter in the data whereas data from the larger L/D ratio thermosyphons are more consistent. This is probably attributable to two-dimensional effects which cannot be predicted with the one-dimensional model used in Chapter 3.

Figures 5-4 to 5-7 show the same data in non-dimensional form. These results confirm the relationship predicted by equation (3.26) for the condenser heat transfer coefficient. Figures 5-4 and 5-5 show that the effects of both the effective gravity and the working fluid are accounted for by equation (3.26). The experimental results appear to be about 20% higher than the theoretical predictions. However, Figures 5-6 and 5-7 show that this is largely due to the use of the smaller ($L/D = 30$) thermosyphon where the two-dimensional effects come into play.

Figure 5-8 shows the effect of the fill ratio on the maximum heat flux. Thermosyphons were tested at fill ratios from 11% to 85%. Recall that the fill ratio is defined as the ratio of liquid volume to evaporator volume. At both extremes, failure occurred at very low heat fluxes and showed little improvement with increased effective gravity. In the intermediate range, there was significant improvement in the maximum heat flux with increased effective gravity. There appears to be an optimum fill ratio in the vicinity of 35-45%. At the lower fill ratios, the early failure is caused by evaporator dry-out. At the higher fill ratios, the early failure is caused by condenser flooding. This is consistent with previous results on gravitational thermosyphons published in references [5.1] and [5.2]. The filling method employed did not allow precise control over the fill ratio so this portion of the results is considered very approximate. See Appendix A for more discussion of the filling method.

The evaporator data is plotted in Figures 5-9 to 5-14. The dimensional data is presented in Figures 5-9 to 5-11. Because of the large amount of scatter in this data, the regression line on these figures is of little value and not much can be said about Figures

5-9 and 5-10. Figure 5-11 does exhibit the same behavior as that of Figure 5-3 for the condenser. That is, the scatter in the data is reduced at the higher L/D ratios. Eliminating the L/D = 30 data from Figures 5-9 and 5-10 will result in a relationship between heat flux and temperature difference similar to that found in Figures 5-1 and 5-2 for the condenser. This is shown in Figure 5-16.

The nondimensionalized data in Figures 5-12 to 5-14 clearly shows the evaporator heat transfer is a combination of pool boiling as predicted by equation (3.44) and film evaporation which is predicted by equation (3.33). The data shows that equation (3.33) is fairly accurate for Nusselt numbers above about 2500. When equation (3.33) predicts a Nusselt number below 2500, the actual Nusselt number remains fairly constant at that value. This suggests the following relationship to predict the evaporator heat transfer coefficient:

$$\overline{Nu}_{Le} = \frac{\bar{h}L_e}{k_l} = \max \left\{ \frac{\frac{Pr}{4Ja} \cdot \left[Re_L^{1.22} - \frac{3Ja(X_e+L_e)^{4/3} - X_e^{4/3}}{(\sqrt{v/\omega})^{4/3}} \right]^{0.82}}{2500} \right\} \quad (5.2).$$

Therefore, equations (4.8) and (3.26) should be used to predict the evaporator and condenser heat transfer coefficients, respectively.

In order to examine the extent of the Coriolis effect, one set of tests was run with the direction of rotation reversed so that the wall temperature thermocouples were located on the leading vice the trailing edge. As described in Chapter 3, the Coriolis effect causes the film to be thinner on the leading edge. This is demonstrated in Figure 5-15 by a smaller temperature difference for a given level of heat flux. Figure 5-15 also shows that

this effect is rather small as expected. It is also interesting to note that dry-out failure was observed at a lower heat flux when the thermocouples were located on the leading edge. This phenomenon is also predicted in Chapter 3. All data gathered in the experimental portion of this thesis are located on the enclosed floppy disks in Lotus 123 Release 4 format. A summary of the data is tabulated in Appendix B.

5.2 Preliminary Design Tool

A computerized preliminary design tool has been developed for sizing multi-disk axial gap propulsion motors to a specific ship application. This allows the ship designer to easily conduct trade-off studies to determine the best propulsion plant configuration for a particular set of ship requirements. Figure 5-17 shows the input and output sections of the design tool. The heat transfer section is summarized in Figure 5-18. Stator cooling is via indirect water and rotor cooling is via radial rotating thermosyphons. Air cooling of the thermosyphon condensers is evaluated both with and without fins for comparison with water cooling of the condensers. Air gap heat transfer is also considered in the heat transfer model. Other heat transfer paths are negligible by comparison and are ignored. The equations developed in Chapters 2 and 3 constitute the core of the design tool.

The design tool was written as a spreadsheet in the Lotus 123 release 4 program. A spreadsheet format was chosen because it allows the user to change any input and immediately see the effect on any of the outputs. The spreadsheet has four pages. Figures 5-17 and 5-18 constitute pages one and two, respectively. Page three contains various property data and page four is a record of changes log. The shaded blocks in Figure 5-17

constitute the design inputs. Additional inputs are the empirical boiling coefficients located in the shaded area in Figure 5-18 and the various material properties located in shaded regions of page three of the spreadsheet (not pictured).

Additionally, the user must use the "solver" feature of the spreadsheet program to solve the two implicit equations in the spreadsheet. The first comes from equation (2.38) in the structural model. The key sequence *ALT-R-A-S* brings up the solver dialog box. Cell A:B49 is selected as the adjustable cell and cell A:B50 is the constraint cell. There is no optimal cell. Select enter and the spreadsheet will solve the implicit equation using a Newton-Raphson technique. The second implicit loop comes about from the heat transfer model. The thermosyphon design section uses the total heat transfer required as an input to calculate the winding temperature whereas the air gap heat transfer section uses the winding temperature and the incoming air temperature to calculate the total amount of heat transfer obtained. Since other heat transfer paths are neglected, conservation of energy requires the total heat transferred via these two paths to equal the total losses generated. This sequence of equations creates an implicit loop in the spreadsheet. This loop is also solved with the "solver" function by specifying cell B:E8 as the adjustable cell and B:E12 as the constraint cell. With all of the inputs specified and the two implicit equations solved, the design is complete at this level of detail. A copy of the design tool is included on the disks attached to this thesis.

Synchronous Machine Design Program									
Axial Field Motor									
Date: 5-8-95									
Inputs are shaded									
Design Parameters									
Terminal Voltage	750	Volts							
Rated Speed	164	rpm							
Rated Frequency	188.5	rad/sec							
Rated P.F. angle	0.451	rad							
Outer radius, Ro	1.08	m							
Inner radius, Ri	0.65	m							
Air gap, g	0.01	m							
No. of air gaps, ng	10								
Pitch, p	0.889								
No. of slots/pole - phase, q	3								
Stator space factor, lams	0.7								
Stator slot depth, hs	0.027	m							
Stator slot factor, SSF	0.8								
Lams at outer radius =	0.42	m							
Core lamination thickness	0.0005	m							
No. rotor slots/pole, qr	4								
Rotor slot depth, hr	0.022	m							
Rotor space factor, lamr	0.7								
Rotor slot factor, RSF	0.8								
Lamr at outer radius =	0.42	m							
Stator electric loading, Ks	2.0E+05	A/m							
Peak flux density in iron, Bs	1.8	T							
Peak air gap flux density, Bgap	1.2	T							
Max. cooling air velocity, Vs	25	m/s							
Cooling Air entry temp., To	30	deg. C							
Tsat	100	deg. C							
Thermosyphon Diameter, D	0.007	m							
Fill Ratio	0.2								
Insulation Thickness	0.005	m							
Insulation thermal Cond.	2	W/m-K							
Fin Spacing	0.01	m							
Fin Thickness	0.001	m							
Thermal Conductivity of Alum.	111	W/m-K							
Structural Design									
Shaft Outer Diameter	0.509	m							
Shaft Inner Diameter	0.408	m							
Shaft Cross Section	0.07339	m^2							
Torque per Disk	307026	N-m							
Structural Outer Radius, r_oo	1.39	m							
Structural Inner Radius, r_ii	0.46	m							
Rotor Disk Thickness	0.0023	m							
Stator Disk Thickness	0.0018	m							
Drum Inner Diameter	0.904	m							
Case Outer Diameter	2.78	m							
Solver Constraint Cell	0								
Weight and Volume									
Stack length, L	0.846	m							
Air gap volume	0.234	m^3							
Back iron vol.	0.491	m^3							
Stator iron vol.	0.395	m^3							
Stator Winding volume	0.502	m^3							
Rotor Winding volume	0.426	m^3							
Rotor steel vol.	0.677	m^3							
Case vol.	0.019	m^3							
Shaft volume	0.062	m^3							
Machine volume	5.145	m^3							
Rotor weight	9077	kg							
Stator weight	7543	kg							
Back iron weight	3831	kg							
Case weight	146	kg							
Machine weight	20597	kg							
Machine weight	20.3	LT							
Variables of Interest									
eaf	2.00	per unit							
xd	1.35	per unit							
Jas	7.4E+06	A / m^2							
Jfs	7.7E+06	A / m^2							
volume	5.14	m^3							
weight	20.3	LT							
Efficiency	96.2%								
Traction	24.61	psi							
Power	2.6E+07	W							
Power	35355	HP							
Stack Length	0.846	m							
Stator									
# of pole pairs, p	11								
No. of series stators, Ss	10								
Pitch factor, kp	0.985								
Breadth factor, kb	0.960								
Voltage, Va	102	Volts/turn							
Current, Ia	95295	Amp-turns							
Rated Apparant Power	2.93E+07	V-A							
Base Impedance, Zb	0.00108	Ohms/turn^2							
Slot current density, Jas	7.4E+06	A / m^2							
Cu current density, Ja	9.3E+06	A / m^2							
Turn Length, lt	1.30	meters							
Resistance, Ra	2.14E-05	Ohms/turn^2	0.0199	per unit					
Flux per pole, phi	0.08133	Webers							
Back iron depth, tb	0.105	meters							
Slot width, ws	0.014	meters							
Rotor									
No. of series rotors, Sr	10								
Tip speed, u	18.5	m / s							
Rotor breadth factor	0.958								
Radius ratio, a	0.60								
excitation, eaf	2.00	per unit							
turn length, ltf	1.36	meters							
field resistance	9.1E-06	Ohms/turn^2	0.0085	per unit					
N / L field	121563	Amp-turns							
Full load field	243402	Amp-turns							
Cu current density, Jf	9.7E+06	A / m^2							
Slot current density, Jfs	7.7E+06	A / m^2							
Electric loading, Kf	1.7E+05	A / m							
Slot width, wr	0.033	meters							
Reactances									
Leakage	5.77E-05	Ohms/turn^2	0.05	per unit					
Xaao	9.31E-04	Ohms/turn^2	0.87	per unit					
D-axis, xd	1.45E-03	Ohms/turn^2	1.35	per unit					
Losses									
Stator copper	583325	Watts	0.0199	per unit					
Windage & frict.	35	Watts	0.0000	per unit					
Core loss	24741	Watts	0.0008	per unit					
Field copper	540899	Watts	0.0185	per unit					
Total Losses	1149000	Watts	0.0392	per unit					
Efficiency	96.2%								
Heat Transfer Summary									
Stator air-gap heat loss	136708	Watts							
Rotor air-gap heat loss	302870	Watts							
Rotor t'syphon heat loss	238029	Watts							
Stator water heat loss	471359	Watts							

Figure 5-17: Design Tool Input and Output Sections

Synchronous Machine Design Program

Heat Transfer Design

Heat generated in stator	608066	W	Thermosyphon Design		
Heat generated in rotor	540899	W	Total # of rotor slots	878	
Total Heat to be removed	1148965	W	Number of slots / disk	88	
Cooling air mass flow rate	16.9	kg / sec	Req'd heat flow per pipe	271	Watts
Cooling air temperature rise	67.4	deg. C	Total req'd heat flow	238029	Watts
Cooling air exit temperature	97.4	deg. C	Required heat flux, qhp	7.04E+06	W/m^2
Avg cooling air temp	63.7	deg. C	Nucleate Boiling Coeff.	0.013	
			Nucleate Boiling Exp.	2	
			Solver Constraint Cell	0	
Air Gap Heat Transfer					
Total Rotor surface area, Ar	23.4	m^2	General Outputs:		
Total Stator surface area, As	23.4	m^2	H/P X-sectional area	3.85E-05	m^2
Gap Ratio, G = g/ro	0.009		Heat pipe perimeter	0.021991	m
Hydraulic Diameter, Dh	0.02	m	Transition Re_tr	3186	
Volume flow rate	1.02	m^3/s	Min. Inner Cond Radius	0.10	m
Flow Coefficient, Cw	5.42E+04		Length / Dia. Ratio	140	
Rotational Reynolds #, Reo	1.15E+06		Characteristic Length	1.32E-04	m
Radial Reynolds #, Rer	2.93E+06				
Rotor Nusselt Number, Nur	3762		Condenser Outputs:		
Rotor heat transfer coef, hcr	100	W/m^2-K	Condenser length, Lc	0.366	m
Stator Nusselt Number, Nus	1698		Condenser Area, Ac	8.05E-03	m^2
Stator heat transfer coef, hcs	45	W/m^2-K	Condenser Constant	0.3141	m^4/3
Rotor heat removed via a/g	302870	W	Cond. Heat Flux, q_c	33668	W/m^2
Rotor heat removed via t/s	238029	W	Cond. Temp Diff.	1.34	deg. C
Stator heat removed via a/g	136708	W	Cond. Wall Temp, Tcw	98.7	deg. C
Stator heat removed via H2O	471359	W	Jakob No.	0.002509	
			Exit Reynolds No.	76.9	
From Thermo Tables @Tsat:	-26800				
hfg	2.257E+06	J/kg	Evaporator Outputs:		
nu_l	3.000E-07	m^2/s	Evaporator Length, Le	0.344	m
Rho_l	958.0	kg/m^3	Evaporator Area, Ae	7.56E-03	m^2
k_l	0.6810	W/m-K	Evaporator Constant	0.4290	m^4/3
Rho_v	0.5978	kg/m^3	Evap. Heat Flux, q_e	35834	W/m^2
Pr_l	1.76		Evap Temp Diff., Evap	1.75	deg. C
Cp_l	4212.0	J/kg-K	Pool Char. Length grp.	0.0078	
mu_l	2.85E-04	kg/m-s	Pool Depth	0.086	m
Sigma	5.89E-02	N/m	Pool Constant	0.116056	m^4/3
			Evap Temp Diff., Pool	3.7	deg. C
			Design Temp Diff.	3.7	deg. C
			Evap. Wall Temp, Tew	103.7	deg. C
			Winding Temperature	193.3	deg. C
Finned Condensers:					
Total Flow Area w/o fins	0.421	m^2	Air Cooling of Condenser:		
Total Flow Area with fins	0.379	m^2	Longitudinal Spacing	0.012	m
Adjusted Velocity	66.0	m/s	Avg. Transverse Spacing	0.033	m
Effective Outer Radius	0.013	m	Longitudinal Pitch	1.75	
Wetted Area	9.60E-05	m^2	Transverse Pitch	4.74	
Perimeter	0.039	m	Psi	0.834	
Hydraulic Diameter	9.80E-03	m	Phi	1.06	
Reynolds Number	3.71E+04		Max Velocity, V	30.0	m/s
f	0.022		Reynolds No.	12030	
Nusselt Number	122		Re < 1e4	52.55	
Heat Transfer Coefficient	356	W/m^2-K	2e4 < Re < 4e5	1.21	
Beta	80		4e5 < Re < 5e6	1.11	
Fin Efficiency	0.731		Nu_d1	63	
Total Fin Area per t'syphon	0.055	m^2	Nu	67	
Total Heat X-fer per t'syphon	989	Watts	Heat Transfer Coeff.	274	W/m^2-K
			Max. heat transfer to air	224.5	W / pipe w / o fins

Figure 5-18: Design Tool Heat Transfer Section

5.2.1 Design Example

The inputs of Figure 5-17 are chosen to produce a small diameter 35,000 HP motor suitable for a podded propulsion destroyer application. It is a 10 air gap or 5-disk design. Figure 5-19 is a scaled preliminary drawing of this design. Figures 2-5 and 2-6 also depict this specific design. Table 5-1 compares several other existing or proposed motor technologies at the same power and speed rating. Note the significant improvement in both volume and weight over the other technologies. The numerical values for the other technologies were obtained from [5.3].

In addition to the values obtained from [5.3], the permanent magnet single disk axial gap motor was simulated with the design tool. It is interesting to note that this motor is actually only a 30,000 HP motor vice the 35,000 HP advertised. Comparison of the starred (*) values calculated with the design tool and non-starred values for this motor show that the design tool is giving reasonable results. The weight difference is due to the difference between permanent magnet and wound field synchronous technologies. The length difference is accounted for by the fact that the design tool does not include a length allowance for journal or thrust bearings which are included in the other data. This length difference also accounts for the volume difference.

Comparison of the starred values in the last two columns of Table 5-1 show the advantages of the multi-disk technology over the next most recent proposed motor design. The multi-disk axial design provides a 29% weight reduction, a 40% volume reduction and nearly a 50% reduction in radius over the single-disk design while providing 16% more power.

	Conventional air-cooled	Conventional water-cooled	PM axial gap motor	Multi-disk Axial motor
Cooling method (Arm / Field)	air/air	Water/water	water/air	water/t'syphon
Armature current density (A/mm ²)	6.2	7.75	5	7.4
Field current density (A/mm ²)	7	7.75	N/A	7.7
Airgap flux density (T)	1.1	1.2	0.84	1.2
Electromagnetic shear stress (KPa)	216.7	283.2	158.2	246
Efficiency (%)	98	96.5	98.5	96.2
Radius (m)	2.9	2.2	2.1	1.1
Length (m)	3.7	4	1.2 / 0.4*	0.85*
Weight (LT)	112	51	22 / 28.1*	20*
Volume (m ³)	167	57	22.7 / 8.4*	5.1*

Table 5-1: Comparison of Motor Technologies

5.3 Conclusions and Recommendations for Future Research

Table 5-1 shows the significant volume and weight advantages of the multi-disk design developed in the course of this research. Of particular interest to the ship designer is the nearly 50% reduction in the motor diameter with the multi-disk geometry. This technology clearly shows promise and more research should be conducted in this area. The computer model developed herein is only the first step in evaluating this new motor geometry. It will however, allow ship trade-off studies to be completed to determine if the ship impacts predicted in the introduction are favorable enough to make electric drive cost competitive. Such trade-off studies are the first recommendation for future research.

The motor design tool developed in the course of this research is very well suited to being incorporated into an optimization program. This feature allows future

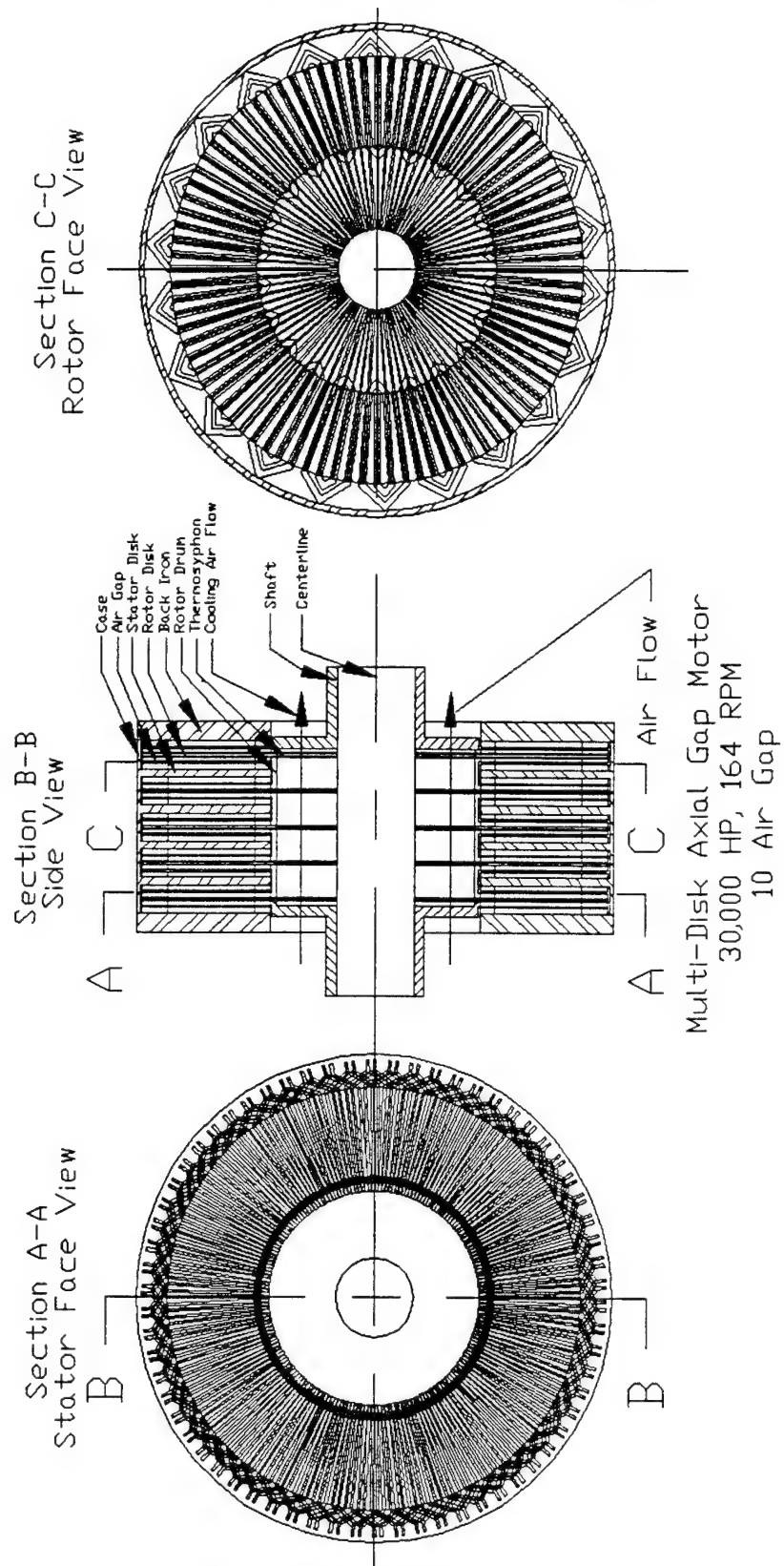


Figure 5-19: Motor Section Views

researchers to explore the entire design space of these unique motors, eventually developing an optimum geometry for ship propulsion motors. Once the preliminary design is optimized, a detailed design sequence should be undertaken. The detailed design should include a complete structural analysis and a more detailed electromagnetic analysis which includes harmonic effects, fringing fields and end turn effects. Once these analyses are completed, a prototype multi-disk motor should be built and tested.

This thesis has presented theoretical predictions with experimental verification of the heat transfer coefficients found in radial rotating thermosyphons. While this research is considered successful because of the agreement between theory and experiment, the application of thermosyphons to rotor cooling cannot yet be recommended without reservations. Specifically, the experimental portion of this research revealed that there are serious stability problems with the RRT.

It was noted during testing that the heat flux at failure was not path independent. Failure could be induced at different power levels for the same speed setting depending on how the operating point was approached (i.e. holding speed constant and increasing power or changing speed at a constant power level). Because of this hysteretic behavior, a prediction for the maximum heat flux could not be developed. Such a prediction is a necessity if optimal designs are to be generated. Once failure occurred, the thermosyphon had to be cooled to room temperature prior to restarting.

Transient testing was also not part of this research. Transient operation is an important part of the operating profile of a ship propulsion motor. It is recommended that any future research into radial rotating thermosyphons include transient effects.

Other areas which should be considered in future research are a more detailed study of the effects of fill ratio on the maximum heat flux, larger length to diameter ratios and other working fluids. It is believed that the theoretical predictions presented herein will exhibit good agreement with experiment for L/D ratios of 50 or greater. The motor design tool currently uses water as the working fluid. If the problems of freezing can be overcome, water will be a superior working fluid to the alcohols because of its very high heat of vaporization.

The shape of the thermosyphon cross-section should also be evaluated. All testing in the current research was carried out on circular cross-sections. However, as shown in Figure 3-6 a rectangular cross-section would be more effective for conducting the heat into the evaporator. Depending on the specific section chosen, the Coriolis effect may become more significant under operating conditions encountered in ship propulsion motors.

- 5.1 Feldman, K.T. & Srinivasan, R., "Investigatin of Heat Transfer Limits in Two-Phase Thermosyphons," *Research and development of Heat Pipe Technology, Proceedings of the 5th International Heat Pipe Conference*, Japan Technology & Economics Center, 1984.
- 5.2 Nguyen-Chi, H. & Groll, M., "Entrainment or Flooding Limit in a Closed Two-Phase Thermosyphon," *Advances in Heat Pipe Technology, Proceedings of the 4th International Heat Pipe Conference*, Pergamon, 1982.
- 5.3 US Navy, "ASMP Program Industry Brief," 4-5 May 1993.

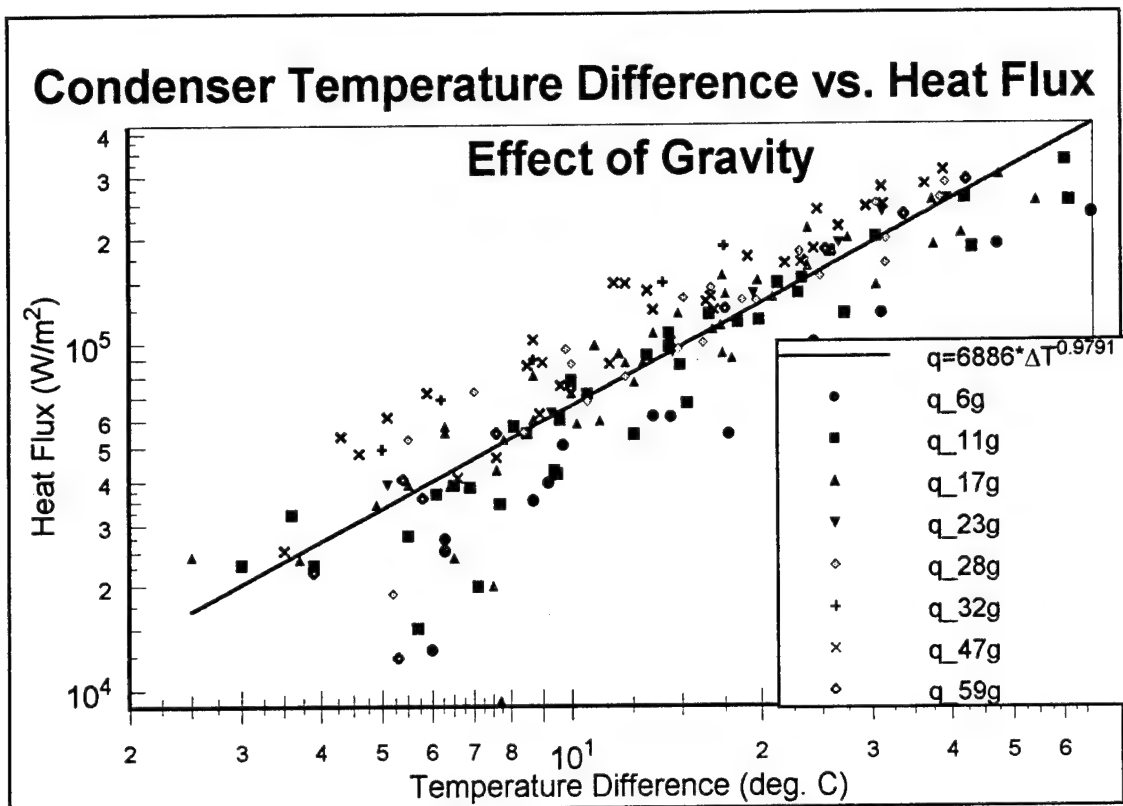


Figure 5-1

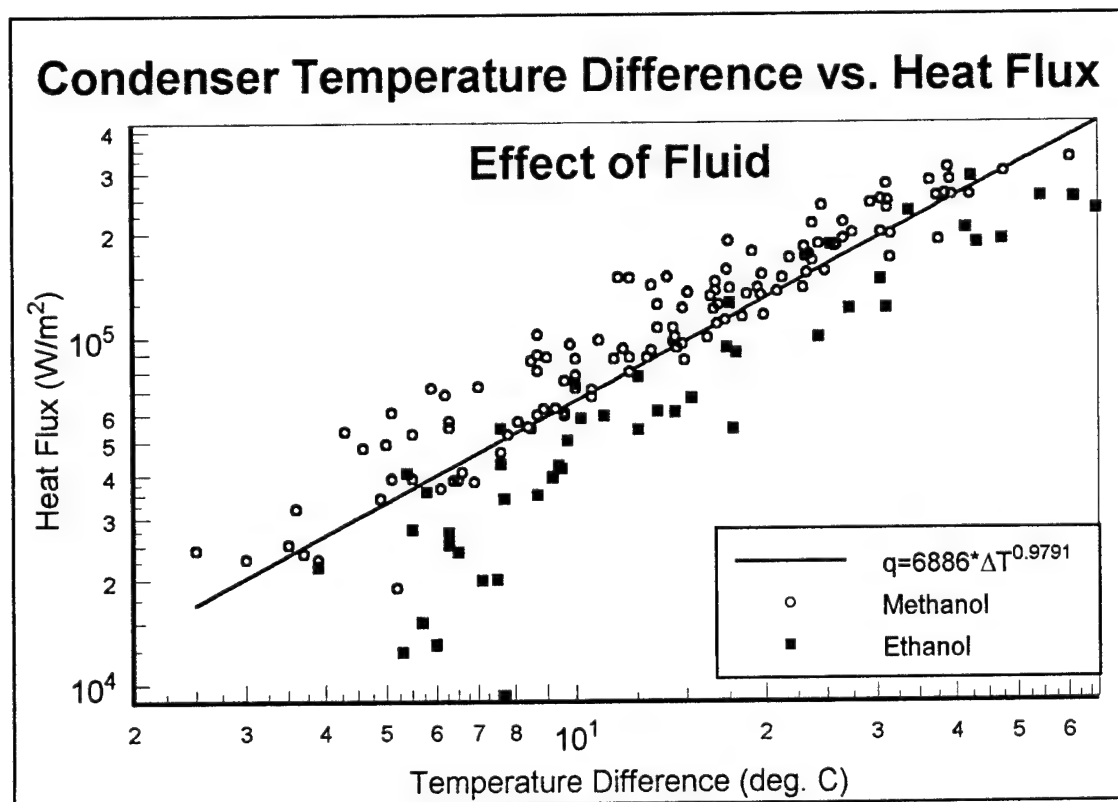


Figure 5-2

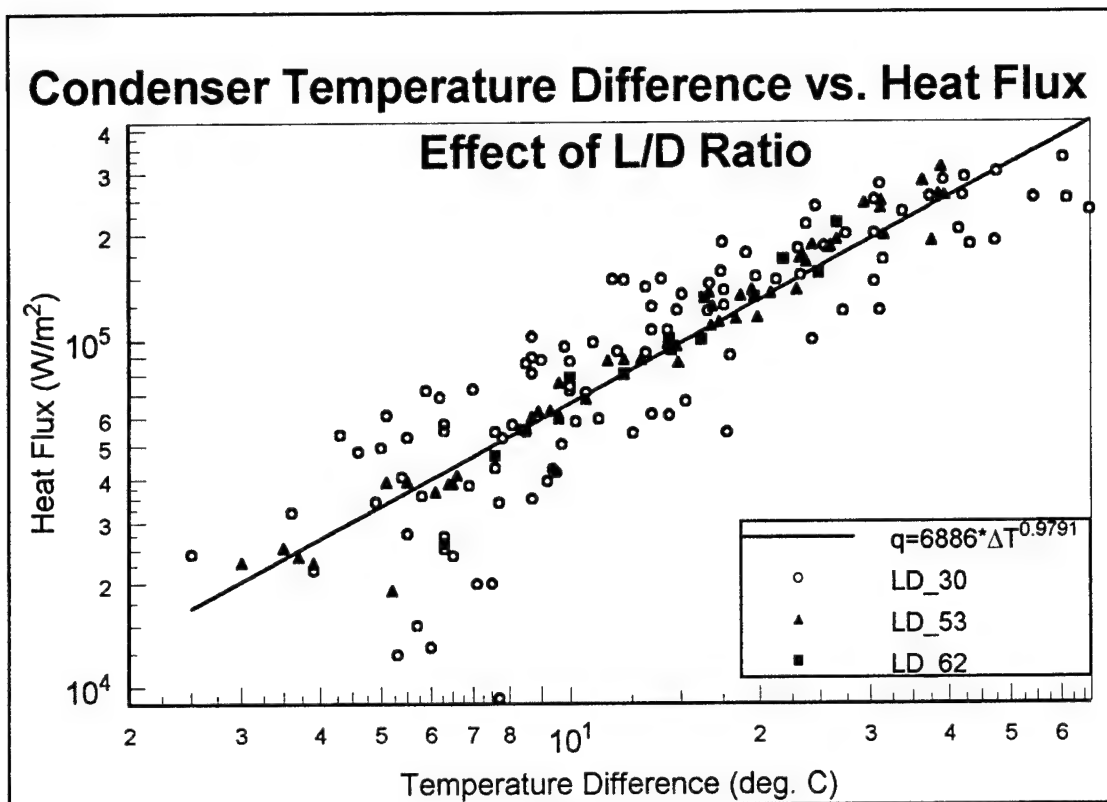


Figure 5-3

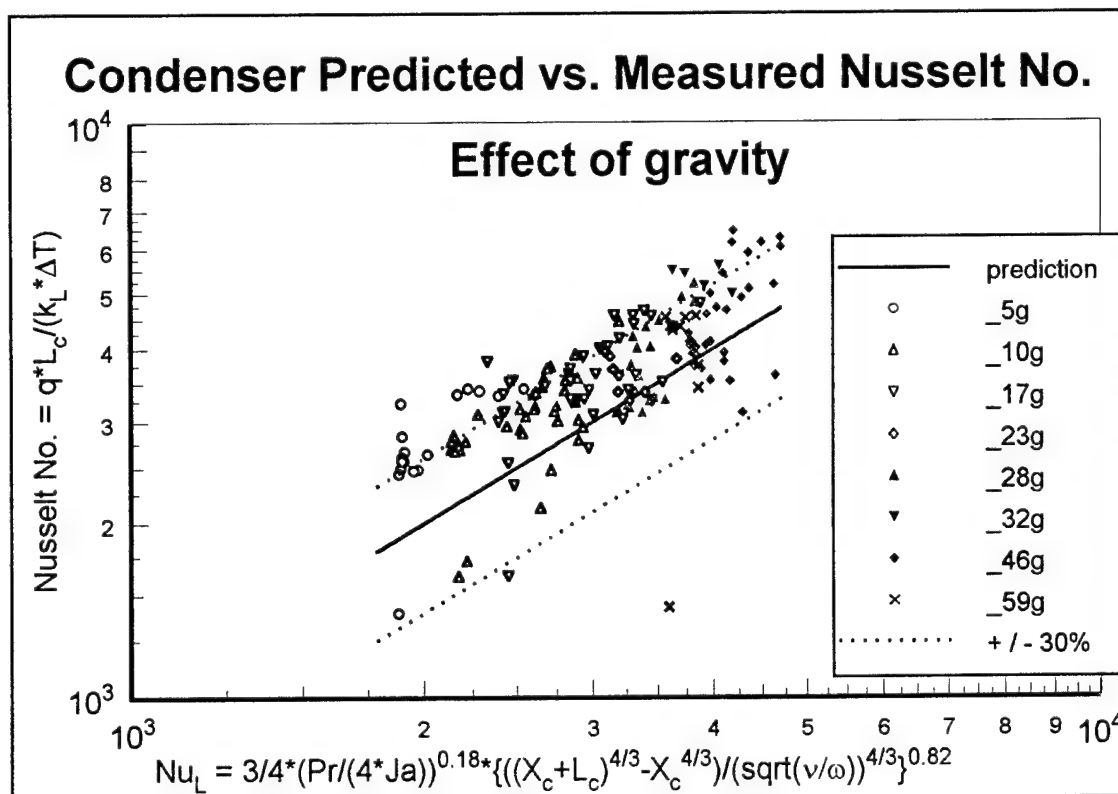


Figure 5-4

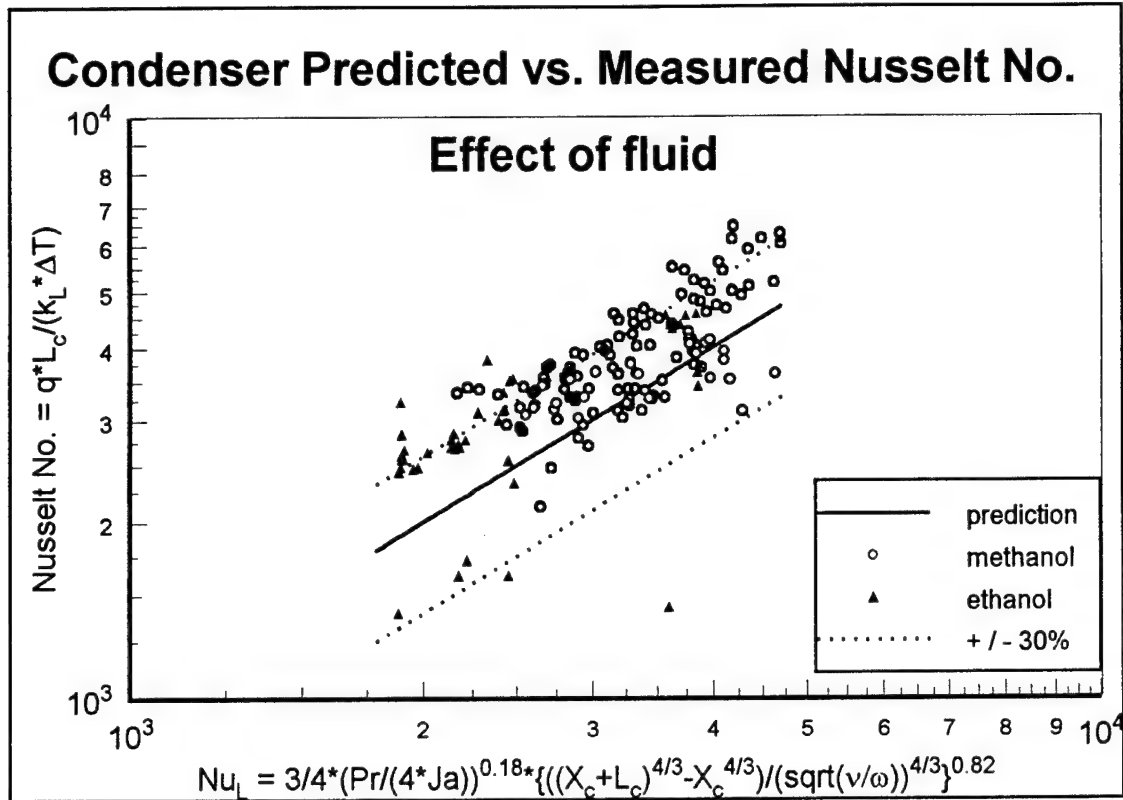


Figure 5-5

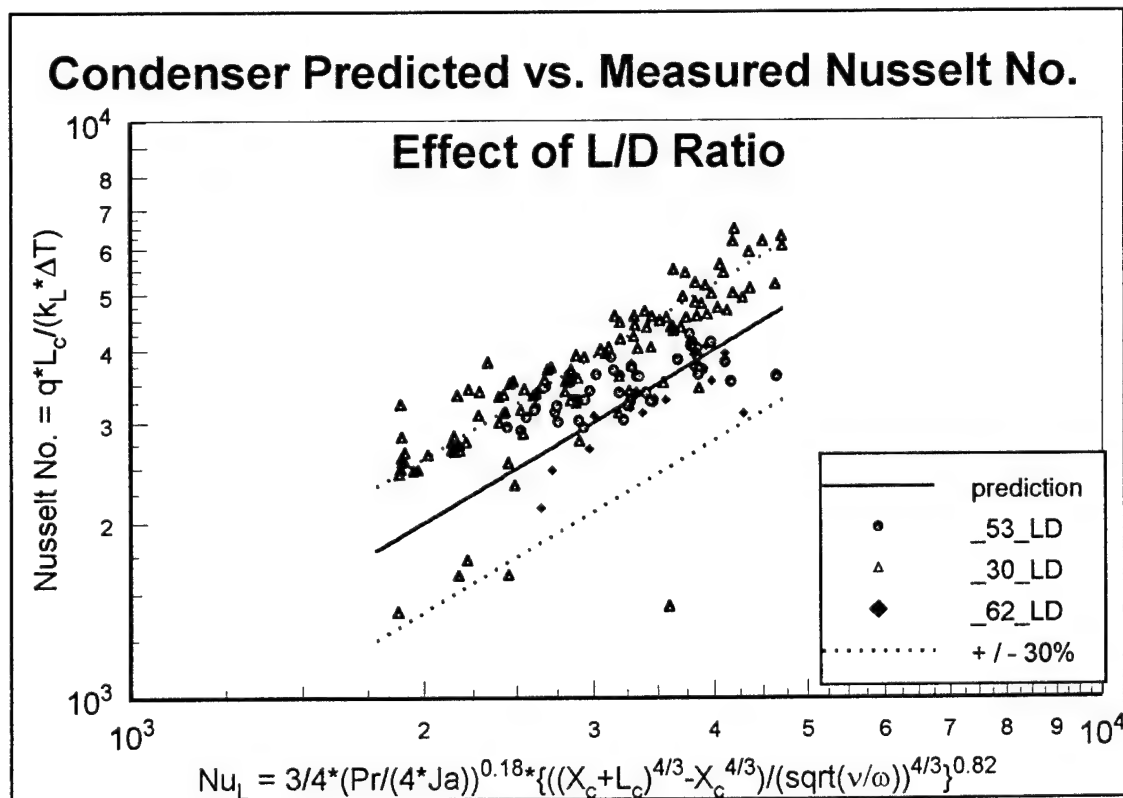


Figure 5-6

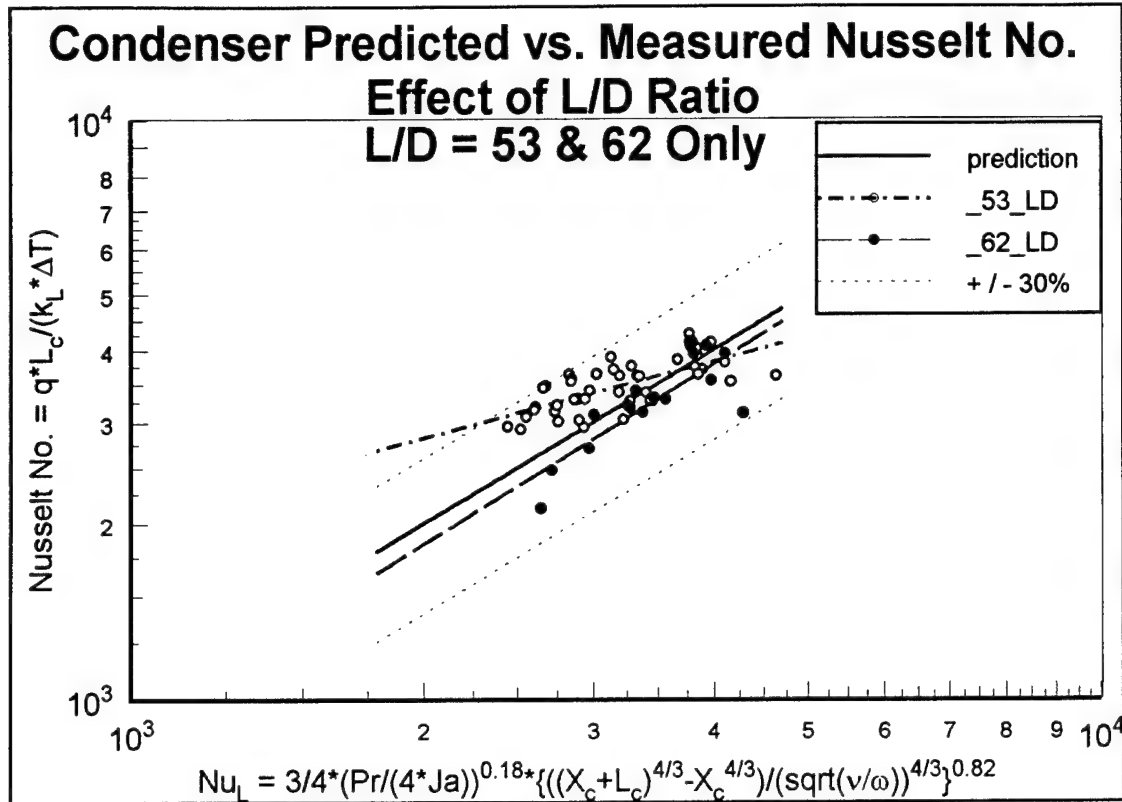


Figure 5-7

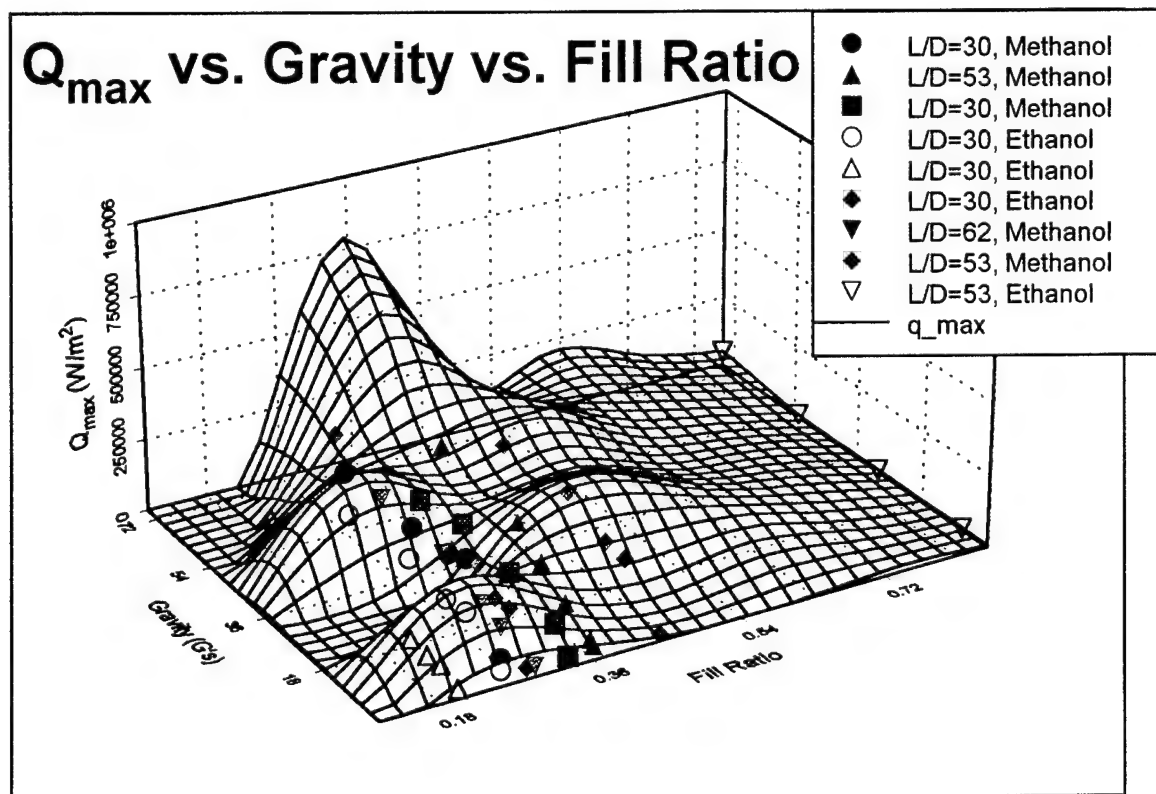


Figure 5-8

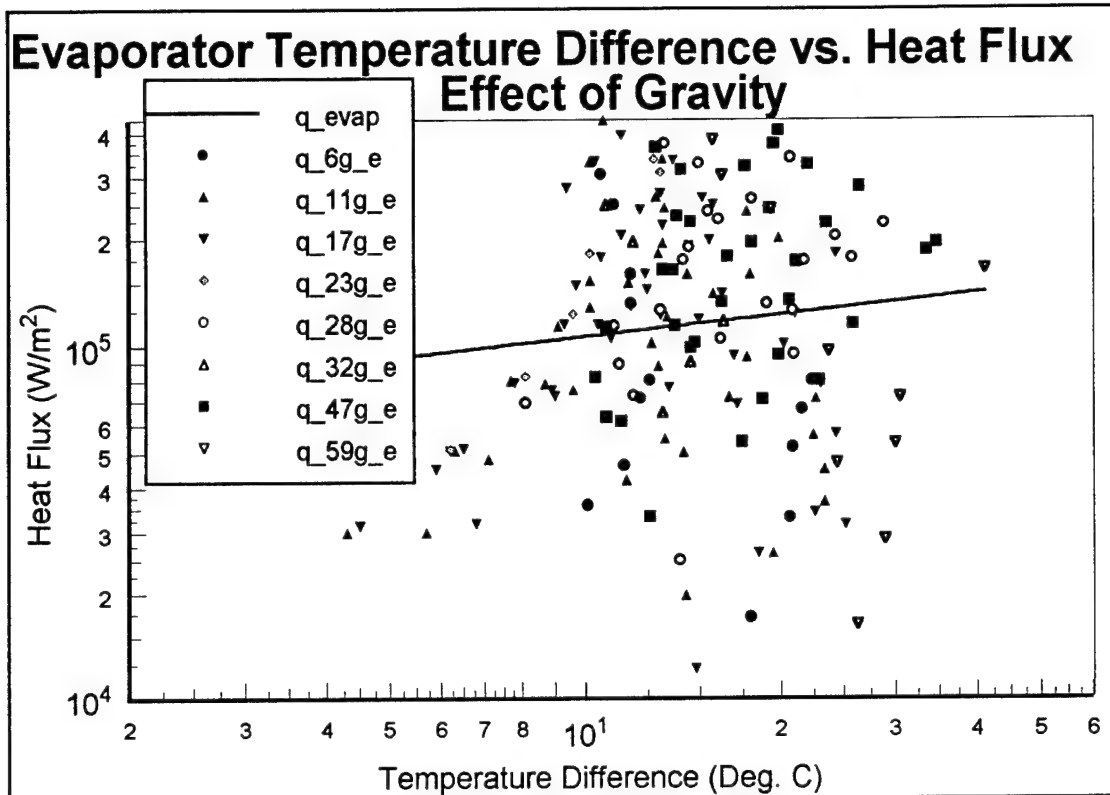


Figure 5-9

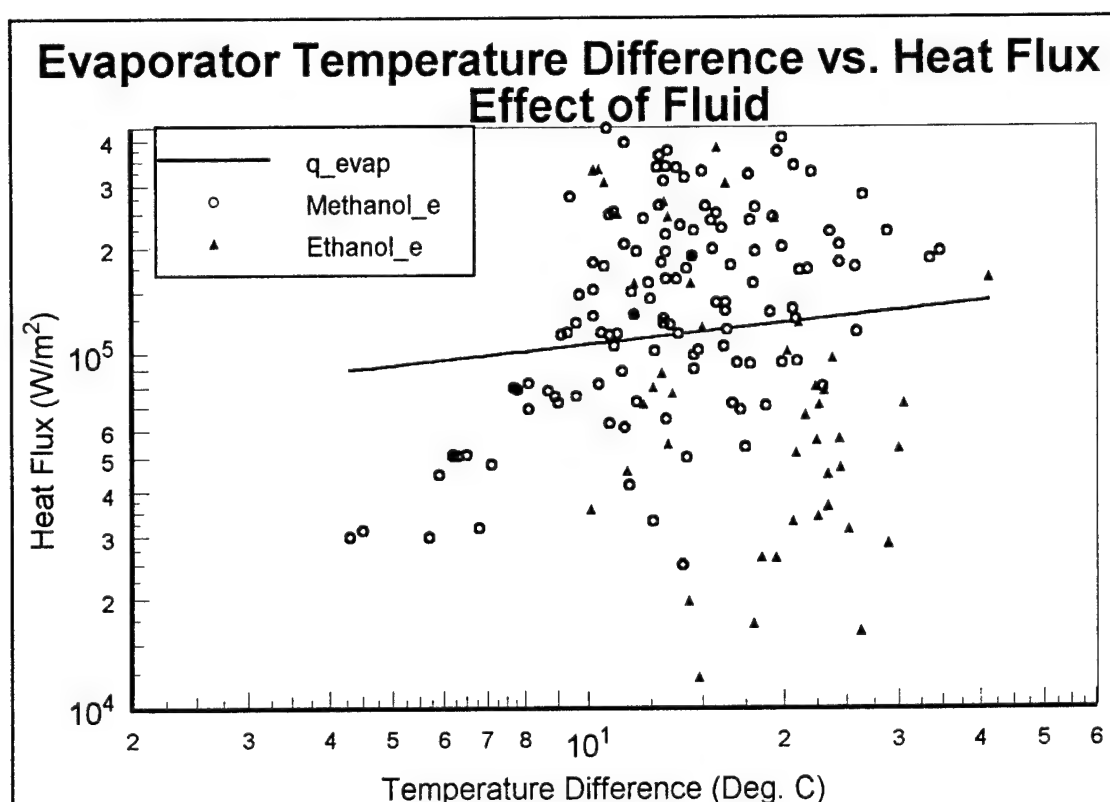


Figure 5-10

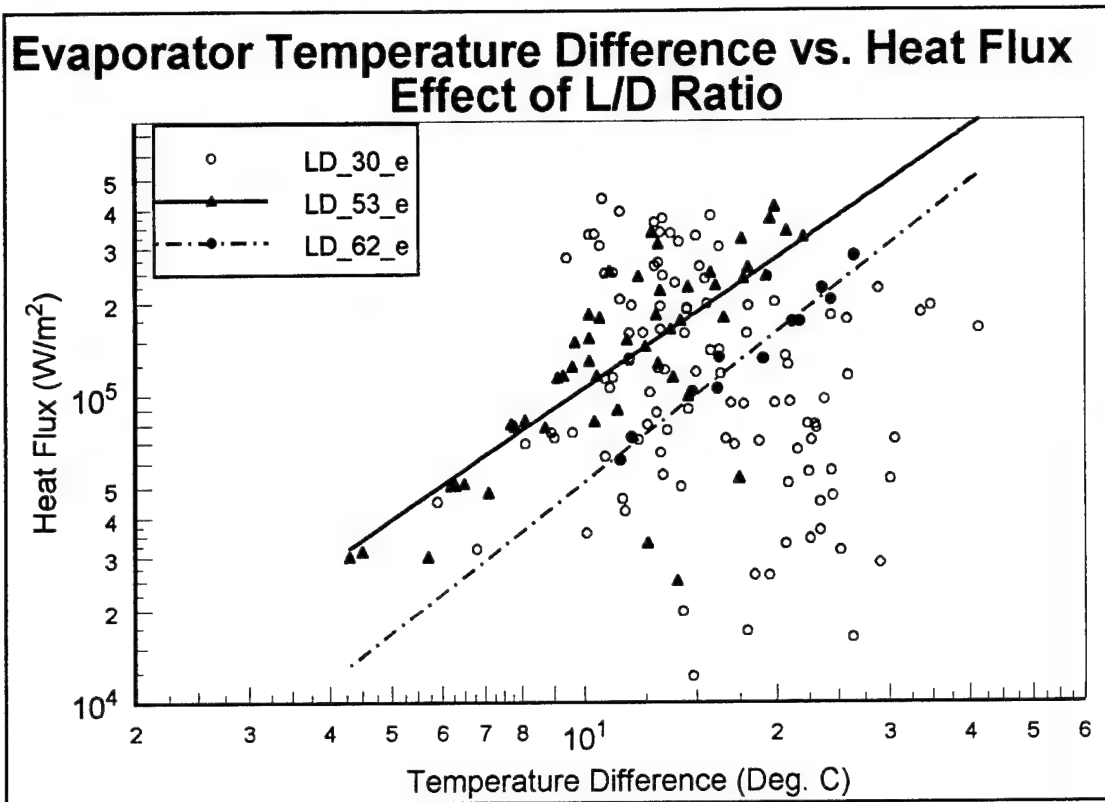


Figure 5-11

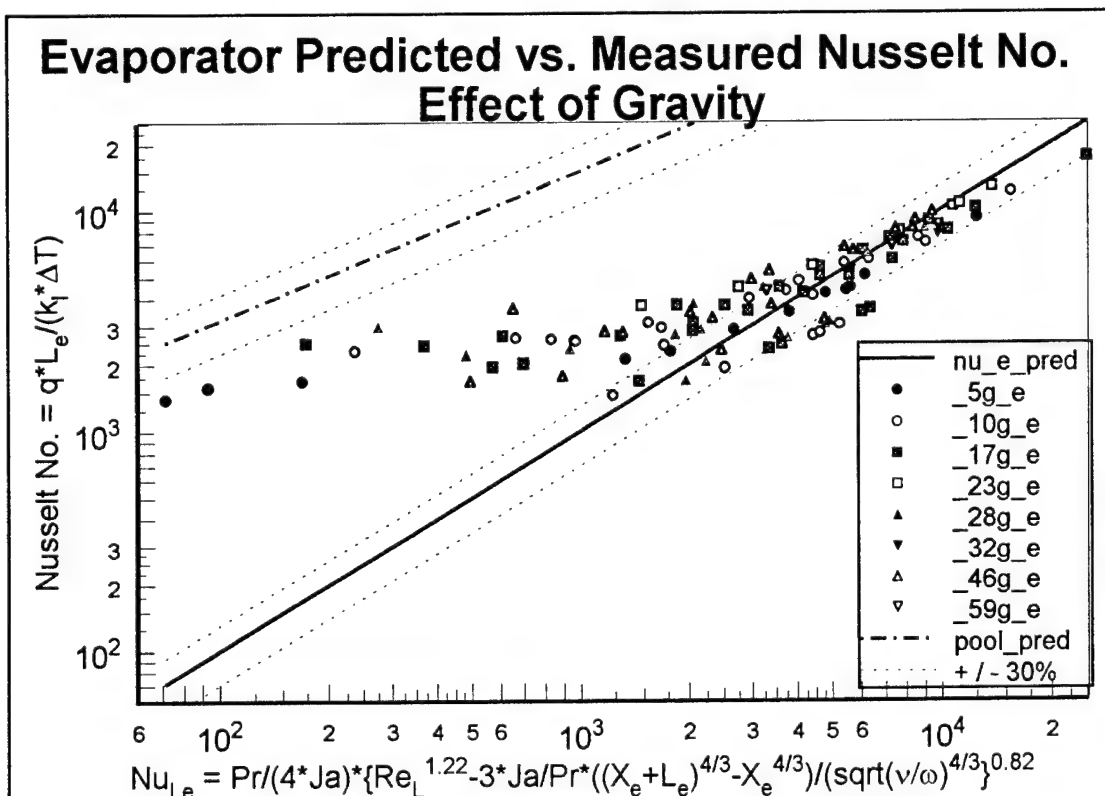


Figure 5-12

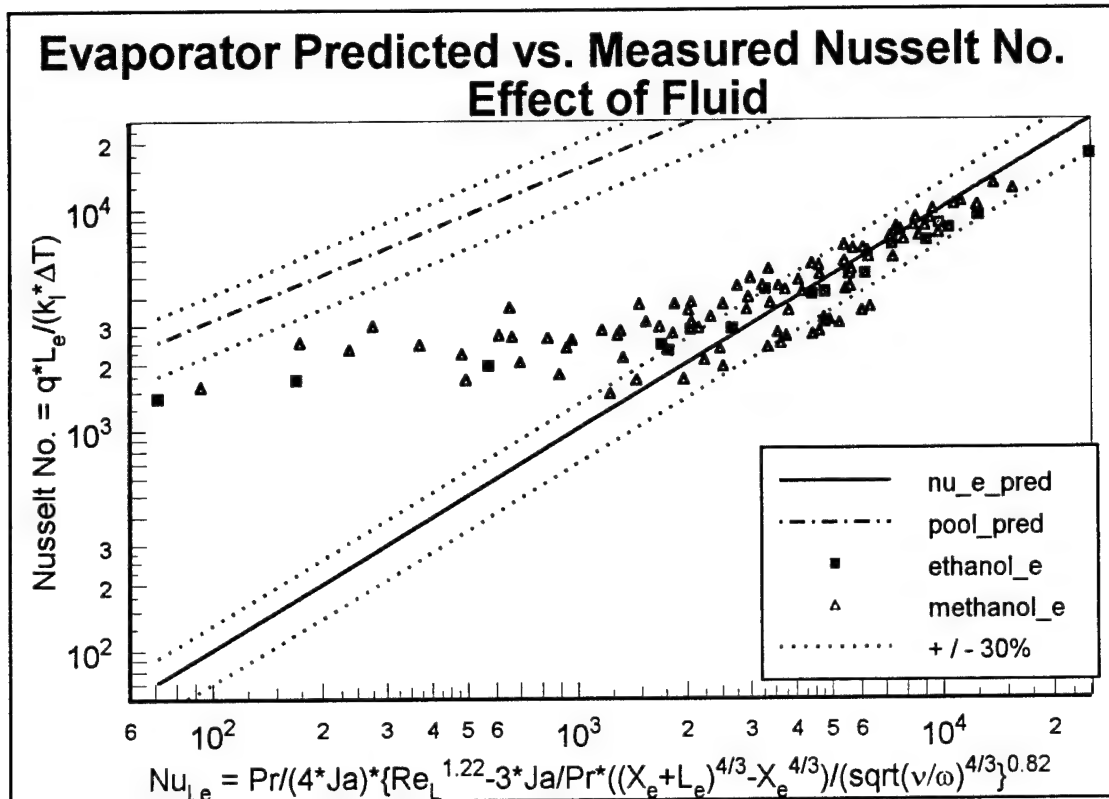


Figure 5-13

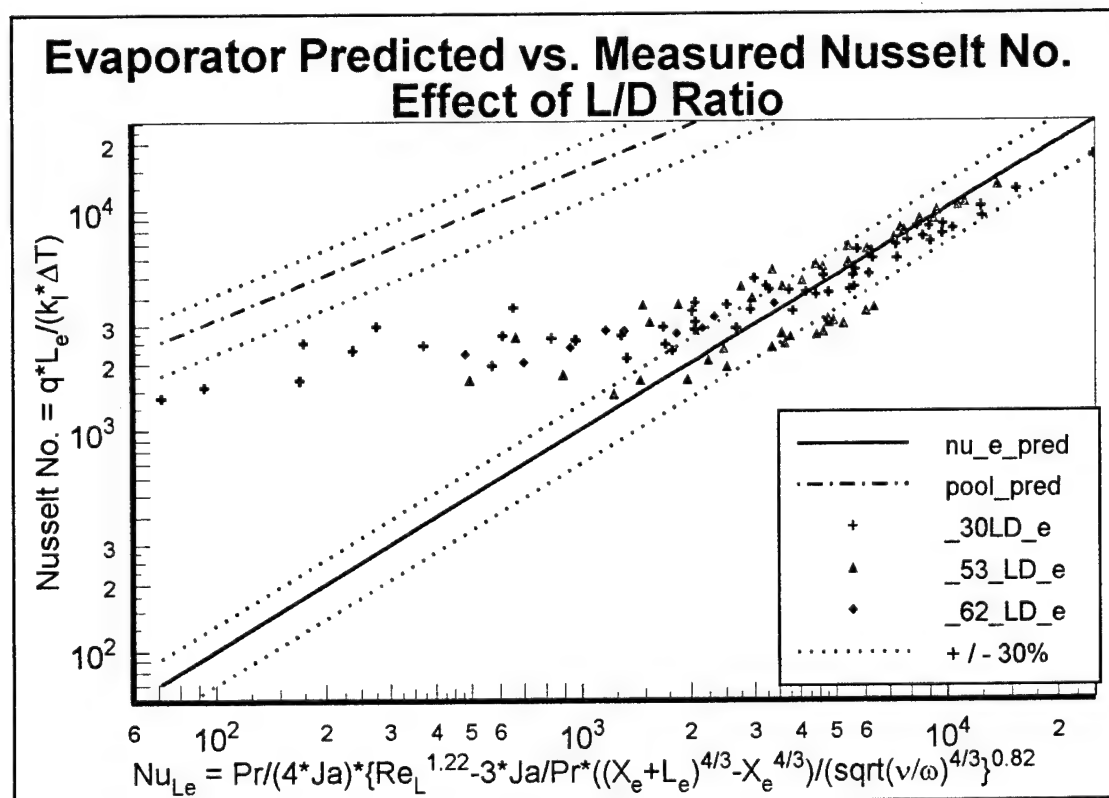


Figure 5-14

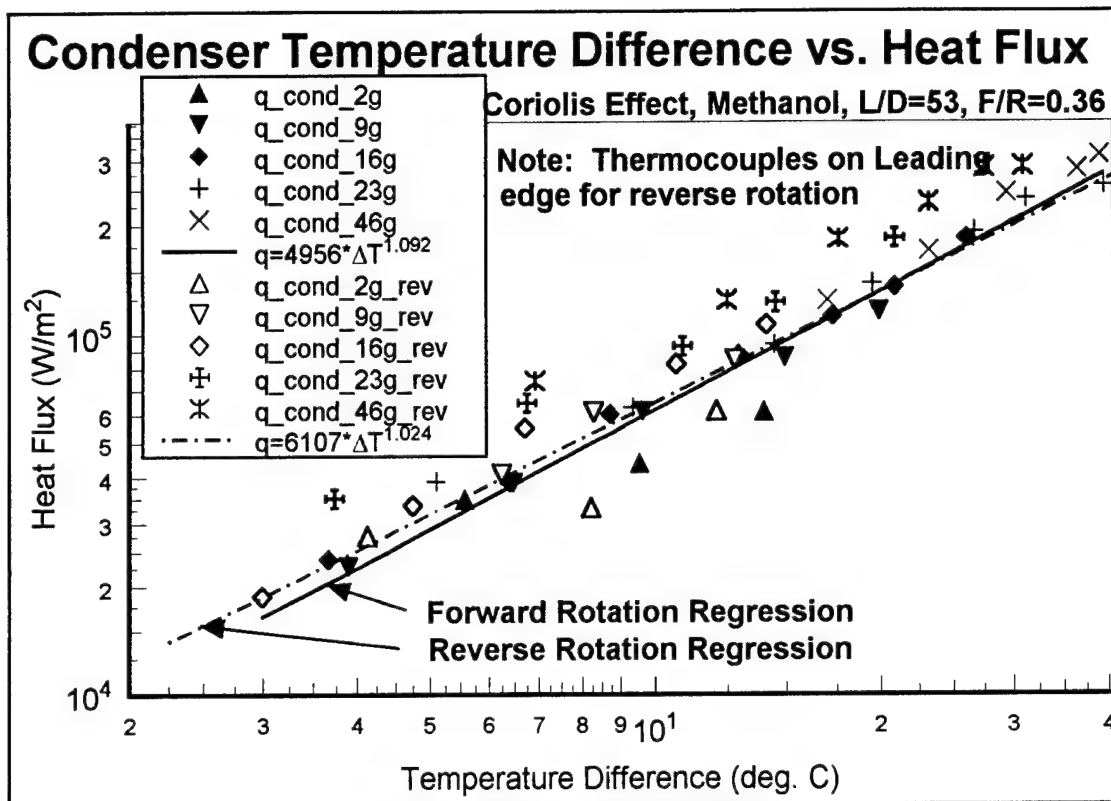


Figure 5-15: Coriolis Effect

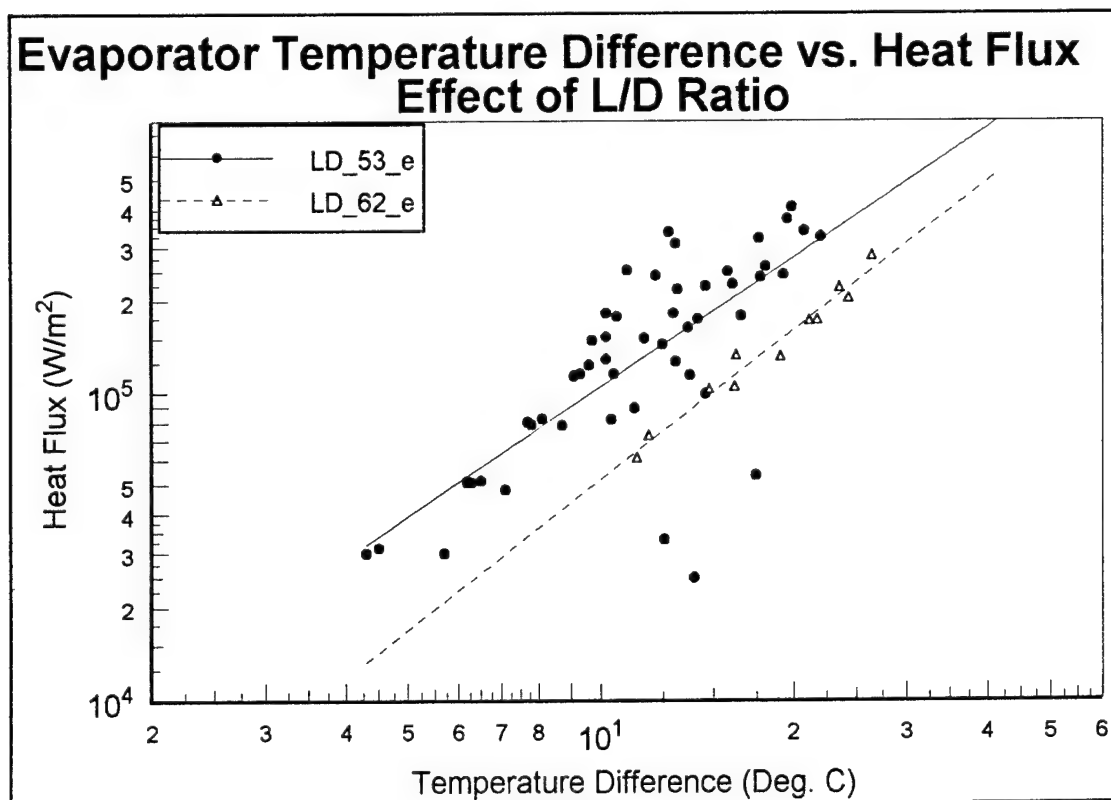


Figure 5-16

Appendix A: Thermosyphon Construction

This appendix describes the techniques and lessons learned in construction and operation of the test thermosyphons. The primary references used were Dunn & Reay [A-1] and Chisolm [A-2]. Both of these references contain fairly detailed descriptions of construction techniques, material selection and compatibility information and a list of commercial manufacturers of heat pipes. Dunn & Reay also contains a chapter on the practical aspects of heat pipe design which was very useful in designing the experiment. It is the intent of this appendix to augment rather than repeat information found in those references.

Selection of working fluids was based primarily on the expected operating temperatures of the thermosyphon and the fluid properties. Water, Methanol and Ethanol were chosen as test fluids. Water was later abandoned because of the difficulty in its use. There were two problems with water: 1) removal of dissolved gasses was extremely difficult and; 2) the low vapor pressure of water when at room temperature placed very rigorous requirements on the various seals of the thermosyphon to prevent air from leaking into it.

The container material was initially selected based upon compatibility with the working fluid. Dunn & Reay recommended copper for use with these working fluids. Because of its very high thermal conductivity, copper caused problems obtaining accurate temperature measurements. It is believed that this was caused by axial conduction of heat in the container walls. The thermosyphons from which the data was gathered were

constructed from yellow brass and type 304 stainless steel. Dunn & Reay reported that some researchers had experienced problems with stainless steel and the alcohols, however this author experienced no problems with stainless steel. Brass was a good compromise material since its thermal conductivity is one fourth that of copper but it is much easier to solder than stainless steel.

For this test program, the ability to empty and re-fill the thermosyphons was desired. Consequently, the filling valve was left on the thermosyphons during testing to seal out the atmosphere. This worked quite well. Brass plug valves with Viton O-rings were used quite successfully. New valves were disassembled and cleaned with acetone. The seals were then coated with silicone vacuum grease prior to re-assembly.

Both of the references cited above recommend welding or soldering for sealing heat pipes. All mechanical joints were sealed by soldering with Stay-Brite silver bearing solder. This solder's melting point is lower than normal silver solders, but is higher than lead-tin soft solder. It also has much greater strength characteristics than soft solder at the operating temperatures encountered in this research.

The fill valve, pressure transducer and the internal thermocouple probes were attached to the thermosyphon via mechanical connections to allow for removal and cleaning between uses. Swagelock brand connectors initially were used for these mechanical connections. Unfortunately, after assembling and disassembling these connectors 2-3 times they became susceptible to leaks. The thermosyphon design was then altered to accommodate Cajon VCO vacuum fittings. These fittings worked extremely well. In addition to being leak free and more sturdy, they allowed larger access

holes into the thermosyphon for brush cleaning the interior. Figure 4-1 depicts this version of the test thermosyphon.

The cleaning and filling procedure was adapted from several described [A-1] and [A-2]. The need for cleanliness when assembling thermosyphons cannot be overemphasized. Removal of all oils, greases and oxides from the container is essential to maintaining a vacuum inside the thermosyphon after disconnecting it from the vacuum system. The cleaning procedure used in this research was as follows:

1. Soak all components in a base bath overnight. Base bath formula is one cup of Potassium-hydroxide chips, one cup of distilled water and two gallons of methanol.
2. Passivate components by soaking for 15 minutes in a 15% nitric, 5% hydrochloric acid bath.
3. Rinse in distilled water.
4. After assembly, rinse inside of thermosyphon with trichloroethane.
5. Soak for 2 hours in trichloroethane.
6. Rinse out with acetone. Clean out with brush soaked in acetone.
7. Soak for 2 hours in acetone.
8. Rinse with distilled water.

Steps 4-8 were repeated each time a thermosyphon was re-filled.

The filling procedure is also critical in maintaining a vacuum long enough to complete testing. The filling procedure was:

1. Maintain vacuum in filling rig at all times.
2. Evacuate a new thermosyphon for a minimum of two days.
3. Close thermosyphon fill valve and vacuum pump isolation valve.
4. Remove and weigh evacuated thermosyphon.
5. Re-install thermosyphon, open vacuum pump isolation valve.

6. When ultimate vacuum is achieved, open thermosyphon fill valve.
7. Evacuate thermosyphon until there is no difference in ultimate vacuum with the fill valve open or closed.
8. Isolate vacuum pump from system by closing valve.
9. Open isolation valve to liquid burette.
10. Meter desired amount of fluid into fill rig.
11. Heat walls of fill rig to evaporate liquid off walls.
12. Close burette isolation valve and thermosyphon fill valve.
13. Remove and re-weigh thermosyphon to determine exact amount of liquid fill.

The design of the fill rig was essentially identical to those described in [A-2].

Figure A-1 depicts the configuration of the fill rig. The problem encountered with the fill rig was the inability to install a precisely measured amount of liquid into the test thermosyphon. Some of the fluid coats the walls of the fill rig, thus the volume measurement from the burette is only approximate. The most accurate measurement of the liquid in the thermosyphon comes from the weight difference. However, this is done after the fact so the only way to remedy an incorrect fill is to empty the thermosyphon and start over.

Type E thermocouples were used throughout the experiment. Initially, silicon diaphragm pressure transducers were used as the manufacturer indicated they would be acceptable for use with distilled water and the alcohols. However, the distilled water caused the silicon to rupture in a very short time, creating vacuum leaks in the thermosyphons. Pressure transducers with all stainless steel wetted parts were substituted with satisfactory results. The specific model used (Omega Engineering PX-120), did have

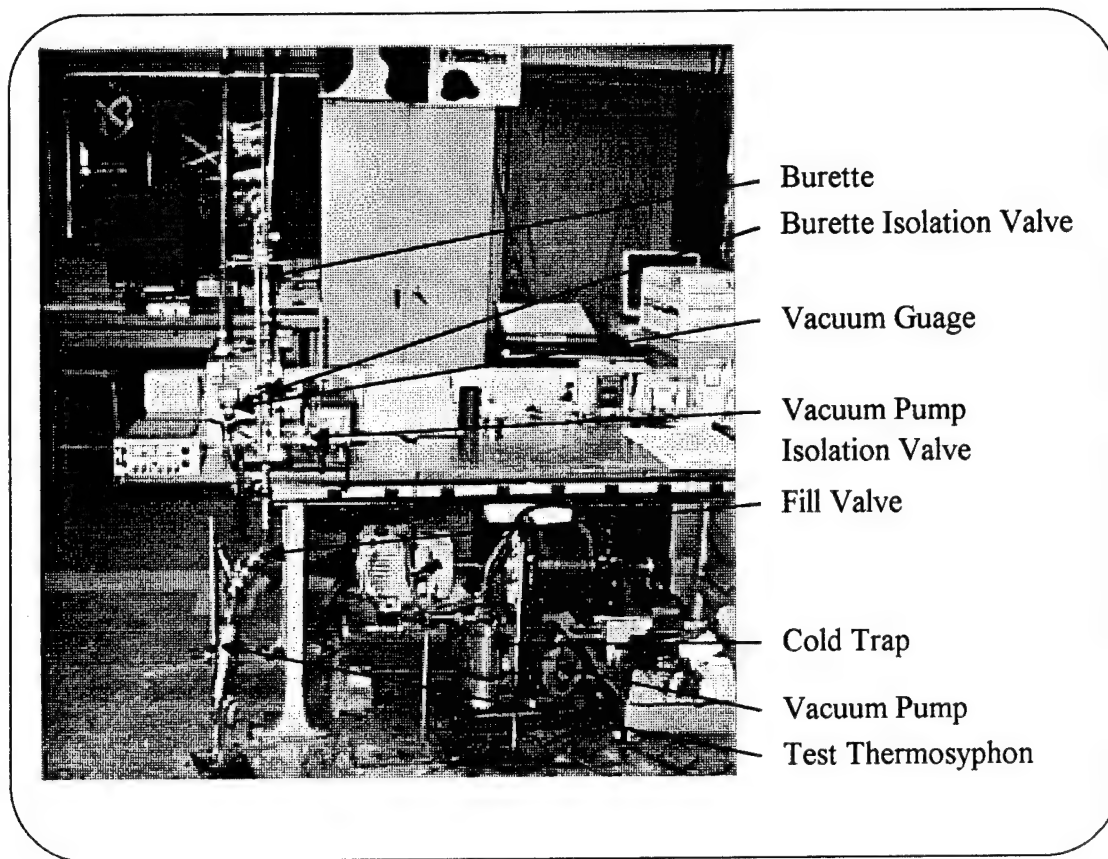


Figure A-1: Thermosyphon Fill Rig

a tendency to take a permanent set altering its zero reading significantly after exposure to a vacuum or vapor pressure for a few days. This created difficulty in correlating the pressure and temperature measurements until the thermosyphon was emptied and the zero on the transducer could be re-checked. Once the proper zero was entered into the data sheets, good correlation between the measured saturation pressure and measured saturation temperature was obtained.

A-1 Dunn, P.D. & Reay, D.A., *Heat Pipes, 4th ed.*, Pergamon, 1994.

A-2 Chisolm, D. et al., "Manufacture of Heat Pipes," *Analysis Design & Manufacture of Heat Pipes*, National Engineering Laboratory Course Papers, 19-21 June, 1973.

Appendix B: Data Summary

Methanol, L/D=53, F/R=0.40

pipe_no	gravity (g's)	q_cond (W/m ²)	t_sat (deg. C)	del_t_c (deg. C)	del_t_e (deg. C)
7	11	32,007	45	4	12
7	11	57,327	60	8	10
7	11	77,502	68	10	13
7	11	91,758	80	13	13
7	11	148,160	94	21	13
7	11	200,038	110	30	13
7	11	256,708	117	42	13
7	11	329,940	148	60	11
7	16	55,081	58	6	9
7	16	92,791	73	12	13
7	16	150,845	89	20	16
7	16	198,899	101	28	15
7	16	255,073	118	37	14
7	16	299,693	133	48	11
7	27	52,666	52	6	8
7	27	86,757	68	10	11
7	27	144,089	81	17	14
7	27	181,808	95	23	16
7	27	249,425	110	30	15
7	27	284,350	124	39	13
7	48	47,963	53	5	11
7	48	85,860	67	8	11
7	48	124,299	77	14	13
7	48	176,307	92	19	14
7	48	239,314	105	25	14
7	48	276,588	117	31	13

Methanol, L/D=53, F/R=0.44

pipe_no	gravity (g's)	q_cond (W/m ²)	t_sat (deg. C)	del_t_c (deg. C)	del_t_e (deg. C)
11	11	22,862	42	3	6
11	11	36,674	49	6	7
11	11	59,572	56	10	9
11	11	97,506	68	14	10
11	11	114,505	77	18	12
11	11	138,489	86	23	13
11	11	182,010	97	26	18
11	16	39,148	49	6	6
11	16	87,410	64	12	10
11	16	109,098	73	17	12
11	16	166,008	86	24	13
11	16	190,171	96	38	16
11	28	18,978	46	5	14
11	28	67,654	64	11	11
11	28	95,935	71	15	13
11	28	132,770	78	19	14
11	28	172,667	86	24	16
11	28	197,517	104	32	18
11	28	258,194	113	38	21
11	47	25,219	42	4	13
11	47	62,168	60	9	10
11	47	86,669	68	12	14
11	47	135,687	81	17	17
11	47	185,351	94	24	19
11	47	247,157	106	31	22

Methanol, L/D=53, F/R=0.36

pipe_no	gravity (g's)	q_cond (W/m^2)	t_sat (deg. C)	del_t_c (deg. C)	del_t_e (deg. C)
12	9	22,815	46	4	4
12	9	38,703	54	6	6
12	9	60,961	59	10	8
12	9	86,102	71	15	9
12	9	115,705	81	20	10
12	16	23,821	45	4	4
12	16	38,628	53	6	6
12	16	59,865	58	9	8
12	16	87,445	66	13	9
12	16	112,197	74	17	10
12	16	134,965	85	21	11
12	16	184,152	96	26	12
12	23	39,035	48	5	6
12	23	62,515	58	9	8
12	23	93,404	70	14	10
12	23	138,398	82	20	10
12	23	192,092	99	27	11
12	23	235,138	107	31	13
12	23	256,450	127	39	13
12	46	40,787	53	7	18
12	46	75,159	61	10	15
12	46	124,191	75	17	14
12	46	170,216	90	23	15
12	46	245	103	29	18
12	46	282,657	122	36	20
12	46	309,231	123	39	20

Methanol, L/D=30, F/R=0.33

pipe_no	gravity (g's)	q_cond (W/m ²)	t_sat (deg. C)	del_t_c (deg. C)	del_t_e (deg. C)
13	18	24,249	46	2	7
13	18	34,309	54	5	6
13	18	57,347	59	6	9
13	18	80,193	70	9	11
13	18	98,207	77	11	12
13	18	121,136	87	15	12
13	18	155,991	93	17	11
13	18	212,319	107	24	9
13	32	49,304	60	5	13
13	32	68,606	63	6	15
13	32	89,075	70	9	16
13	32	148,820	86	14	12
13	32	188,878	91	18	11
13	45	53,693	56	4	19
13	45	71,700	60	6	20
13	45	101,958	71	9	21
13	45	148,238	80	12	35
13	45	148,512	79	12	18

Methanol, L/D=30, F/R=0.25

pipe_no	gravity (g's)	q_cond (W/m^2)	t_sat (deg. C)	del_t_c (deg. C)	del_t_e (deg. C)
14	11	38,278	55	7	14
14	11	54,692	64	8	17
14	11	70,951	67	11	18
14	11	106,335	75	14	16
14	11	120,667	83	17	18
14	11	152,750	94	23	20
14	16	52,328	60	8	17
14	16	71,524	66	10	17
14	16	106,575	76	14	16
14	16	138,256	88	18	24
14	28	72,238	62	7	21
14	28	95,470	69	10	21
14	28	134,265	80	15	26
14	28	168,817	97	32	29
14	47	61,073	66	5	23
14	47	87,731	68	9	26
14	47	141,369	76	13	34

Ethanol, L/D=53, F/R=0.85

pipe_no	gravity (g's)	q_cond (W/m^2)	t_sat (deg. C)	del_t_c (deg. C)	del_t_e (deg. C)
15	8	7,787	44	7	28
15	30	7,377	50	12	19
15	53	9,172	47	11	18
15	75	1,470	38	5	10
15	75	9,231	53	16	28
15	75	23,798	54	7	30
15	75	49,059	58	8	32

Ethanol, L/D=30, F/R=0.20

pipe_no	gravity (g's)	q_cond (W/m ²)	t_sat (deg. C)	del_t_c (deg. C)	del_t_e (deg. C)
17	6	13,020	42	6	18
17	6	25,179	51	6	21
17	6	39,440	58	9	21
17	6	50,446	58	10	22
17	6	61,131	68	14	22
17	10	15,055	43	6	14
17	10	27,767	49	6	23
17	10	34,192	55	8	23
17	10	42,715	56	9	22
17	10	54,220	65	13	23
17	15	9,243	45	8	15
17	15	26,025	48	6	23
17	15	23,973	51	6	25
17	15	43,086	56	8	24
17	15	59,392	64	11	23
17	59	12,383	43	5	26
17	59	21,796	46	4	29
17	59	40,553	56	5	30
17	59	54,573	60	8	31

Ethanol, L/D=30, F/R=0.28

pipe_no	gravity (g's)	q_cond (W/m^2)	t_sat (deg. C)	del_t_c (deg. C)	del_t_e (deg. C)
18	6	27,232	55	6	10
18	6	35,076	60	9	12
18	6	60,917	70	14	13
18	6	54,351	78	18	12
18	6	99,908	90	24	12
18	6	120,787	99	31	12
18	6	189,956	120	47	11
18	6	232,413	143	66	11
18	10	19,860	52	7	20
18	10	41,784	59	10	13
18	10	66,726	72	15	13
18	10	120,744	91	27	14
18	10	186,091	118	43	13
18	10	251,560	142	61	10
18	15	19,929	53	8	18
18	15	58,328	64	10	14
18	15	90,256	80	18	15
18	15	145,827	99	30	14
18	15	205,163	117	42	13
18	15	252,768	134	54	10
18	59	35,790	59	6	24
18	59	73,715	70	10	24
18	59	125,028	84	18	41
18	59	184,305	96	25	19
18	59	230,313	113	34	16
18	59	290,267	124	42	16

Methanol, L/D=62, F/R=0.29

pipe_no	gravity (g's)	q_cond (W/m ²)	t_sat (deg. C)	del_t_c (deg. C)	del_t_e (deg. C)
19	16	77,098	63	13	20
19	16	93,262	75	17	21
19	28	55,160	54	8	12
19	28	79,707	65	12	16
19	28	99,893	72	16	19
19	28	131,986	81	20	22
19	28	154,973	91	25	24
19	47	46,676	58	8	11
19	47	77,857	61	10	15
19	47	100,594	70	14	16
19	47	131,421	74	16	21
19	47	168,541	84	22	24
19	47	214,438	92	27	26

Methanol, L/D=53, F/R=0.36 Reverse Rotation

pipe_no	gravity (g's)	q_cond (W/m^2)	t_sat (deg. C)	del_t_c (deg. C)	del_t_e (deg. C)
12a	2	27,545	48	5	4
12a	2	32,878	61	8	7
12a	2	61,189	70	12	12
12a	9	21,500	49	2	6
12a	9	40,658	51	6	6
12a	9	60,663	61	8	7
12a	9	84,704	74	13	9
12a	16	18,764	43	3	6
12a	16	33,461	47	5	7
12a	16	54,775	56	7	8
12a	16	82,520	68	11	8
12a	16	105,826	79	14	8
12a	23	35,006	46	4	9
12a	23	64,430	60	7	7
12a	23	92,241	70	11	9
12a	23	122,350	78	14	11
12a	23	183,890	99	21	13
12a	46	47,821	50	5	8
12a	46	74,047	59	7	10
12a	46	123,511	72	12	13
12a	46	182,529	90	18	13
12a	46	229,534	105	23	14
12a	46	285,908	119	28	16
12a	46	288,392	124	31	18